Universität Stuttgart

Ab initio Studies of Solid Phase Diagrams with Quantum Chemical Theories

Von der Fakultät Chemie der Universität Stuttgart
zur Erlangung der Würde eines Doktors der Naturwissenschaften
(Dr. rer. nat.) genehmigte Abhandlung

Vorgelegt von
Ke Liao
aus Leiyang, China

Hauptberichter: Prof. Ph.D. Ali Alavi
Mitberichter: Prof. Dr. Andreas Köhn
Mitprüfer: Prof. Dr. Rainer Niewa

Tag der mündlichen Prüfung: 14. Juli, 2021

Institut für Theoretische Chemie der Universität Stuttgart
2021

Supervisor:
Prof. Ph.D. Ali Alavi
Day-to-day Supervisor:
Prof. Dr. Andreas Grüneis

"*The first principle is that you must not fool yourself and you are the easiest person to fool.*"

—Richard P. Feynman

UNIVERSITÄT STUTTGART

Zusammenfassung

***Ab initio* Studies of Solid Phase Diagrams with Quantum Chemical Theories**

In dieser Arbeit wenden wir zunächst mehrere etablierte Methoden an, darunter Full Configuration Interaction Monte Carlo (FCIQMC) und Coupled Cluster Singles und Doubles (CCSD). Wir berechnen damit die festen Wasserstoffphasen unter hohem Druck und stellen fest, dass CCSD ein statisches Phasendiagramm voraussagt, das gut mit der state-of-the-art Diffusion Monte Carlo (DMC) Methode übereinstimmt, insbesondere auf den stabilsten Phasen. Wir merken an, dass alle existierenden Arbeiten an festen Wasserstoffphasen, Geometrien verwenden, die durch Dichtefunktionaltheorie (DFT) unter Verwendung unterschiedlicher Austauschkorrelations-Funktionale optimiert wurden. Als zweiten Schritt und um über DFT hinauszugehen, entwickeln und implementieren wir daher für die Geometrieoptimierungen der festen Wasserstoffphasen, ein Programm, das die MP2-Kräfte unter Verwendung eines ebenen Wellenbasissatzes berechnet. Die durch DFT-PBE erhaltenen C2/c-24 Modellstrukturen werden mit den MP2-Kräften weiter entspannt und die resultierenden Strukturen liefern Bandlücken, berechnet nach der G_0W_0-Methode und unter störungstheoretischer Berücksichtigung der Elektron-Phonon-Wechselwirkungen, die gut mit Experimenten übereinstimmen. Darüberhinaus sind die H_2-Vibron-Frequenzkurven in Abhängigkeit vom Druck, berechnet auf Basis der MP2 optimierten Strukturen, in fast perfekter Übereinstimmung mit einem der Experimente und liefern wertvolle theoretische Einblicke hinsichtlich langjähriger Diskrepanzen zwischen Experimenten über die Druckkalibrierungskurve bei hohen Drücken. Schließlich, um bestehende Methoden effizienter und genauer zu machen kombinieren wir die Transkorrelierte Methode (TC) mit der Coupled Cluster Methode, mit einer Anwendung auf das dreidimensionale, gleichförmige Elektronengas (3D UEG), das ein Modellsystem für periodische Festkörper ist. Traditionell wurde die TC-Methode verwendet, um die Koaleszenzbedingungen der Wellenfunktion direkt in den TC-Hamiltonian einzuführen, sodass weniger Basisfunktionen benötigt werden, um Energien zu erreichen, die frei von Fehlern aufgrund der Unvollständigkeit des Basissatzes sind. Wir stellen fest, dass das TC-Framework sehr allgemein ist und zusätzliche Korrelationseffekte neben den kurzreichweitigen Koaleszenzbedingungen auch eingeführt werden können und möglicherweise

sogar die Genauigkeit von Näherungsmethoden wie Coupled/Distinguishable Cluster Doubles (CCD/DCD) in Systemen mit starken Korrelationen verbessert wird. Inspiriert durch die Paarkorrelationsfunktionen im reelen Raum für das 3D-UEG, entwerfen wir einen Korrelator, der ihr Verhalten als Funktion der Elektronendichte nachahmt. Zusätzlich wurde ein einfaches Framework eingeführt, das darauf basiert das HF-Gewicht in der Wellenfunktion zu maximieren, um die Parameter im Korrelator zu optimieren. Dadurch werden die Genauigkeit und Effizienz von TC-CCD und TC-DCD über einen großen Bereich von Elektronendichten deutlich verbessert im Vergleich zu ihren kanonischen Gegenstücken, wobei FCIQMC- und DMC-Ergebnisse als Benchmark-Daten verwendet werden. Wir hoffen diese Methoden in Zukunft auf echte, periodische, feste Materialien zu verallgemeinern.

UNIVERSITÄT STUTTGART

Abstract

Ab initio Studies of Solid Phase Diagrams with Quantum Chemical Theories

In this thesis, we first apply several existing methods, including full configuration interaction Monte Carlo (FCIQMC) and coupled cluster singles and doubles (CCSD), on the solid hydrogen phases under high pressures and find that CCSD predicts a static phase diagram that agrees well with the state-of-the-art diffusion Monte Carlo (DMC), especially on the most stable phases. Noticing that all existing studies on the solid hydrogen phases use structures which are optimized by density functional theory (DFT) using different exchange-correlation functionals, as a second step and to go beyond DFT, we develop and implement a program that calculates the MP2 forces using a plane wave basis set for the structural optimization of the solid hydrogen phases. The C2/c-24 model structures obtained via DFT-PBE are further relaxed using the MP2 forces and the resulting structures provide band gaps, calculated by the G_0W_0 method and with the electron-phonon interactions included perturbatively, that agree reasonably well with experiments. Furthermore, the H_2 vibron frequencies versus pressure curve calculated based on the MP2 optimized structures agree almost perfectly with one of the experiments, providing valuable theoretical insights in dissolving a long-standing dispute among experiments over the pressure calibration curve at high pressures. Finally, to make existing methods more efficient and accurate, we combine the transcorrelation method (TC) and the coupled cluster methods, with an application on the three dimensional uniform electron gas (3D UEG) which is a model system for periodic solids. Traditionally, the TC method has been used to incorporate the short range cusp conditions in the wavefunction directly into the TC Hamiltonian, so that fewer basis functions are needed to achieve energies that are free from the basis-set incompleteness errors. We notice that the TC framework is very general and correlations in addition to the short range cusp conditions can also be included and potentially improve even the accuracy of approximate methods like coupled/distinguishable cluster doubles (CCD/DCD) in systems with strong correlations. Inspired by the pair-correlation functions in real space for the 3D UEG, we design a correlator that mimics their behaviours as a function of the electron density. In

addition to that, a simple framework which aims to maximize the HF weight in the wavefunction is introduced to optimize the parameters in the correlator. As a result, the accuracy and efficiency of TC-CCD and TC-DCD are improved significantly compared to their canonical counterparts over a large range of electron densities, using FCIQMC and DMC results as benchmark data. We hope to generalize these methods to real periodic solid materials in the future.

Acknowledgements

I am deeply grateful for those people I met during this scientific journey in life, who have inspired me and ignited the curiosity inside of me by being so curious and genuine towards life themselves. They are the elder kids in my village who shared in such excitement and joy the new word "gravity" they had learned in school; they are the young mathematics teacher in middle school who talked about the exotic world of special relativity as if he had experienced the time dilation and space contraction himself; they are the physics teacher in middle school who I followed on the way to the canteen after classes and answered my endless questions about how a fluorescent lamp works; they are the biology teacher in high school who saw me as a kid with fire of passion and curiosity; they are the head teacher (Prof. Jing Shi) during my undergraduate study who encouraged us to always allow ourselves to spend some time in life pondering on things randomly and not following the beaten path; they are also the great minds like Richard Feynman whose life and scientific stories I had read from books.

For the completion of this thesis, I want to express my sincere gratitude to my supervisor Prof. Dr. Ali Alavi who once said "one never stops trying new ideas", and indeed that is what he has been tirelessly and joyfully practicing. The best teaching is through examples and I think he does a great job. Ali is always up for spontaneous discussions, during which new ideas are frequently exchanged. He is always open and patient in listening to his students' ideas. This light and inclusive attitude that he leads fuels the good relationships and creativity among all group members. I also want to thank my day-to-day supervisor Prof. Dr. Andreas Grüneis, without whose support and guidance, I would have lost in a lot of the technical details. What I appreciate the most is the resolve and determination that he shows when facing problems. His endless focus and energies when solving problems set a good example for me to complete this thesis.

我将永远亏欠于我的父母。尽管当时家里经济比较拮据，他们在我儿时花费了很多心血和时间陪伴我，让我能得到好的教育。另一方面，他们没有像很多其他传统的中国式父母一样对我很严格，而是让我有很多自由和选择。我十分珍惜他们这一路的爱和支持。 (I am forever in debt to my parents who have spent so much time with me during my childhood to ensure that I had enough company and could get a proper education, despite the financial stress. On the other hand, they did not go to the extreme as a lot of other traditional Chinese parents would have done, that is being too strict and turning into tiger parents. I value a lot their love and support along the way.)

I would also like to express my gratitude towards all my colleagues in Stuttgart and in Vienna for being so nice and helpful. I have learned a lot from them and had a great time in both places. Recreational wise, they are always up for a hiking or biking trip when there was no pandemic. The beautiful hiking trip in Austria organised by Oskar Weser and the biking trip around the Bodensee with Dr. Vamshi Katukuri, Niklas Liebermann and Dr. Khaldoon Ghanem are particularly memorable, amongst a few others. In particular, I want to thank Dr. Kai Guther for planning the fantastic trans-Siberia train trip. His humor and patience make very good companion for long trips. In addition, he teaches patiently German lessons and many other things free of charge. I am looking forward to some other crazy trips that we can take in the future. I would also like to thank Dr. Nikolay Bogdanov for suggesting good places to visit during the trip. German is a hard language to learn, but I have had help from my German-speaking and German-learning colleagues, Niklas, Kai, Werner, Vamshi and Eugenio, just to name a few. We have started the "Deutschermittagstisch" initiative where we speak only German during lunch, which eventually did not last mostly due to the unusual silence observed during lunch and the ongoing pandemic [1].

Academically speaking, I have participated in many stimulating discussions and received countless helpful advice from my colleagues. In Stuttgart, especially, I want to thank Dr. Daniel Kats, who helped me a lot with the coupled cluster theory. I can just knock on his office door and ask for a discussion almost anytime. Or, whenever I had questions during the pandemic and sent them via messages, he would also answer them swiftly. The discussions with him are always delightful and can get things sorted out at the same time. I thank Dr. Werner Dobrautz and Kai for help with the NECI code; Dr. Pablo Lopez Rios for explaining things related to DMC; Dr. Giovanni Li Manni for the knowledge of strongly correlated systems, mostly learned from the coffee corner talks; Kai, Khaldoon and Dr. Lauretta Schwarz for contributing to the neural network project that we attempted; Dr. Hongjun Luo for the help with UEG and TC in NECI; Dr. Aron Cohen for the discussions on whether solid hydrogen can be metallic or not, on which we still have a bet. In Vienna, I would like to thank Dr. Andreas Irmler for the stimulating discussion on basis set correction, which almost made me miss the flight back to Stuttgart. I also thank Alejandro Gallo for organising the online seminars during the pandemic that cover state-of-the-art topics. The help from Dr. Felix Hummel with the usage of VASP and development on CC4S is gratefully acknowledged. Many thanks

[1] Hence I am writing this thesis in English.

to Dr. Xin-Zheng Li and Tong Shen from Peking University for the discussions on electron-phonon interactions.

For the proofreading of this thesis, I appreciate help from Daniel, Werner, Vamshi, Giovanni, Kai, Niklas, Pablo, Thomas Schraivogel and Tong Shen. Especially, I thank Thomas for correcting the German abstract.

Contents

谨以此文献给我儿时的欢乐港湾，我亲爱的爷爷。

Dedicated to the happy harbor of my childhood, my dear grandfather.

Part I

Introduction

"All things are made of atoms." is the shortest sentence that Richard Feynman believed to be able to convey the most important scientific knowledge to a post-apocalyptic world for the next generation of intelligent creatures to restart science. The behaviors of atoms are governed by the laws of quantum mechanics, so are those of their constituent parts such as electrons and nuclei. To be more specific, the Schrödinger equation dictates the details of the behaviors of all those microscopic particles when the relativistic effects can be ignored. Methods which are based on the Schrödinger equation and do not require additional inputs other than some fundamental constants to predict the properties of quantum systems, like molecules or solids, are called *ab initio* or first principles.

In classical mechanics, the first principles theory is the Newton laws, based on which the movement of a macroscopic object can be predicted precisely, once some crucial parameters are known, such as the forces, mass, initial velocity, etc. Ideally, the same level of success is desirable using quantum mechanics in the microscopic world as the Newtonian mechanics did in the macroscopic world—once the molecular structure of a material is known, we should be able to accurately predict the properties of the system according to the Schrödinger equation. For example, we want to predict if a certain arrangement of atoms will be more stable than another. This could provide us with the so-called phase diagrams, such as the energy versus pressure diagram of different phases, of a solid material without even synthesizing it in the laboratory. It could open the door to fast design and discovery of materials with novel properties, which can greatly enrich our toolbox in pushing the boundaries in science and technology and can have significant impacts on the human society as well. Thanks to the increasingly efficient modern computers, we are able to make some of these predictions on certain materials where the correlations among electrons are not so strong, that is the state of each electron does not depend strongly on the states of the other electrons in the system. But the goal of making general and accurate predictions on any systems is still out of our reach. Using state-of-the-art quantum Monte Carlo to obtain the exact solution to a quantum many-body problem is exponentially hard with respect to the number of the simulated particles [1], and approximate methods that have satisfactory accuracy also come with high polynomial scaling in computational cost.

Practically, various approximations have been introduced to make solving the Schrödinger equation more tractable. One of the most important ones is the Born-Oppenheimer (BO) approximation, which decouples the movements of the light electrons and the heavy nuclei. The general idea is that the former are so light that they can adapt to the "slow" movements of the latter almost

instantaneously, so that we can solve the electronic problem with static nuclei and the nuclei problem with the electron clouds as external potentials in two subsequent steps.

Even with the BO approximation, solving the many-electron Schrödinger equation is still an exponentially hard problem. So some further approximations are needed. For example, in density functional theory (DFT), which scales only $\mathcal{O}(N^3)$ with system size N, i.e. the number of electrons in the system, the electrons are treated as non-interacting quasiparticles and the correlation effects are all included in the so-called exchange-correlation (XC) functional; Hartree-Fock (HF) theory ($\propto \mathcal{O}(N^4)$) [2] includes the correct exchange symmetry in the wavefunction by using a single Slater determinant as an ansatz for the true many-electron ground state wavefunction, while the electronic correlations are treated only in a mean-field fashion. The latter and the later developed correlation methods that are based on it are often called wavefunction-based or quantum chemical methods.

One of the important post-HF theories is the coupled cluster (CC) theory, which employs an exponential excitation operator on a reference determinant, often the HF determinant, to approximate the true many-electron ground state wavefunction. The coupled cluster singles and doubles (CCSD) ($\propto \mathcal{O}(N^6)$) ansatz is one of the most practical methods that has a good compromise between accuracy and efficiency; coupled cluster singles and doubles plus perturbative triples (CCSD(T)) ($\propto \mathcal{O}(N^7)$) is the *de facto* standard in quantum chemistry for predicting properties of small systems that match the best with experiments in most of the cases. Another important category is the quantum Monte Carlo (QMC) methods, which generally represent the many-electron wavefunction using random walkers in continuous real or discrete Slater determinant space. In diffusion Monte Carlo (DMC), a projector consisting of the diffusion and branching steps is repeatedly applied to stochastically project out higher energy components of an initial guess of the wavefunction, so that only the ground state wavefunction remains in the limit of infinite projection time. However, DMC relies on a trial wavefunction, thus some bias, to avoid the collapse onto the undesired bosonic ground state. Despite this approximation, DMC has been successfully applied to molecules and solids, and is one of the most accurate and efficient *ab initio* methods. Using the product of a Slater-Jastrow (SJ) factor and a single Slater determinant as the trial wavefunction, DMC can achieve $\mathcal{O}(N^4)$ scaling with the system size. However, in strongly correlated systems where more Slater determinants are needed in the trial wavefunction in order

[2] The transformation of orbitals scales $\propto \mathcal{O}(M^5)$, where M is the number of orbitals

to target a certain accuracy, the scaling of DMC will also increase. Full configuration interaction quantum Monte Carlo (FCIQMC) uses a similar idea, but in Slater determinant space, where the antisymmetry of the wavefunction upon the exchange of two like-spin electrons is enforced. This gives FCIQMC an advantage that the exact ground state wavefunction can emerge automatically once enough random walkers are used. Formally, FCIQMC scales exponentially with the system size.

In this thesis, both the electronic and the nuclear problems are treated within the framework of the BO approximation. A large part of this thesis is dedicated to the electronic problem, with one example showing that CCSD can predict accurate static phase diagrams of solid hydrogen phases under high pressures. Structural optimisation is also attempted in this thesis, in order to better understand the solid hydrogen phases. To this end, the algorithm to compute the nuclear forces on the level of the second order Møller-Plesset perturbation (MP2) using the plane wave basis is implemented. Using the MP2 forces, the crystal structures of solid hydrogen models at high pressures are optimised. The optimised structures show very good agreement with experiments in the H_2 vibron frequencies as a function of the pressure. After the nuclear problem is solved perturbatively to include the effects due to the electron-phonon interaction (EPI), the band gaps of the optimised structures are also in reasonable agreement with experiments. New theoretical methods are also developed to solve the electronic problem more accurately and efficiently. In particular, the idea of including physical insights in terms of a similarity transformation (ST) on the many-electron Hamiltonian, which can compactify the ground state wavefunction in Slater determinant space, is combined with the coupled cluster doubles (CCD)/distinguishable cluster doubles (DCD) theory. The ST method is also termed transcorrelation (TC), which dates back to Boys and Handy [2, 3] in the late 1960s. The combination scheme, termed as TC-CC, is applied to the three dimensional uniform electron gas (3D UEG) model to showcase its greatly improved efficiency and accuracy, compared to traditional CC methods.

The thesis is structured as follows. In part II, we introduce some of the basic notions, tools and theories that are relevant to this thesis. These include some fundamental concepts in quantum mechanics, such as the indistinguishability, spins and exchange symmetries of quantum particles; the essential Bloch's theorem for periodic systems and a simple model for periodic solids, 3D UEG; elaboration on the BO approximation; second quantization and the Wick's theorem; mean-field theories, including the HF theory and DFT; diagrammatic theories like MP2 and CC; further details on on DMC and FCIQMC. Since the

main topic of the thesis is on phase diagrams of periodic solids, techniques to correct finite size errors are also covered. Towards the end of this part, the perturbative treatment of the EPI will be briefly reviewed. In part III, the focus will be on the new theoretical developments made during my Ph.D. study, including the MP2 nuclear forces and TC-CCD. In part IV, applications of the existing theories and newly developed tools on solid hydrogen phases and 3D UEG will be presented. In part V, the thesis is concluded with a summary of the main contents and some outlook for future directions.

Part II

Theory

Chapter 1

Introduction to the Quantum Many-body Problem

The discovery of quantum mechanics in the early 1900s unveiled the curtain for, as of now, over a century's developments and applications of the theory. It is now established as one of the most accurate theories in human history. The word "quantum" refers to small quantities that are discrete and cannot be divided into smaller parts. It reflects our realisation that our world is fundamentally discretised. The concept of quantized energy was first introduced by the German physicist Max Planck between 1900 and 1901 to resolve the troubling problem of the ultraviolet catastrophe in black body radiation [4], and later was further developed by Albert Einstein [5] and others. The behaviors of microscopic particles are distinctly different from those of macroscopic objects, in that they possess both properties of waves and particles. This duality puts some fundamental limits to how precisely two conjugate variables, such as the position and momentum of a microscopic particle, like the electron, can be measured at the same time. This is the so-called *Heisenberg's uncertainty principle*. This duality has also led to the discovery of Schrödinger's wave equation for non-relativistic quantum particles, which is now known as the time-dependent Schrödinger equation,

$$\mathrm{i}\frac{\mathrm{d}}{\mathrm{d}t}\Psi(\mathbf{X},t) = \hat{H}\Psi(\mathbf{X},t), \tag{1.1}$$

where i is the imaginary unit and atomic units are used [1], $\Psi(\mathbf{X},t)$ is the wavefunction describing the evolution of a state of the system as a function of time and $\hat{H}$ is the Hamiltonian of the system. The underlying assumption is that since particles behave also like waves, there must be a "wave" equation similar to the classical one to describe this behavior. So instead of describing definite trajectories of particles in time, $\|\Psi(\mathbf{X},t)\|^2$ is used to represent the probability

[1] We set the reduced Planck constant $\hbar = 1$, the speed of light $c = 1$, elementary charge $e = 1$ and electron mass $m_e = 1$.

density of finding the particles (either electrons or nuclei) in the position configuration $\mathbf{X} = \{\mathbf{x}_1, \mathbf{x}_2, \ldots, \mathbf{x}_i, \ldots, \mathbf{x}_N\}$ at a specific time t, where $\mathbf{x}_i$ denotes the position of particle i.

Within the scope of this thesis, the stationary states are of interest, to be more specific, only the ground state and a few low-lying excited energy states. To this end, the stationary or time-independent Schrödinger equation is often used [2]

$$\hat{H}\Psi(\mathbf{X}) = E\Psi(\mathbf{X}), \tag{1.2}$$

which mathematically is an eigenvalue problem.

In this thesis, the quantum many-body problem is limited to periodic solids (crystals), where normally the periodic boundary condition is applied. From now on, for simplicity, the term "solids" refers to periodic solids or crystals. Solids consist of nuclei and electrons, which are positively and negatively charged, respectively. The Hamiltonian for such a system is written as

$$\hat{H} = -\sum_{n=1}^{N}\frac{1}{2}\nabla_n^2 - \sum_{\mu=1}^{K}\frac{1}{2M_\mu}\nabla_\mu^2 - \sum_{i=1}^{N}\sum_{\mu=1}^{K}\frac{Z_\mu}{|\mathbf{r}_i - \mathbf{R}_\mu|} + \sum_{j>i}^{N}\frac{1}{|\mathbf{r}_i - \mathbf{r}_j|} + \sum_{\mu>\nu}^{K}\frac{Z_\mu Z_\nu}{|\mathbf{R}_\mu - \mathbf{R}_\nu|}, \tag{1.3}$$

The first term on the right hand side (r.h.s.) of equation (1.3) refers to the sum of the kinetic energy operators of the N electrons in the system; the second term is a sum of the kinetic energy operator of the K nuclei, where M_μ stands for the mass of nucleus μ; the other three terms are the sums of nucleus-electron, electron-electron, and nucleus-electron optential operators, respectively, where Z_μ refers to the charges that nucleus μ carries.

1.1 Identical Particles, Spins and Exchange Symmetries

In the quantum world, one has to abandon the classical sense of trajectories due to the uncertainty principle. The wavefunction reflects the nature of this uncertainty by representing the particles' states as probability clouds. This then leads to the important concept of *identical* particles in quantum mechanics: particles belonging to the same species have exactly the same intrinsic properties such as mass, electric charge and spin, e.g. electrons. Two identical quantum particles are indistinguishable from each other. To reflect this indistinguishability in the total wavefunction of two identical particles, it is required that if $\Psi(\mathbf{x}_1, \mathbf{x}_2)$ is a

[2] In the QMC methods, the imaginary-time Schrödinger equation will used to derive the algorithms to get the ground state wavefunction.

solution to the static Schrödinger equation, i.e. $\hat{H}\Psi(\mathbf{x}_1, \mathbf{x}_2) = E\Psi(\mathbf{x}_1, \mathbf{x}_2)$, so should $\Psi(\mathbf{x}_2, \mathbf{x}_1)$ be a valid solution. This is only possible when $\Psi(\mathbf{x}_1, \mathbf{x}_2)$ and $\Psi(\mathbf{x}_2, \mathbf{x}_1)$ are related by a constant C,

$$\begin{aligned} \Psi(\mathbf{x}_1, \mathbf{x}_2) &= C\Psi(\mathbf{x}_2, \mathbf{x}_1) \\ \Psi(\mathbf{x}_2, \mathbf{x}_1) &= C\Psi(\mathbf{x}_1, \mathbf{x}_2), \end{aligned} \tag{1.4}$$

from which we conclude that $C^2 = 1$ or $C = \pm 1$ [3]. The case when $C = -1$ indicates that the total wavefunction is antisymmetric upon exchanging two identical particles, which we call fermions and have half integer spins; the other case refers to a symmetric total wavefunction of two identical particles, which we call bosons and have integer spins. It is worth pointing out that the antisymmetry in the fermionic wavefunction naturally ensures the Pauli exclusion principle, which states that two identical particles (now including the same spin attribute) cannot occupy the same state. In real space, it is equivalent to requiring that $\Psi(\mathbf{x}_1, \mathbf{x}_2) = 0$, when $\mathbf{x}_1 = \mathbf{x}_2$, which is the case when the total wavefunction is antisymmetric.

1.2 Born-Oppenheimer Approximation

The large ratio (10^3) between the masses of a typical nucleus and an electron is the basis for the BO approximation. The main idea is that electrons move much faster than the much heavier nuclei when they are in thermal equilibrium and thus the decoupling of their motions is justified. Mathematically, the full many-body problem of Eq. (1.2) is split into the electronic and nuclear parts by approximating the full many-body wavefunction using a product of the electronic and the nuclear wavefunction as follows

$$\Psi(\{\mathbf{r}\}, \{\mathbf{R}\}) = \Psi_{\mathrm{e}}(\{\mathbf{r}\}) \times \Phi_{\mathrm{n}}(\{\mathbf{R}\}), \tag{1.5}$$

where $\Psi_{\mathrm{e}}(\{\mathbf{r}\})$ and $\Phi_{\mathrm{n}}(\{\mathbf{R}\})$ are the electronic and nuclear wavefunction, respectively. This approximation enables us to write the electronic and nuclear problems separately as

$$\hat{H}_{\mathrm{e}}\Psi_{\mathrm{e}}(\{\mathbf{r}\}) = E_{\mathrm{e}}(\{\mathbf{R}\})\Psi_{\mathrm{e}}(\{\mathbf{r}\}), \tag{1.6}$$

$$\hat{H}_{\mathrm{n}}\Phi_{\mathrm{n}}(\{\mathbf{R}\}) = E_{\mathrm{n}}(\{\mathbf{R}\})\Phi_{\mathrm{n}}(\{\mathbf{R}\}), \tag{1.7}$$

[3] C can only be a real number in 3-dimensional space, in 2-dimensional it can be complex and the corresponding particles are called anyons [6].

where the electronic and nuclear Hamiltonians are

$$\hat{H}_e = -\sum_{i=1}^{N} \frac{1}{2}\nabla_i^2 - \sum_{i=1}^{N}\sum_{\mu=1}^{K} \frac{Z_\mu}{|\mathbf{r}_i - \mathbf{R}_\mu|} + \sum_{j>i}^{N} \frac{1}{|\mathbf{r}_i - \mathbf{r}_j|} + \sum_{\mu>\nu}^{K} \frac{Z_\mu Z_\nu}{|\mathbf{R}_\mu - \mathbf{R}_\nu|}, \tag{1.8}$$

$$\hat{H}_n = -\sum_{\mu=1}^{K} \frac{1}{2M_\mu}\nabla_\mu^2 + E_{\mathrm{e}}(\{\mathbf{R}\}). \tag{1.9}$$

Since the electronic wavefunction does not have an explicit dependence on the nuclei positions, the last term in Eq. (1.8) yields a constant energy for each set of fixed nuclei positions. After solving Eq. (1.6) at a set of fixed $\{\mathbf{R}\}$, the electronic energy, which depends on them parametrically, plays the role of an external potential in the Schrödinger equation for the nuclei in Eq. (1.7). The total energy of the system is a sum of the two contributions:

$$E_{\mathrm{total}} = E_e + E_n. \tag{1.10}$$

In this thesis, the electronic problem is solved with fixed nuclei positions using various methods in most cases. Only on the level of the MP2 theory, is the minimisation of the electronic energy with respect to the nuclei positions attempted, see chapter 8. This means that the nuclei positions are updated using the nuclear forces in small steps and the MP2 potential energy surface (PES) $E_e(\{\mathbf{R}\})$ is obtained, where the global minimum is searched for. To facilitate a direct comparison between theoretical predictions and experiments, the influences from EPI also need to be considered, see chapter 7.

1.3 The Electronic Structure Problem in Periodic Solids

The electronic structure problem refers to solving Eq. (1.6) with fixed nuclei positions. Unlike in molecular systems, where the natural boundary condition [4] is applied to the wavefunction, in solids, the periodic boundary condition is often used to reflect the periodicity observed in the arrangement of atoms in crystals. To meaningfully compare with experimental results, all observables calculated from theory should be extrapolated to the thermodynamic limit (TDL), which means an increasingly larger number of particles and larger volumes should be

[4] The wavefunction should vanish at infinity.

simulated, while keeping the ratio between them constant:

$$N \to \infty, \quad V \to \infty, \quad \frac{N}{V} = \text{constant}. \tag{1.11}$$

In solids, this is accomplished by simulating larger and larger supercells, which consist of numerous unit cells, or by sampling a denser and denser k-mesh in the *first Brillouin zone*. This poses a unique scaling problem in solids in comparison with molecules. In the following subsections, some basic notions, including *unit cell*, *supercell*, the *first Brillouin zone* and the *k-mesh* sampling the *first Brillouin zone*, and the *Bloch's theorem* in solid state physics will be introduced.

1.3.1 Bravais Lattice and Periodic Boundary Condition

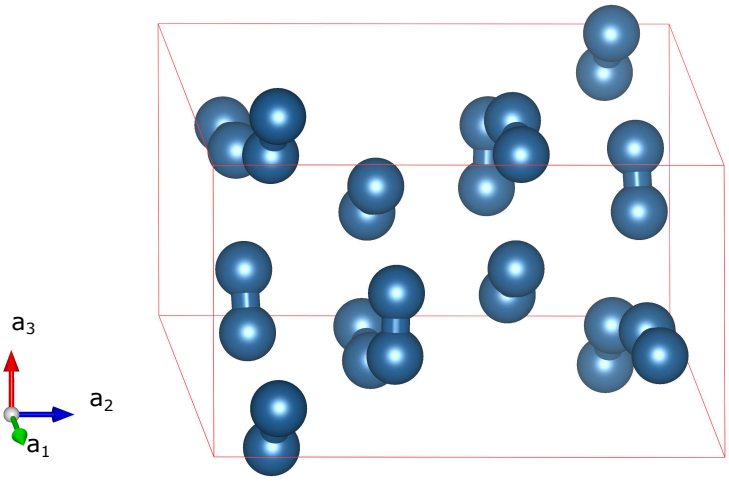

FIGURE 1.1: The primitive unit cell containing 24 hydrogen atoms of the phase C2c-24 at 100 GPa optimised by MP2 forces. The red lines show the boundary of the unit cell. Some atoms from the neighbouring cells are included to show the complete molecular bonds.

A *primitive unit cell* in a solid is the smallest unit that can be repeated in three directions to construct the solid. The choice of the *primitive unit cell* in a solid is not unique, however all possible choices have the same volume Ω. In Fig. 1.1, the *primitive unit cell* of a model phase for solid hydrogen at 100 GPa is shown for example. The shape of a unit cell is defined by three basis vectors $\mathbf{a}_i$, $i = 1, 2, 3$. All crystals can be constructed by repeating the primitive unit

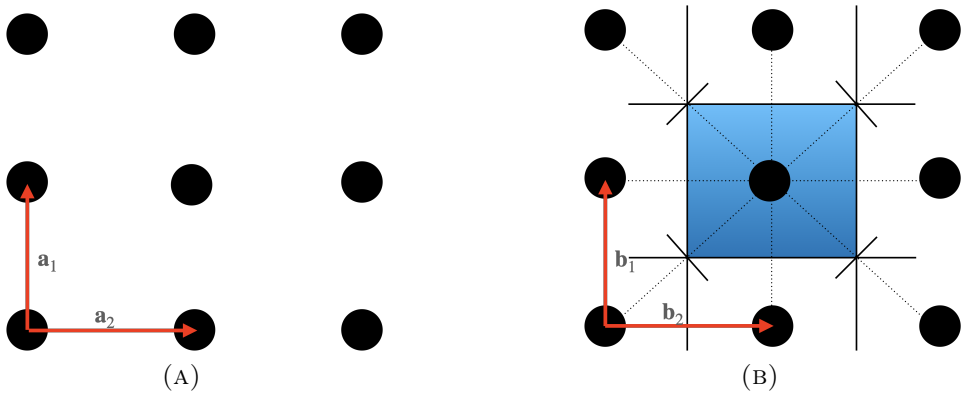

FIGURE 1.2: (A): 2D square Bravais lattice. (B): Reciprocal lattice of the 2D square lattice and the corresponding first Brillouin zone (shaded in blue).

cell in all three directions [5]. Each repetition can be identified as a point on the *Bravais lattice*:

$$\mathbf{L} = \sum_{i=1}^{3} n_i \mathbf{a}_i, \quad n_i \in \mathcal{Z}. \tag{1.12}$$

In association to the Bravais lattice, one can define a reciprocal lattice via the relation $e^{i\mathbf{L}\cdot\mathbf{K}} = 1$ and $\mathbf{a_i} \cdot \mathbf{b}_j = 2\pi\delta_{i,j}$:

$$\mathbf{K} = \sum_{i=1}^{3} \tilde{n}_i \mathbf{b}_i, \quad \tilde{n}_i \in \mathcal{Z}, \tag{1.13}$$

where $\mathbf{b}_i$, $i = 1, 2, 3$, are the three basis vectors for the reciprocal cell. The first Brillouin zone is defined as the area enclosed by the bisection lines (planes) between one lattice point and its nearest surrounding points in reciprocal space. In Fig. 1.2, an example of a 2D square Bravais lattice, its reciprocal lattice and the corresponding first Brillouin zone are shown.

In reality, one cannot simulate an infinitely large solid. So normally a *supercell* containing $N_p = N_1 N_2 N_3$ unit cells is simulated, where N_1, N_2, N_3 are the number of unit cells in x, y, z directions respectively; in addition, the single-particle wavefunction is required to fulfill the periodic or *Born-von Karman* boundary condition, which reads

$$\psi(\mathbf{r} + N_i \mathbf{a}_i) = \psi(\mathbf{r}), \quad i = 1, 2, 3. \tag{1.14}$$

[5] In 3 dimensional space, there are in total 14 different Bravais lattices.

1.3.2 Bloch's Theorem

Theorem 1.3.1. *The eigenstates ψ of a single-particle Hamiltonian, which contains only a periodic potential $U(\mathbf{r}+\mathbf{L}) = U(\mathbf{r})$, can be written as a product of a plane wave and a function with periodicity of the Bravais lattice $\mathbf{L}$:*

$$\psi(\mathbf{r}) = e^{\mathrm{i}\mathbf{k}\cdot\mathbf{r}} u(\mathbf{r}), \tag{1.15}$$

where $u(\mathbf{r}+\mathbf{L}) = u(\mathbf{r})$.

We follow the definition of the theorem, Eq. (8.3), in Ref. [7] and refer to the proofs therein. In combination with the periodic boundary condition introduced in the previous subsection, we can find the possible values of $\mathbf{k}$ defined by a supercell by plugging Eq. (1.15) into Eq. (1.14):

$$\begin{aligned} \psi(\mathbf{r}+N_i\mathbf{a}_i) &= e^{\mathrm{i}N_i\mathbf{k}\cdot\mathbf{a}_i} e^{\mathrm{i}\mathbf{k}\cdot\mathbf{r}} u(\mathbf{r}+N_i\mathbf{a}_i) \\ &= e^{\mathrm{i}N_i\mathbf{k}\cdot\mathbf{a}_i} e^{\mathrm{i}\mathbf{k}\cdot\mathbf{r}} u(\mathbf{r}) \\ &= e^{\mathrm{i}N_i\mathbf{k}\cdot\mathbf{a}_i} \psi(\mathbf{r}), \end{aligned} \tag{1.16}$$

and if the expression in the last line is to satisfy the periodic boundary condition, the following has to be true:

$$e^{\mathrm{i}N_i\mathbf{k}\cdot\mathbf{a}_i} = 1 \implies N_i\mathbf{k}\cdot\mathbf{a}_i = 2m_i\pi, \quad m_i \in \mathcal{Z}. \tag{1.17}$$

By decomposing $\mathbf{k}$ using the reciprocal lattice vectors as $\mathbf{k} = \sum_{i=1}^{3} x_i\mathbf{b}_i$, we find that

$$x_i = \frac{m_i}{N_i}. \tag{1.18}$$

Normally we restrict $|m_i| < |N_i|$, so that the k-points are within the first Brillouin zone. In practice, in terms of the system size, simulating a supercell with $N_p = N_1N_2N_3$ unit cells but with the first Brillouin zone sampled by only one k-point is equivalent to simulating a single unit cell but with the first Brillouin zone sampled by $N_p = N_1N_2N_3$ k-points. However, within the latter approach the momentum conservation can be used to reduce the computational cost drastically, albeit with some implementation complexity.

1.3.3 Three Dimensional Uniform Electron Gas

The 3D UEG is the simplest model for realistic periodic solids, of which the Hamiltonian in real space reads

$$\hat{H} = -\sum_i \frac{1}{2}\nabla_i^2 + \sum_{i\neq j} \frac{1}{|\mathbf{r_i} - \mathbf{r_j}|} + \text{const.}, \tag{1.19}$$

where the const. includes the interactions between electrons and the homogenous positive background charge, and the interactions between the electrons and their own periodic images, which is termed as the Madelung constant and will disappear as the size of the simulation cell goes to infinity. Atomic units are used to simplify the equations. When plane wave basis functions and a simple cubic simulation cell of volume $\Omega = L^3$ are used, we can reformulate the Hamiltonian in a second-quantized form,

$$\hat{H} = \sum_p \sum_\sigma \frac{1}{2}\mathbf{k}_p^2 a_{p,\sigma}^\dagger a_{p,\sigma} + \frac{1}{2}\sum_{pqrs}\sum_{\sigma\sigma'} V_{pq}^{rs} a_{p,\sigma}^\dagger a_{q,\sigma'}^\dagger a_{s,\sigma'} a_{r,\sigma}, \tag{1.20}$$

where for simplicity we use $p, q, r, s \ldots$ indices as a compact form for the general momentum (plane wave basis function) indices $\mathbf{k}_p, \mathbf{k}_q, \mathbf{k}_r, \mathbf{k}_s \ldots$ and hereon we use the two terms plane wave basis function and orbital equivalently. We stress that due to momentum conservation, i.e. $\mathbf{k} \equiv \mathbf{k}_r - \mathbf{k}_p = \mathbf{k}_q - \mathbf{k}_s$, there are only three free indices among $pqrs$, and the interactions with the homogenous positive background charge are cancelled by the divergent Coulomb potential at $k = 0$, which is defined as $V_{pq}^{rs} \equiv V(\mathbf{k}) = \frac{4\pi}{\Omega \mathbf{k}^2}$. We also ignore the Madelung contribution in the Hamiltonian which can be added posteriorly to the ground state energy. The electron density of the system can be described by the Wigner-Seitz radius $r_s = \left(\frac{3}{4\pi N}\right)^{1/3} L$, where N is the number of electrons.

Chapter 2

Mean Field Theories

The analytical solution to the electronic Schrödinger equation is only possible for very few limited cases, e.g. the hydrogen atom. So, in the early days after the discovery of the Schrödinger equation, people have tried various approximations. In his pioneering work, Hartree attempted to approximate the true many-electron wavefunction by using a product of single-particle functions in 1928 [8], where he imposed the Pauli exclusion principle so that two electrons cannot occupy the same single-particle function. However, this formulation does not respect the more fundamental antisymmetry requirement on the fermionic wavefunction, as pointed out by Slater and Fock in 1930 [9, 10]. Later the Hartree-Fock theory using a Slater determinant as an ansatz came into being [11]. On the other hand, there was a parallel paradigm going on which uses the electronic density instead of the wavefunction to solve the Schrödinger equation. The earliest model along this line is the Thomas-Fermi model [12, 13], which is the precursor of the later well-known DFT. In this chapter, these two important mean-field theories that lay the foundation for many others are going to be introduced. In general, mean field theories replace the Coulomb interactions between electrons in the many-electron Hamiltonian, Eq. (1.8), with an effective potential to form a mean-field Hamiltonian,

$$\hat{H}_{\mathrm{MF}} = \hat{h} + \hat{v}_{\mathrm{eff}}(\mathbf{r}), \tag{2.1}$$

where the Coulomb potential among the nuclei is ignored and can be added to the total energy at a later point; and all the single-particle operators are put together as

$$\hat{h} = -\frac{1}{2}\nabla^2 - \sum_{\mu=1}^{K} \frac{Z_\mu}{|\mathbf{r} - \mathbf{R}_\mu|}. \tag{2.2}$$

2.1 Hartree-Fock Theory

The HF employs a single Slater determinant as the ansatz for the true many-electron ground state wavefunction, the optimisation of which is normally cast into a self-consistent field framework. Fundamentally, HF can be categorised as one of the many variational methods which utilises the variational principle.

2.1.1 The Variational Principle

The variational principle is a very powerful tool in that it gives an upper bound to the ground state energy, which not only permits a possibility for systematic improvement in the employed ansatz, but can also provide estimates for errors. It is the most crucial element in a host of methods, besides HF, such as density matrix renormalisation group (DMRG) theory[1] [14] and variational Monte Carlo (VMC) [15].

Given an arbitrary wavefunction Ψ_a under the normalisation requirement that $\langle\Psi_\mathrm{a}|\Psi_\mathrm{a}\rangle = 1$, the Rayleigh quotient functional is defined as

$$E(\Psi_\mathrm{a}) = \langle\Psi_\mathrm{a}|\hat{H}|\Psi_\mathrm{a}\rangle\,. \tag{2.3}$$

The variational principle then states that this functional satisfies the following condition:

$$E(\Psi_\mathrm{a}) \geq E_0, \tag{2.4}$$

where E_0 is the ground state energy of $\hat{H}$.

Proof. The eigendecomposition of the arbitrary ansatz is

$$|\Psi_\mathrm{a}\rangle = \sum_i C_i\,|\Psi_i\rangle\,, \quad \sum_i |C_i|^2 = 1, \tag{2.5}$$

where $|\Psi_i\rangle$ are the eigen states of $\hat{H}$, which satisfy $\hat{H}\,|\Psi_i\rangle = E_i\,|\Psi_i\rangle$ and $\langle\Psi_i|\Psi_j\rangle = \delta_{i,j}$. Plugging the eigendecomposition of the arbitrary ansatz into

[1] The canonical formulation uses the variational principle, but the theory can be formulated in a way that also work with non-hermitian Hamiltonians.

the Rayleigh quotient, Eq. (2.3), one obtains

$$\begin{aligned} E(\Psi_{\mathrm{a}}) &= \sum_i \sum_j C_i^* C_j \langle \Psi_i | \hat{H} | \Psi_j \rangle \\ &= \sum_i \sum_j C_i^* C_j E_j \delta_{i,j} \\ &= \sum_i |C_i|^2 E_i \geq \sum_i |C_i|^2 E_0 = E_0. \end{aligned} \tag{2.6}$$

□

2.1.2 Basis Set and Slater Determinant

In solids, plane waves are usually used as the basis set and a linear combination of the basis functions is used to represent a single-particle function [2]. Plane waves are naturally orthonormal

$$\begin{aligned} \langle \phi_{\mathbf{G}}(\mathbf{r}) | \phi_{\mathbf{G}'}(\mathbf{r}) \rangle &= \int e^{-\mathrm{i}\mathbf{G}\cdot\mathbf{r}} e^{\mathrm{i}\mathbf{G}'\cdot\mathbf{r}} \mathrm{d}\mathbf{r} \\ &= \delta_{\mathbf{G},\mathbf{G}'}. \end{aligned} \tag{2.7}$$

The number of them included inside of the basis set can be easily controlled by a single parameter–the plane wave energy cutoff:

$$\frac{|\mathbf{k}_i + \mathbf{G}|^2}{2} \leq E_{\mathrm{cutoff}}, \tag{2.8}$$

where $\mathbf{k}_i$ are the k-points sampling the first Brillouin zone and all the plane wave momentum vectors, $\mathbf{G}$, that satisfy the unit cell periodicity and this condition will be included as basis functions. So any single-particle wavefunction can be expanded in plane waves as

$$\varphi_i(\mathbf{r}) = \frac{1}{\sqrt{\Omega}} \sum_{\mathbf{G}} C_{n_i,\mathbf{k}_i}(\mathbf{G}) e^{\mathrm{i}(\mathbf{k}_i+\mathbf{G})\cdot\mathbf{r}}, \tag{2.9}$$

where $C_{n_i,\mathbf{k}_i}$ are the coefficients, Ω is the volume of the unit cell and the composite index $i = \{n_i, \mathbf{k}_i\}$ contains the information on both the index of the band (index of orbitals in quantum chemistry language) and the index of the k-point. In the later part of this thesis, the index i of a single-particle wavefunction/energy will be used for simplicity and the composite indices will be used where necessary for clarity.

[2] Sometimes in combination with some other framework such as the *projector augmented wave (PAW)* method to treat the oscillatory behavior of the single-particle wavefunction in regions close to the nuclei, whose details will not be covered in this thesis.

A Slater determinant is nothing but a normalised and antisymmetrised product of functions , satisfying the antisymmetry requirement for fermions. It is expressed as

$$D(\mathbf{x}_1, \mathbf{x}_2, \ldots, \mathbf{x}_N) = \frac{1}{\sqrt{N!}} \begin{vmatrix} \chi_1(\mathbf{x}_1) & \chi_2(\mathbf{x}_1) & \ldots & \chi_N(\mathbf{x}_1) \\ \chi_1(\mathbf{x}_2) & \chi_2(\mathbf{x}_2) & \ldots & \chi_N(\mathbf{x}_2) \\ \vdots & \vdots & \ddots & \vdots \\ \chi_1(\mathbf{x}_N) & \chi_2(\mathbf{x}_N) & \ldots & \chi_N(\mathbf{x}_N) \end{vmatrix}, \tag{2.10}$$

where $\mathbf{x}_i = \{\mathbf{r}_i, \omega\}$ carries the position and spin degrees of freedom and $\chi_I(\mathbf{x}) = \varphi_i(\mathbf{r})\sigma_i(\omega)$, which is a product of the *spatial orbital* and a spin function, is called the *spin orbital*. The spin functions satisfy the orthogonality relation via the formal integration over an augmented spin variable ω as follows

$$\int \sigma_i(\omega)\sigma_j(\omega)\mathrm{d}\omega = \delta_{\sigma_i,\sigma_j}, \tag{2.11}$$

which in practice means that if two electrons have different spins, say one with spin up and the other with spin down, the above relation gives 0, otherwise 1.

There are two other simplified forms of a Slater determinant which might appear in other contexts. One is the diagonal representation:

$$D(\mathbf{x}_1, \mathbf{x}_2, \ldots, \mathbf{x}_N) = |\chi_1(\mathbf{x}_1), \chi_2(\mathbf{x}_2), \ldots, \chi_N(\mathbf{x}_N)\rangle\,; \tag{2.12}$$

the other one is the occupation representation:

$$D(\mathbf{x}_1, \mathbf{x}_2, \ldots, \mathbf{x}_N) = |\overbrace{\underbrace{11\ldots1}_{N \text{ electrons}}\ 00\ldots0}^{M \text{ spin orbitals}}\rangle\,, \tag{2.13}$$

for which there is a common pictorial representation as shown in Fig. 2.1 for a Slater determinant that has the lowest N spin orbitals occupied and one that is singly excited. This occupation representation will be very useful for the introduction of the second quantization in the later part of this thesis. Following conventions, capital and lowercase letters are used to represent spin-orbitals and spatial orbitals, respectively. In particular, $I, J, K\ldots$ $(i, j, k\ldots)$ are used to represent occupied spin orbitals (spatial orbitals) and $A, B, C\ldots$ $(a, b, c\ldots)$ are used to represent unoccupied [3] spin orbitals (spatial orbitals) in the reference determinant. For general spin orbitals (spatial orbitals), $O, P, Q, \ldots$ $(o, p, q, \ldots)$ indices are used.

[3] The unoccupied orbitals are also referred to as virtual orbitals.

FIGURE 2.1: A reference Slater determinant that has the lowest N spin orbitals occupied (left). A singly excited Slater determinant that has an electron removed from the Ith spin orbital and elevated onto the Ath spin orbital (right).

2.1.3 Self-consistent Field Equation

In HF, the goal is to minimise the energy as a functional of the single-particle functions inside of a single Slater determinant,

$$E_{\mathrm{HF}}(\{\chi\}) = \langle D|\hat{H}_e|D\rangle\,. \tag{2.14}$$

This is achieved by requiring that $\frac{\delta E_{\mathrm{HF}}(\{\chi_I\})}{\delta \chi_I} = 0$ under the constraint that the spatial functions are also orthonormal, $\langle\varphi_i|\varphi_j\rangle = \delta_{i,j}$, along with the preexisting orthonormal condition for the spins. This condition yields the following equation [16]

$$\hat{h}\chi_I(\mathbf{x}) + \sum_{J\neq I}^{N}\left[\int \mathrm{d}\mathbf{x}'\,|\chi_J(\mathbf{x}')|^2\,\tfrac{1}{|\mathbf{r}'-\mathbf{r}|}\right]\chi_I(\mathbf{x}) - \sum_{J\neq I}^{N}\left[\int \mathrm{d}\mathbf{x}'\chi_J^*(\mathbf{x}')\chi_I(\mathbf{x}')\tfrac{1}{|\mathbf{r}'-\mathbf{r}|}\right]\chi_J(\mathbf{x}) = \epsilon_I\chi_I(\mathbf{x}), \tag{2.15}$$

which can be recast into an eigenvalue problem by defining the *Fock operator*

$$\hat{f} = \hat{h} + \hat{v}^{\mathrm{HF}}(\mathbf{x}), \tag{2.16}$$

where

$$\hat{v}^{\mathrm{HF}}(\mathbf{x}) = \sum_{J\neq I}^{N} \int \mathrm{d}\mathbf{x}' \, |\chi_J(\mathbf{x}')|^2 \frac{1}{|\mathbf{r}'-\mathbf{r}|} - \sum_{J\neq I}^{N} \int \mathrm{d}\mathbf{x}' \chi_J^*(\mathbf{x}') \frac{1}{|\mathbf{r}'-\mathbf{r}|} \hat{\mathcal{P}}(\mathbf{x},\mathbf{x}')\chi_J(\mathbf{x}'), \tag{2.17}$$

and the exchange operator $\hat{\mathcal{P}}(\mathbf{x},\mathbf{x}')\chi_J(\mathbf{x}')\chi_I(\mathbf{x}) = \chi_J(\mathbf{x})\chi_I(\mathbf{x}')$. The HF eigenproblem

$$\hat{f}\chi_I(\mathbf{x}) = \epsilon_I \chi_I(\mathbf{x}) \tag{2.18}$$

cannot be diagonalised directly and must be solved iteratively, because the Fock operator depends on the desired eigenvectors. The variation of the orbital functions is achieved by changing the expansion coefficients in Eq. (2.9) so that the energy decreases. In the plane wave basis, Eq. (2.18) can be rewritten as

$$\sum_{\mathbf{G}'} F_{\mathbf{G},\mathbf{G}'} C_I(\mathbf{G}') = \epsilon_I C_I(\mathbf{G}'), \tag{2.19}$$

where $F_{\mathbf{G},\mathbf{G}'} = \int \mathrm{d}\mathbf{r} e^{-\mathrm{i}\mathbf{G}\cdot\mathbf{r}} \hat{f} e^{\mathrm{i}\mathbf{G}'\cdot\mathbf{r}}$ is the *Fock matrix*. A simplistic way to solve this equation is to

1. start from a random guess of the coefficients $C_I(\mathbf{G})$ and construct the Fock matrix;
2. diagonalise the Fock matrix to obtain a new set of $C_I(\mathbf{G})$ and ϵ_I;
3. construct a new Fock matrix using the new $C_I(\mathbf{G})$ from the previous step and repeat step 2 until convergence.

After the eigenvectors and the eigenvalues are obtained, the eigenvalues ϵ_I can be defined as the orbital energy of the orbital χ_I. The HF energy can be expressed as

$$E_{\mathrm{HF}} = \sum_{I}^{N} \epsilon_I - \frac{1}{2} \sum_{I,J}^{N} \left(\langle IJ|IJ\rangle - \langle IJ|JI\rangle \right), \tag{2.20}$$

where

$$\begin{aligned}
\langle IJ|IJ\rangle &= \int\int \mathrm{d}\mathbf{x}\mathrm{d}\mathbf{x}' \left|\chi_I(\mathbf{x})\right|^2 \frac{1}{|\mathbf{r}'-\mathbf{r}|} \left|\chi_J(\mathbf{x}')\right|^2 \\
&= \int\int \mathrm{d}\mathbf{r}\mathrm{d}\mathbf{r}' \left|\varphi_i(\mathbf{r})\right|^2 \frac{1}{|\mathbf{r}'-\mathbf{r}|} \left|\varphi_j(\mathbf{r}')\right|^2 \\
&\equiv \langle ij|ij\rangle\,, \\
\langle IJ|JI\rangle &= \int\int \mathrm{d}\mathbf{x}\mathrm{d}\mathbf{x}' \chi_I^*(\mathbf{x})\chi_J(\mathbf{x}) \frac{1}{|\mathbf{r}'-\mathbf{r}|} \chi_J^*(\mathbf{x}')\chi_I(\mathbf{x}') \\
&= \int\int \mathrm{d}\mathbf{r}\mathrm{d}\mathbf{r}' \varphi_i^*(\mathbf{r})\varphi_j(\mathbf{r}) \frac{1}{|\mathbf{r}'-\mathbf{r}|} \varphi_j^*(\mathbf{r}')\varphi_i(\mathbf{r}')\delta_{\sigma_i,\sigma_j} \\
&\equiv \langle ij|ji\rangle\, \delta_{\sigma_i,\sigma_j}.
\end{aligned} \tag{2.21}$$

In this thesis, only *closed-shell* systems are of interests, where the lowest $N/2$ spatial orbitals are doubly occupied. For such systems, the HF energy can be expressed as

$$E_{\mathrm{HF}} = 2\sum_{i}^{N/2} \epsilon_i - \sum_{i,j}^{N/2} \left(2\langle ij|ij\rangle - \langle ij|ji\rangle\right), \tag{2.22}$$

where the spin degrees of freedom have been integrated over, so that the indices i, j run over spatial orbitals. Once the converged HF solution is found, the virtual-virtual block of the Fock matrix can be constructed, by diagonalising which the virtual orbitals, φ_a, can be obtained, along with their corresponding eigenenergies, ϵ_a. These virtual orbitals will be used to construct excited Slater determinants, along with the HF determinant, which form the basis to expand the many-electron wavefunction.

2.2 Kohn-Sham Density Functional Theory

Similar to the HF eigenproblem Eq. (2.18), DFT treats the many-electron problem as an interaction free eigenproblem by introducing an XC functional to approximate the interactions among electrons, which yields the famous *Kohn-Sham (KS)* equation

$$\left(\hat{h} + V_{\mathrm{KS}}(\mathbf{r})\right)\varphi_p(\mathbf{r}) = \epsilon_p\varphi_p(\mathbf{r}), \tag{2.23}$$

The potential $V_{\mathrm{KS}}(\mathbf{r})$ contains the Hartree term and the XC functional as follows

$$V_{\mathrm{KS}}(\mathbf{r}) = \int \mathrm{d}\mathbf{r}' \frac{n(\mathbf{r}')}{|\mathbf{r}'-\mathbf{r}|} + V_{\mathrm{XC}}[n(\mathbf{r})], \tag{2.24}$$

where the electron density is related to the normalised many-electron wavefunction as follows

$$n(\mathbf{r}) = N \int \mathrm{d}\mathbf{r}_2 \cdots \int \mathrm{d}\mathbf{r}_N \, \Psi^*(\mathbf{r}, \mathbf{r}_2, \ldots, \mathbf{r}_N)\Psi(\mathbf{r}, \mathbf{r}_2, \ldots, \mathbf{r}_N). \tag{2.25}$$

When the many-electron wavefunction is approximated by a normalised Slater determinant constructed by orthonormal single-particle orbitals, the electron density is simply $n(\mathbf{r}) = \sum_{i=1}^{N} \int \mathrm{d}\mathbf{r} |\varphi_i(\mathbf{r})|^2$, which is the sum of the densities of the N electrons in their corresponding orbitals. Therefore the equivalence between the Hartree term in Eq. (2.24) and the first term in the HF potential $v^{\mathrm{HF}}(\mathbf{r})$ defined in Eq. (2.17) is established. So the only difference between DFT and HF resides in the second term in their respective potentials. The XC potential in DFT is a functional of the electron density which itself depends on the desired single-particle wavefunctions. So the KS equations are also solved iteratively. In practice, the functional form of the XC potential is designed based on some emperical or physical arguments to approximate the many-body correlation effects. When it is chosen to be the same exchange potential [4] as in $v^{\mathrm{HF}}(\mathbf{r})$, one returns to the HF problem.

DFT has been the workhorse in material science over the years due to its low computational cost and, in some cases, satisfactory accuracy. However, due to its lack of systematical improvability, in recent years its shortcomings are becoming more obvious in comparison to other systematically improvable methods such as QMC and quantum chemistry methods. For example, different XC functionals often provide different, sometimes contradictory, results on the same problem, and the errors on different phases using the same functional are not so consistent, which renders the studies on establishing reliable phase diagrams extremely hard. In the comparative study on the solid hydrogen phases in chapter 10, the advantages and shortcomings of DFT will be discussed in a more concrete context, in comparison with other methods, such as HF, CCSD and DMC.

[4] In the DFT community, it is called the exact exchange functional.

Chapter 3

Electronic Correlations

The HF solution to the many-electron Schrödinger equation is fast and sometimes provides some insights to a system. However, often it is insufficient in describing the correct physics. Because it treats the electron-electron interactions as an averaged one-particle potential. Hence it ignores a large part of the correlations among electrons [1]. To gauge how many correlations are absent in the reference wavefunction (normally it is the HF wavefunction), the correlation energy is defined as [17]

$$E_{\mathrm{c}} \equiv E_{\mathrm{exact}} - E_{\mathrm{HF}}. \tag{3.1}$$

However this definition is not so practical when the exact ground state energy E_{exact} is not known beforehand. So a more practical way is to define a method dependent correlation energy as follows

$$E^{\mathrm{c}}_{\mathrm{method}} \equiv E_{\mathrm{method}} - E_{\mathrm{HF}}. \tag{3.2}$$

For a variational method, the lower the correlation energy it gets, the closer it is to the exact ground state energy. In the following sections, we will discuss the origins of dynamical (short-range) correlations and static correlations.

3.1 Weak Dynamical Correlations and the Cusp Condition

Due to the repulsive Coulomb potential, electrons should in principle avoid getting too close to each other. This effect should show up as the decaying amplitude of the wavefunction as two electrons approach each other. To be more precise, the condition on the wavefunction at the point where two electrons collide was analytically determined by Kato in 1957 [18], which is now termed

[1] It has the correct exchange correlations due to the anti-symmetry of the Slater determinant

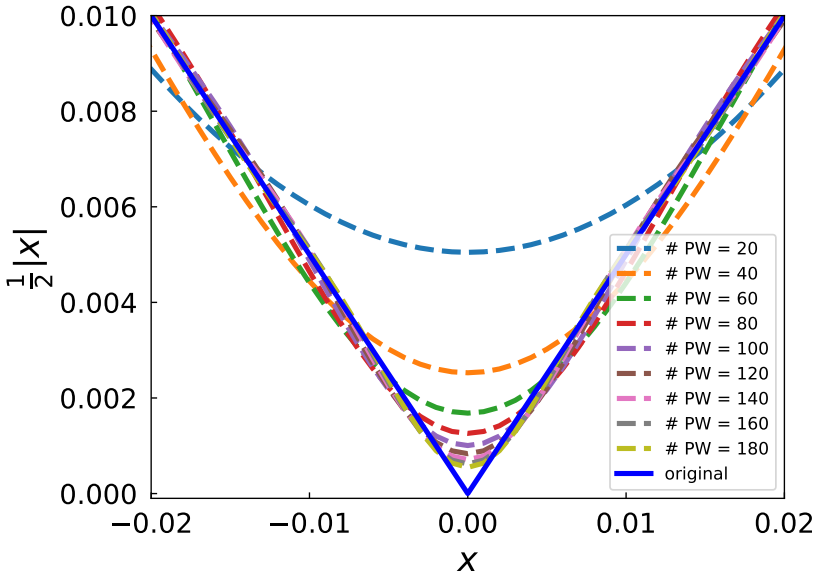

FIGURE 3.1: An example of wavefunction at the electron coalescence point. The function $\frac{1}{2}|x|$ is reconstructed with increasing numbers of plane waves. It requires a lot of high frequency plane waves to resolve the sharp cusp.

the *Kato cusp* condition (for a singlet pair),

$$\left.\frac{\partial \Psi^{\text{avg}}}{\partial \mathbf{r_{ij}}}\right|_{\mathbf{r_{ij}}=0} = \frac{1}{2}\Psi(\mathbf{r_{ij}}=0), \tag{3.3}$$

where the superscript avg denotes the spherical average of the wavefunction. However, in the HF wavefunction, this sharp cusp is absent. To recover this physical behavior, one needs to resort to theories that are more flexible in representing the wavefunction. As shown in literature, a simple perturbation theory can restore the cusp in the wavefunction [19], albeit with a large number of plane waves (or other basis functions). To illustrate this, in Fig. 3.1, the cusp function $f(x) = \frac{1}{2}|x|$ is reconstructed by using increasingly many plane waves in the Fourier series expansion. Although it is not a physical wavefunction, this example demonstrates the essence of requiring a large number of smooth basis functions in real systems to resolve the sharp cusp in the wavefunction in order to reach convergence for the calculated energy and other properties. The *complete basis set (CBS)* limit is thus defined as the basis set that contains an infinite number of basis functions, at which every property calculated is converged. The correlations that are mostly due to the short-range cusp condition, which can be captured by methods that are based on a single reference determinant, are normally classified as the *dynamical* or *weak* correlations.

Correlations that are beyond the capability of the single-reference methods are generally termed static or strong correlations. In the next section, the origin of this type of correlations will be explored.

3.2 Strong Correlations

In contrast to weakly correlated systems which can be accurately described by single-reference post-HF methods, strongly correlated systems normally exhibit a multi-reference nature. The descriptions of these systems given by single-reference methods are not even qualitatively correct. The full configuration interaction (FCI) method provides the most general ansatz for the true many-electron ground state wavefunction via a linear combination of Slater determinants (SD)

$$|\Psi\rangle = \sum_i C_i \, |D_i\rangle \,, \tag{3.4}$$

where all possible Slater determinant (SD)s constructed for N electrons in M (orthogonal) spin orbitals are summed over, as illustrated in Fig. 2.1. The total number is calculated as the number of possible combinations of selecting N elements out of a total M elements, which is $\frac{M!}{N!(M-N)!}$ and in practice quickly grows larger than the number of bytes of storage in the whole world. For this reason alone, essentially exact FCI solutions are only available for very small systems.

Nevertheless, FCI provides a convenient way to represent the many-electron Hamiltonian as a matrix and the wavefunction as a vector

$$\mathbf{HC} = E\mathbf{C}, \tag{3.5}$$

which can be modeled using small matrices to explore the origin of strong correlations. We set up our model (symmetric) Hamiltonian matrix based on the following parameters/rules:

1. The dimension of the matrix: N.
2. The gaps between neighboring diagonal matrix elements: $\Delta_i^{i+1} \geq 0$; and the first diagonal element is set to 0.
3. The probability of an off-diagonal element to be nonzero: $0 < p_{\text{off}} \leq 1$.
4. The magnitude of a nonzero off-diagonal elements: $M_{\text{off}} > 0$.
5. The sign of each nonzero off-diagonal element is randomly assigned to be positive or negative with equal probability.

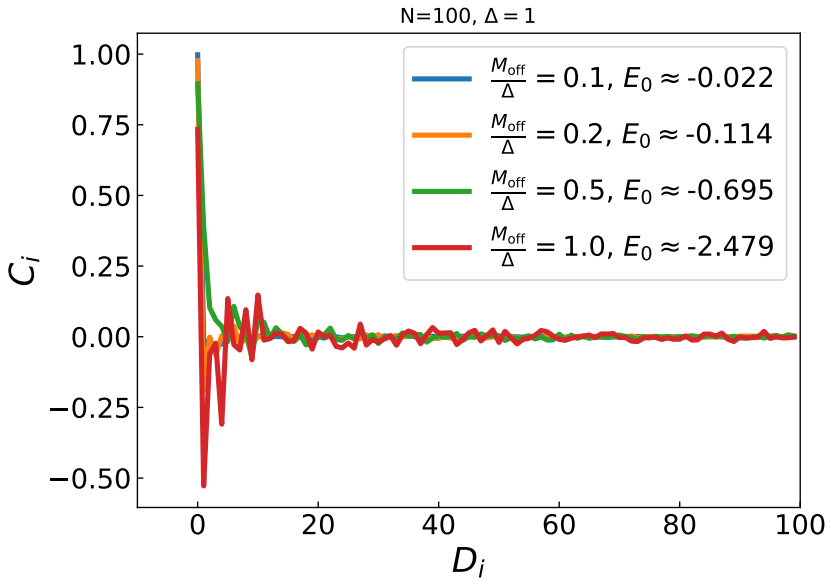

FIGURE 3.2: Ground state eigenvectors corresponding to model Hamiltonians with increasing diagonal elements at a fixed step $\Delta = 1$ and different values of the off-diagonal magnitude M_{off}. Dense matrices with size 100×100 are used by setting $p_{\text{off}} = 1$. E_0 refers to the lowest eigenenergies in the matrices.

First, in Fig. 3.2 the ground state eigenvectors are shown, which belong to matrices with varying ratios of $\frac{M_{\text{off}}}{\Delta}$ and constant gaps between neighboring diagonal elements, i.e. $\Delta_i^{i+1} = \Delta = 1$. To restrict the number of variables, $p_{\text{off}} = 1$ is used for now, which generates dense matrices with all off-diagonal elements having magnitude M_{off} and randomly determined signs. After diagonalising the matrices, the eigenvectors corresponding to the lowest eigenvalues are retrieved, where we normalise the wavefunctions such that the total weight of a wavefunction is $\sum_i^N \sqrt{C_i^2} = 1$. We notice that the weight of the "HF" determinant D_0 keeps dropping and the ground state wavefunction has more weights distributed on excited determinants when the ratio $\frac{M_{\text{off}}}{\Delta}$ increases, which simulates the physical situation when the Coulomb interactions that are not captured by the mean-field solution are large.

Next, we investigate the effect of the number of nonzero terms in the off-diagonal elements. For this purpose, 20 pairs of M_{off} and p_{off} are generated independently; and for each pair, 500 random matrices of size 100×100 are generated accordingly. The ground state eigenvectors of those matrices are calculated, so that the weight of the "HF" determinant as a function of $p_{\text{off}} M_{\text{off}}$ can be found, as shown in Fig. 3.3. The product $p_{\text{off}} M_{\text{off}}$ can be seen as the total interaction strength. For all matrices, $\Delta_i^{i+1} = 1$ is set. The weight of the "HF" determinant falls sharply when $p_{\text{off}} M_{\text{off}}$ goes from 0 to 1 and then

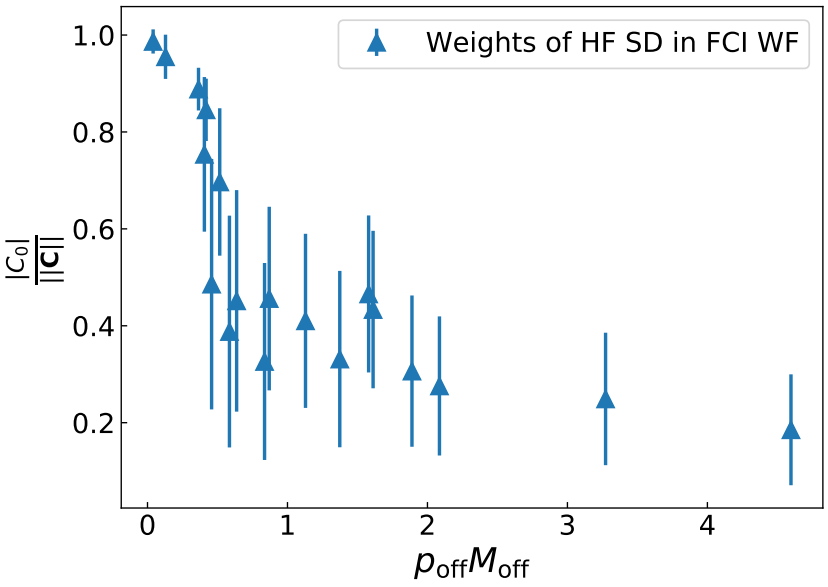

FIGURE 3.3: The average weight of "HF" determinant in the FCI wavefunction as a function of $p_{\text{off}}M_{\text{off}}$, retrieved from the ground state eigenvectors of randomly generated matrices according to $N = 100$, $\Delta_i^{i+1} = 1$, p_{off} and M_{off}. In total, 20 pairs of random p_{off} and M_{off} values are used, and for each pair 500 random matrices are generated. The mean value and the standard deviation at each point are calculated from the corresponding set of 500 random samples.

keeps dropping but slower as the total interaction strength further increases. At around 0.5 total interaction strength, the "HF" weight falls below 50%. One can therefore use this point as the dividing line between weak and strong interaction regions.

So far only situations where there are finite gaps between diagonal elements are investigated. Even in these cases strong correlations (multi-reference nature) can occur when there are many nonzero and large off-diagonal elements. We now investigate the case when there are weak interactions while some degeneracies happen in the diagonal elements, which can occur in real systems due to symmetries. For simplicity, we can set $p_{\text{off}} = 1$ and scan M_{off} among the three values of $0.001, 0.01, 0.1$ to ensure that the interactions are weak, whilst setting the first 10 diagonal elements to be 0 to mimic the degeneracies generated by symmetries or accidents [2], and increasing the rest of the diagonal elements by a fixed step size of $\Delta_i^{i+1} = 1$. In Fig. 3.4, the ground state

[2]For degeneracies generated strictly by symmetries, not only the diagonal elements are the same, but also the surrounding environment should be the same. As a result, determinants belonging to the same symmetry should have the same weight in the wavefunction. Without loss of generality, only the diagonal elements are considered here.

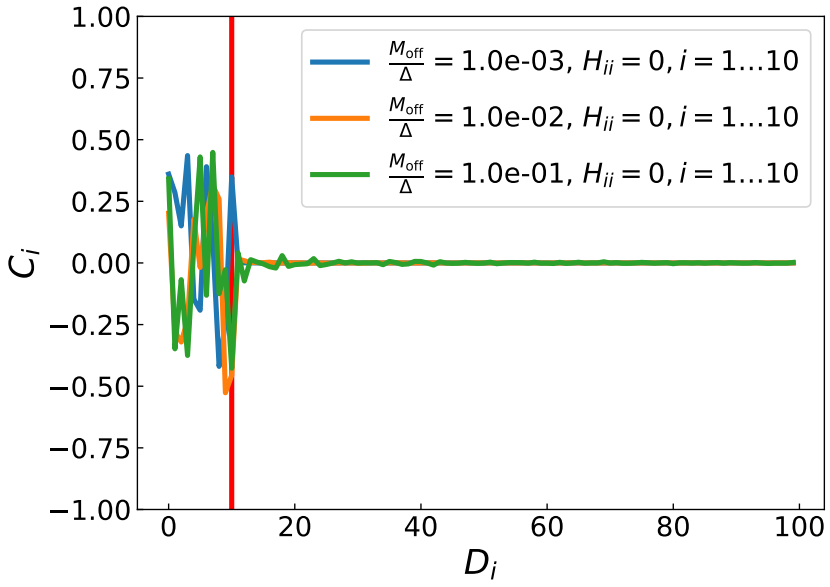

FIGURE 3.4: The ground state eigenvectors of three randomly generated matrices with parameters $N = 100$, $p_{\text{off}} = 1$ and $M_{\text{off}} = 0.001, 0.01, 0.1$. The first 10 diagonal elements of the matrices are set to 0 to define a degenerate space and the rest of the diagonal elements are increased by a fixed step of $\Delta_i^{i+1} = 1$. The vertical red line is set at $i = 10$ to visually separate the degenerate space and the rest.

eigenvectors of these random matrices are shown. The red vertical line is at $i = 10$ to separate the degenerate space and the rest. Even the smallest perturbations from the off-diagonal terms have tremendous impact inside of the degenerate space, resulting in multiple determinants with large weights. In real systems, the multi-reference feature in the ground state wavefunction caused by (quasi-)degeneracies is attributed as *static correlations*. This type of correlations clearly cannot be treated correctly with any methods that rely on the assumption that there is a dominant reference determinant in the wavefunction.

In conclusion, strong correlations appear when i) there are remaining strong Coulomb interactions that are not captured by the mean-field solution; ii) there are degeneracies in the low-lying SD space and (small) perturbations within this space. An example for the first case is the system of NiO, which, according to the simple band theory, is a metal, but in reality it is an insulator due to the strong on-site Coulomb repulsion among electrons [20]. The second scenario occurs normally in systems with partially filled d or f shells, such as $3d$ transition metal oxides.

Chapter 4

Deterministic Many-body Theories

In this chapter, we will review a host of many-body theories that aim to include the correlation effects and go beyond the mean-field theories. In particular, we focus on a hierarchy of methods that can be classified as perturbative or diagrammatic methods. In terms of computation of the ground state energy, MP2, CCD/DCD, CCSD/distinguishable cluster singles and doubles (DCSD) and CCSD(T) represent a hierarchy of methods, whose computational costs increase and accuracies improve in roughly the same order. It is worth pointing out that CCSD(T) is the standard in quantum chemistry for predicting chemical reactions in gas phases. We will start with some basics about second quantization and Wick's theorem before the introduction to the many-body theories.

4.1 Second Quantization

The second quantization provides useful tools to incorporate the statistics of fermions and bosons in the representation of the wavefunctions, in the occupation number form as introduced in Eq. (2.13). The most important notations are the creation and annihilation operators, which for fermions satisfy the following anticommutation relations,

$$[a_i^\dagger, a_j]_+ = \delta_{i,j}, \quad [a_i^\dagger, a_j^\dagger]_+ = 0, \quad [a_i, a_j]_+ = 0, \tag{4.1}$$

where the anticommutation relation is defined as $[\hat{A}, \hat{B}]_+ \equiv \hat{A}\hat{B} + \hat{B}\hat{A}$. These relations between the fermionic creation and annihilation operators plant the

antisymmetry naturally into the wavefunction. The effects of applying the creation and annihilation operators on a many-body state are

$$\begin{aligned} a_1^\dagger \left|111000\right\rangle &= 0, \\ a_4^\dagger \left|111000\right\rangle &= -\left|111100\right\rangle, \\ a_1 \left|111000\right\rangle &= \left|011000\right\rangle, \\ a_4 \left|111000\right\rangle &= 0. \end{aligned} \tag{4.2}$$

Using the creation and annihilation operators, we can write the electronic Hamiltonian, Eq. (1.8), as follows

$$\hat{H} = \sum_{pq} \sum_{\sigma} h_{pq} a_{p,\sigma}^\dagger a_{q,\sigma} + \frac{1}{2} \sum_{pqrs} \sum_{\sigma,\sigma'} V_{rs}^{pq} a_{p,\sigma}^\dagger a_{q,\sigma'}^\dagger a_{s,\sigma'} a_{r,\sigma}, \tag{4.3}$$

where p, q, r, s are indices for spatial orbitals, and the one- and two-particle integrals are defined as

$$\begin{aligned} h_{pq} &= \int \mathrm{d}\mathbf{r} \varphi_p^*(\mathbf{r}) \hat{h} \varphi_q(\mathbf{r}), \\ V_{rs}^{pq} &= \int\int \mathrm{d}\mathbf{r}\mathrm{d}\mathbf{r}' \varphi_p^*(\mathbf{r}) \varphi_q^*(\mathbf{r}') \frac{1}{|\mathbf{r} - \mathbf{r}'|} \varphi_r(\mathbf{r}) \varphi_s(\mathbf{r}'), \end{aligned} \tag{4.4}$$

with $\hat{h}$ defined in Eq. (2.2). In practice, the integrals are computed beforehand and stored in computer memory for instant access during the many-body theory simulations.

4.2 Wick's Theorem

The Wick's theorem is an essential tool for handling products of many creation and annihilation operators. Before we introduce the theorem, we need to define the concept of *normal ordering* and *contraction* among operators.

In electronic structure theory, the vacuum state is often chosen to be a reference determinant, such as the HF wavefunction. As such, the creation operators are $a_A^\dagger, a_B^\dagger, a_C^\dagger \ldots$ (creating particles) and $a_I, a_J, a_K \ldots$ (creating holes); the annihilation operators are $a_I^\dagger, a_J^\dagger, a_K^\dagger \ldots$ (destroying holes) and $a_A, a_B, a_C \ldots$ (destroying particles). The meaning of the indices is defined at the end of Sec. 2.1.2 and in this case they refer to spin orbitals. A string of operators are normal-ordered when all creation operators are placed to the left of the annihilation

operators. For example,

$$\{a_I^\dagger a_A^\dagger\} = -a_A^\dagger a_I^\dagger, \quad \{a_A a_I\} = -a_I a_A, \quad \{a_A^\dagger a_I\} = a_A^\dagger a_I, \tag{4.5}$$

where we use $\{\}$ to denote normal-ordered operators and introduce a minus sign when the relative positions between two operators are changed.

A *contraction* is defined as $\hat{A}\hat{B} = \hat{A}\hat{B} - \{\hat{A}\hat{B}\}$. For aforementioned creation and annihilation operators we have

$$\begin{aligned}
\overbrace{a_I^\dagger a_J} &= a_I^\dagger a_J - \{a_I^\dagger a_J\} = a_I^\dagger a_J + a_J a_I^\dagger = \delta_{I,J}, \\
\overbrace{a_B a_A^\dagger} &= a_B a_A^\dagger - \{a_B a_A^\dagger\} = a_B a_A^\dagger + a_A^\dagger a_B = \delta_{A,B}, \\
\overbrace{a_A^\dagger a_I} &= a_A^\dagger a_I - \{a_A^\dagger a_I\} = a_A^\dagger a_I - a_A^\dagger a_I = 0.
\end{aligned} \tag{4.6}$$

The contractions between operators belonging to different spaces, i.e. occupied and unoccupied spaces, are always 0.

Theorem 4.2.1. *A product of creation and annihilation operators $\hat{A}\hat{B}\hat{C}\hat{D}\ldots$ can be expressed as a combination of the normal-ordered product, single contractions between all possible pairs of operators in the normal-ordered product, all possible double contractions in the normal-ordered product, etc. and the fully contracted operator:*

$$\begin{aligned}
\hat{A}\hat{B}\hat{C}\hat{D}\ldots = &\{\hat{A}\hat{B}\hat{C}\hat{D}\ldots\} \\
&+ \sum_{\text{singles}} \{\overbrace{\hat{A}\hat{B}}\hat{C}\hat{D}\ldots\} \\
&+ \sum_{\text{doubles}} \{\overbrace{\hat{A}\hat{B}\hat{C}}\hat{D}\ldots\} \\
&+ \ldots.
\end{aligned} \tag{4.7}$$

The proof of the theorem will be left out in this thesis. Instead we refer to textbooks in advanced quantum mechanics. This theorem will be useful when we treat the three-body operator in the transcorrelated Hamiltonian in Sec. 9.3, as well as when deriving the equations in the following sections.

4.3 G_0W_0 Approximation

The Green's function based G_0W_0 approximation [21] is widely used in solids to obtain accurate band structures (quasi-particle energies). It is normally based on a prior DFT calculation, and it provides corrections due to many-body effects

to the DFT quasiparticle energies. A full introduction to the Green's function based methods and the required *Dyson equation* are beyond the scope of this thesis. Instead, we summarize the main concepts in the G_0W_0 approximation, leaving out the details. A good presentation on this topic can be found in Ref. [22, 23] and many others.

To include the many-body correlation effects, we can add a perturbation term to the KS equations, Eq. (2.23),

$$\left(\hat{h} + V_s(\mathbf{r}) + \int \mathrm{d}\mathbf{r}' \Delta\Sigma(\mathbf{r}, \mathbf{r}'; \epsilon_p)\right) \varphi_p(\mathbf{r}) = \epsilon_p \varphi_p(\mathbf{r}), \tag{4.8}$$

where $\Delta\Sigma(\mathbf{r}, \mathbf{r}'; \epsilon_p) = \Sigma(\mathbf{r}, \mathbf{r}'\epsilon_p) - V_{\mathrm{XC}}(\mathbf{r})\delta(\mathbf{r} - \mathbf{r}')$ is the difference between the self-energy $\Sigma(\mathbf{r}, \mathbf{r}'; \epsilon_p)$ and the XC potential, and ϵ_p, $\varphi_p(\mathbf{r})$ and $V_{\mathrm{XC}}(\mathbf{r})$ are the KS eigenvalues (quasi-particle energies), eigenfunctions and the corresponding XC functional, respectively. In the Green's function formulation, the self-energy contains the information of the correlation effects. So according to perturbation theory, the G_0W_0 quasiparticle energies can be written as

$$\epsilon_p^{G_0W_0} = \epsilon_p + \langle \varphi_p(\mathbf{r}) \,|\, Re[\Delta\Sigma(\mathbf{r}, \mathbf{r}'; \epsilon_p)] \,|\, \varphi_p(\mathbf{r}') \rangle \,. \tag{4.9}$$

In principle, the self-energy is determined by the many-electron Green's function through the *Dyson equation*. In the G_0W_0 approximation, the Green's function is approximated on the level of the KS solutions,

$$G_0(\mathbf{r}, \mathbf{r}'; w) = \sum_p \frac{\varphi_p^*(\mathbf{r}')\varphi_p(\mathbf{r})}{w - \epsilon_p \pm \mathrm{i}\eta}, \tag{4.10}$$

where w is the frequency (energy) and η is a small positive number. With G_0, we can write the self-energy as

$$\Sigma(\mathbf{r}, \mathbf{r}'; w) = \frac{\mathrm{i}}{2\pi} \int \mathrm{d}w' G_0(\mathbf{r}, \mathbf{r}'; w + w') W_0(\mathbf{r}, \mathbf{r}'; w'), \tag{4.11}$$

where the screened Coulomb potential, $W_0(\mathbf{r}, \mathbf{r}'; w')$, is calculated by the random phase approximation (RPA) [24, 25], which will be briefly addressed in Sec. 4.5.1 along with CCD.

It is shown that G_0W_0 provides very good predictions on the band gaps of a range of solid materials [26, 27, 28]. One comment is that the G_0W_0's prediction has a dependence on the XC functional used in DFT. The G_0W_0 method will be used in the study of the band structures of the optimised structure of solid hydrogen in chapter 11.

4.4 Second Order Møller-Plesset Perturbation Theory

In some cases, the HF wavefunction lies close to the true many-electron ground state wavefunction. Hence, a simple perturbative approach can provide an accurate solution to the problem. The Møller-Plesset perturbation theory assumes the following partition of the electronic Hamiltonian

$$\hat{H} = \hat{H}_0 + \lambda \hat{V}, \tag{4.12}$$

where $\hat{H}_0 = \sum_i \left(\hat{h}_i + \hat{v}_i^{\mathrm{HF}}\right)$ is the mean-field HF Hamiltonian, $\hat{V} = \hat{H} - \hat{H}_0 = \frac{1}{2}\sum_{i\neq j}\frac{1}{|\mathbf{r}_i - \mathbf{r}_j|} - \sum_i \hat{v}^{\mathrm{HF}}(\mathbf{r}_i)$ is the remaining interaction operator (perturbation) and λ is a parameter used to track the order of the perturbation. In the meantime, we assume that the true ground state energy and the ground state wavefunction can be expressed in terms of increasing orders of corrections

$$\begin{aligned} E_0 &= E^{(0)} + \lambda E^{(1)} + \lambda^2 E^{(2)} + \dots \\ |\Psi_0\rangle &= \left|\Phi^{(0)}\right\rangle + \lambda \left|\Phi^{(1)}\right\rangle + \lambda^2 \left|\Phi^{(2)}\right\rangle + \dots, \end{aligned} \tag{4.13}$$

with $\hat{H}_0 \left|\Phi^{(0)}\right\rangle = E^{(0)} \left|\Phi^{(0)}\right\rangle$ and the intermediate normalisation $\left\langle \Phi^{(0)} \middle| \Phi^{(0)} \right\rangle = \left\langle \Phi^{(0)} \middle| \Psi_0 \right\rangle = 1$. After we plug Eq. (4.13) and Eq. (4.12) into the time-independent Schrödinger equation, we have

$$\begin{aligned} &(\hat{H}_0 + \lambda\hat{V})\left(\left|\Phi^{(0)}\right\rangle + \lambda\left|\Phi^{(1)}\right\rangle + \lambda^2\left|\Phi^{(2)}\right\rangle + \dots\right) = \\ &\left(E^{(0)} + \lambda E^{(1)} + \lambda^2 E^{(2)} + \dots\right)\left(\left|\Phi^{(0)}\right\rangle + \lambda\left|\Phi^{(1)}\right\rangle + \lambda^2\left|\Phi^{(2)}\right\rangle + \dots\right), \end{aligned} \tag{4.14}$$

and after expansion and regrouping terms involving the first order in λ, we find the following first order relation

$$\lambda\hat{H}_0\left|\Phi^{(1)}\right\rangle + \lambda\hat{V}\left|\Phi^{(0)}\right\rangle = \lambda E^{(0)}\left|\Phi^{(1)}\right\rangle + \lambda E^{(1)}\left|\Phi^{(0)}\right\rangle. \tag{4.15}$$

After multiplying with $\left\langle\Phi^{(0)}\right|$ from the left on both sides of the above equation and using the fact that the $\hat{H}_0$ is Hermitian, i.e. $\left\langle\Phi^{(0)}\right|\hat{H}_0 = \left\langle\Phi^{(0)}\right| E^{(0)}$, we cancel the first terms on both sides of the equation and obtain

$$E^{(1)} = \left\langle \Phi^{(0)} \middle| \hat{V} \middle| \Phi^{(0)} \right\rangle = \left\langle D_{\mathrm{HF}} \middle| \hat{H} - \hat{H}_0 \middle| D_{\mathrm{HF}} \right\rangle = E_{\mathrm{HF}} - \sum_I^N \epsilon_I, \tag{4.16}$$

where we have used the relation, $\left|\Phi^{(0)}\right\rangle = |D_{\mathrm{HF}}\rangle$, $\hat{H}_0 |D_{\mathrm{HF}}\rangle = \sum_{I=1}^N \epsilon_I |D_{\mathrm{HF}}\rangle$ and $E_{\mathrm{HF}} = \left\langle D_{\mathrm{HF}} \middle| \hat{H} \middle| D_{\mathrm{HF}} \right\rangle$.

To obtain the first-order correction to the wavefunction, $\left|\Phi^{(1)}\right\rangle$, we expand it in terms of the eigenstates (Slater determinants) of $\hat{H}_0$,

$$\left|\Phi^{(1)}\right\rangle = \sum_k T_k \left|\Phi_k^{(0)}\right\rangle = \sum_k T_k \left|D_k\right\rangle . \tag{4.17}$$

After rearranging the terms in Eq. (4.15), we find

$$\left(\hat{H}_0 - E^{(0)}\right)\left|\Phi^{(1)}\right\rangle = (E^{(1)} - \hat{V})\left|\Phi^{(0)}\right\rangle . \tag{4.18}$$

According to the *Brillouin theorem* [29], the first order correction to the wavefunction can only contain nonzero components from doubly excited Slater determinants. Thus plugging Eq. (4.17) containing only the doubly excited Slater determinants $\left|\Phi^{(1)}\right\rangle = \sum_{I>J,A>B} T_{IJ}^{AB}\left|D_{IJ}^{AB}\right\rangle$ into the above equation, we can determine the coefficients as

$$T_{IJ}^{AB} = -\frac{\left\langle D_{IJ}^{AB}\middle|\hat{V}\middle|D_{\mathrm{HF}}\right\rangle}{E_{IJ}^{AB} - E^{(0)}} = \frac{\left\langle D_{IJ}^{AB}\middle|\hat{V}\middle|D_{\mathrm{HF}}\right\rangle}{\epsilon_I + \epsilon_J - \epsilon_A - \epsilon_B}, \tag{4.19}$$

where we have used the orthogonality between different Slater determinants and $\hat{H}_0\left|D_{IJ}^{AB}\right\rangle = E_{IJ}^{AB}\left|D_{IJ}^{AB}\right\rangle = (\sum_{K=1}^{N}\epsilon_K - \epsilon_I - \epsilon_J + \epsilon_A + \epsilon_B)\left|D_{IJ}^{AB}\right\rangle$.

In a similar fashion, by comparing the terms containing λ^2 on both sides of Eq. (4.14) and using the expression Eq. (4.19), we get the expression for the second order energy

$$\begin{aligned} E_{\mathrm{MP2}}^{\mathrm{c}} \equiv E^{(2)} &= \left\langle \Phi^{(0)}\middle|\hat{V}\middle|\Phi^{(1)}\right\rangle \\ &= \sum_{I>J,A>B} T_{IJ}^{AB}\left\langle D_{\mathrm{HF}}\middle|\hat{V}\middle|D_{IJ}^{AB}\right\rangle \\ &= \sum_{I>J,A>B} \frac{\left\langle D_{IJ}^{AB}\middle|\hat{V}\middle|D_{\mathrm{HF}}\right\rangle\left\langle D_{\mathrm{HF}}\middle|\hat{V}\middle|D_{IJ}^{AB}\right\rangle}{\epsilon_I + \epsilon_J - \epsilon_A - \epsilon_B} \\ &= \sum_{I>J,A>B} \frac{|V_{IJ}^{AB}|^2}{\epsilon_I + \epsilon_J - \epsilon_A - \epsilon_B}. \end{aligned} \tag{4.20}$$

For a closed-shell system [16], we have

$$E_{\mathrm{MP2}}^{\mathrm{c}} = \sum_{ijab} \frac{(2V_{ij}^{ab} - V_{ji}^{ab})V_{ab}^{ij}}{\epsilon_i + \epsilon_j - \epsilon_a - \epsilon_b}. \tag{4.21}$$

From the energy expression of MP2, it is apparent that it will yield infinite correlation energy when there are degeneracies in the orbital energies close to the

Fermi surface, such as in metals. However for systems with large gaps, MP2 normally provides good results in systems with weak dynamical correlations. Furthermore, due to its relatively low computational scaling with system size ($\mathcal{O}(N^5)$), MP2 also serves as a stepping stone for more advanced, yet more expensive, theories, as we shall discuss in the next section on the MP2 natural orbitals.

4.4.1 MP2 Natural Orbitals

In Sec. 3.1, we illustrate that in order to describe the sharp cusp in the wavefunction as two electrons collide, we need a large number of basis functions (or equivalently, virtual orbitals). And in Ref. [19], it was shown that MP2 is able to recover this behavior at CBS limit. So naturally one wonders if we can get something out of MP2, so that we can accelerate the convergence of some more expensive methods, such as CCSD, with respect to the basis set. One such method is to incorporate the short-range correlation effects inside the virtual orbitals, calculated on the MP2 level, for higher level theories.

To this end, the virtual-virtual block of the one-electron density matrix of MP2 is constructed for closed-shell systems as [30]

$$\Gamma^{(2)}_{ab} = \sum_{cij} \frac{2V^{cb}_{ij}V^{ij}_{ca} - V^{cb}_{ji}V^{ij}_{ca}}{\Delta^{cb}_{ij}\Delta^{ca}_{ij}}, \tag{4.22}$$

where $\Delta^{cb}_{ij} = \epsilon_i + \epsilon_j - \epsilon_c - \epsilon_b$. Or in practice, the approximate version [31],

$$\Gamma^{(2)}_{ab} \approx \sum_{ci} \frac{V^{cb}_{ii}V^{ii}_{ca}}{\Delta^{cb}_{ii}\Delta^{ca}_{ii}}, \tag{4.23}$$

is used which is less computationally expensive yet almost as effective as the original one. We then diagonalise the MP2 one-electron density matrix, obtaining the eigenvalues and eigenvectors, which correspond to the occupation number and MP2 natural orbitals, respectively. The larger the occupation number is, the more important the corresponding natural orbital is. In systems with finite gaps, the occupation number normally decays very fast with the increase of the orbital index. Thus employing only a small fraction of the MP2 (virtual) natural orbitals, calculated at a very large basis set, is enough to recover the main feature of the cusp condition. Hence the computational demand to obtain the correlation energy at a higher level of theory is significantly reduced.

4.5 Coupled Cluster Methods

In the CC [32, 33] ansatz, we let the many-electron ground state wavefunction be

$$|\Psi_{\mathrm{CC}}\rangle = e^{\hat{T}} |\Phi_0\rangle , \tag{4.24}$$

where $|\Phi_0\rangle$ is a reference wavefunction, e.g. HF determinant $|\Phi_0\rangle \equiv |D_{\mathrm{HF}}\rangle$, and $\hat{T}$ is the cluster operator which contains singles, doubles, etc. excitation operators

$$\begin{aligned}
\hat{T}_1 =& \sum_{ai} T_I^A a_A^\dagger a_I, \\
\hat{T}_2 =& \frac{1}{2!} \sum_{ABIJ} T_{IJ}^{AB} a_A^\dagger a_B^\dagger a_J a_I, \\
\hat{T}_3 =& \frac{1}{3!} \sum_{ABCIJK} T_{IJK}^{ABC} a_A^\dagger a_B^\dagger a_C^\dagger a_K a_J a_I, \\
& \vdots
\end{aligned} \tag{4.25}$$

The unknown amplitudes $T_I^A, T_{IJ}^{AB} \ldots$ are determined by solving the following amplitudes equations

$$\left\langle \Phi_{IJ\ldots}^{AB\ldots} \middle| \bar{H} \middle| \Phi_0 \right\rangle = 0, \quad \bar{H} = e^{-\hat{T}} \hat{H} e^{\hat{T}}. \tag{4.26}$$

The above amplitudes equations are nonlinear due to the exponential operator and are normally solved iteratively and self-consistently. We will come to the details of the amplitudes equations and the methods to solve them later.

The similarity transformed Hamiltonian $\bar{H}$ can be expanded by the Hausdorff expansion,

$$\bar{H} = \hat{H} + [\hat{H}, \hat{T}] + \frac{1}{2!}[[\hat{H}, \hat{T}], \hat{T}] + \frac{1}{3!}[[[\hat{H}, \hat{T}], \hat{T}], \hat{T}] + \frac{1}{4!}[[[[\hat{H}, \hat{T}], \hat{T}], \hat{T}], \hat{T}]. \tag{4.27}$$

The termination of this expansion is exact, due to the fact that the electronic Hamiltonian contains operators up to two-body only. The CC correlation energy is obtained as

$$E_{\mathrm{CC}}^{\mathrm{c}} = \left\langle \Phi_0 \middle| \bar{H} \middle| \Phi_0 \right\rangle . \tag{4.28}$$

For an N-electron system, when up to the N-fold excitation cluster operators are included, the CC ansatz is equivalent to the FCI wavefunction, with the

equivalence established as below

$$\begin{aligned}\hat{C}_1 &= \hat{T}_1,\\ \hat{C}_2 &= \hat{T}_2 + \frac{1}{2}\hat{T}_1^2,\\ \hat{C}_3 &= \hat{T}_3 + \hat{T}_1\hat{T}_2 + \frac{1}{3!}T_1^3,\\ &\vdots,\end{aligned} \tag{4.29}$$

where we recast the FCI wavefunction, Eq. (3.4), in terms of the excitation operators acting on the reference determinant $|\Psi_{\mathrm{FCI}}\rangle = (1 + \sum_{n=1}^{N} \hat{C}_n)\,|\Phi_0\rangle$, in which $\hat{C}_n$ generates all possible n-fold excitations from $|\Phi_0\rangle$, e.g. $\hat{C}_2 = \sum_{A>B,I>J} C_{IJ}^{AB} a_A^\dagger a_B^\dagger a_J a_I$.

Comparatively speaking, the CC ansatz has the advantage that even when only the lowest cluster operators are used, it contains quadruples, hextuples and higher order excitations generated by the products of the lower excitations. This fact makes the CC wavefunctions size-consistent and in practice outperform the configuration interaction (CI) wavefunctions truncated at the same level, whilst having the same computational scaling as the latter. For example, when both are truncated at the singles and doubles level, we have configuration interaction singles and doubles (CISD) and CCSD for the CI and CC ansatz respectively. The key difference between the two is that the former has only singly and doubly excited Slater determinants in the wavefunction besides the reference, while the latter has the same plus some disconnected triples, quadruples, etc.

4.5.1 Coupled/Distinguishable Cluster Doubles

In this section, we introduce the spin-restricted CCD and DCD theories. The CCD has been used in model systems such as the uniform electron gas (UEG), where the momentum conservation excludes the singles excitations. Along with the CCD approximation, we will also introduce its distinguishable variant (DCD) [34, 35], which is based on a modification of the CCD amplitude equations by neglecting inter-cluster exchange diagrams and ensuring the particle-hole symmetry and exactness for two electrons. Alternatively, DCD can be derived from screened Coulomb considerations [36]. We start with the canonical CCD and later highlight the differences between CCD and DCD.

In CCD, the full cluster operator is approximated by the doubles excitations only. For a closed-shell system, it is

$$\hat{T} \approx \hat{T}_2 = \frac{1}{2} \sum_{ijab} T_{ij}^{ab} \sum_{\sigma\sigma'} a_{a,\sigma}^\dagger a_{b,\sigma'}^\dagger a_{j,\sigma'} a_{i,\sigma}, \tag{4.30}$$

where T_{ab}^{ij} are the doubles amplitudes. Following convention, we use $i, j, k \ldots$ and $a, b, c \ldots$ to represent occupied and unoccupied spatial orbitals in the reference determinant, respectively.

The T_2 amplitudes are obtained by solving the projective doubles amplitude equations,

$$\left\langle \Phi_{ij}^{ab} \left| e^{-\hat{T}_2} \hat{H} e^{\hat{T}_2} \right| \Phi_0 \right\rangle = 0, \tag{4.31}$$

where Φ_{ij}^{ab} are doubly substituted determinants. To be specific, a functional form of the residual, which unifies CCD and DCD for closed-shell systems, can be written as

$$\begin{aligned} R_{ij}^{ab} =& V_{ij}^{ab} + V_{cd}^{ab} T_{ij}^{cd} + I_{ij}^{kl} T_{kl}^{ab} + X_{cj}^{al} T_{il}^{cb} + \tilde{T}_{ik}^{ac} V_{cd}^{kl} \tilde{T}_{lj}^{db} \\ &+ \hat{\mathcal{P}}(ia;jb) \left[x_c^a T_{ij}^{cb} - x_i^k T_{kj}^{ab} + \chi_{ci}^{al} (T_{lj}^{bc} - T_{lj}^{cb}) \right. \\ &\left. - V_{ic}^{ka} T_{kj}^{cb} - V_{ic}^{kb} T_{kj}^{ac} + \tilde{T}_{ik}^{ac} V_{cj}^{kb} \right], \end{aligned} \tag{4.32}$$

where the Einstein summation rules are used. We define the permutation operator $\hat{\mathcal{P}}(ia;jb) T_{ij}^{ab} \equiv T_{ij}^{ab} + T_{ji}^{ba}$ and the following intermediates,

$$I_{ij}^{kl} = \begin{cases} V_{ij}^{kl} + V_{cd}^{kl} T_{ij}^{cd}, & \text{CCD} \\ V_{ij}^{kl}, & \text{DCD} \end{cases} \tag{4.33}$$

$$X_{cj}^{al} = \begin{cases} V_{cd}^{kl} T_{kj}^{ad}, & \text{CCD} \\ 0, & \text{DCD} \end{cases} \tag{4.34}$$

$$x_c^a = \begin{cases} f_c^a - \tilde{T}_{kl}^{ad} V_{dc}^{lk}, & \text{CCD} \\ f_c^a - \frac{1}{2} \tilde{T}_{kl}^{ad} V_{dc}^{lk}, & \text{DCD} \end{cases} \tag{4.35}$$

$$x_i^k = \begin{cases} f_i^k + \tilde{T}_{il}^{cd} V_{dc}^{lk}, & \text{CCD} \\ f_i^k + \frac{1}{2} \tilde{T}_{il}^{cd} V_{dc}^{lk}, & \text{DCD} \end{cases} \tag{4.36}$$

$$\chi_{ci}^{al} = \begin{cases} V_{cd}^{kl} T_{ki}^{da}, & \text{CCD} \\ 0, & \text{DCD} \end{cases} \tag{4.37}$$

$$\tilde{T}_{ij}^{ab} = 2T_{ij}^{ab} - T_{ij}^{ba}. \tag{4.38}$$

We note that when the canonical HF orbitals are used, the Fock matrix f_q^p is

diagonal, with the diagonal elements being the orbital energies ϵ_p. A straightforward way to update the T_2 amplitudes at iteration $n+1$ will be

$$\Delta T_{ij}^{ab} = \frac{R_{ij}^{ab}}{\epsilon_i + \epsilon_j - \epsilon_a - \epsilon_b}, \tag{4.39}$$

$$T_{ij}^{ab}(n+1) = T_{ij}^{ab}(n) + \Delta T_{ij}^{ab}. \tag{4.40}$$

Of course, more advanced iterative schemes can be used, e.g. DIIS [37, 38], to accelerate convergence rate.

Using the converged T_2 amplitudes, the correlation energy is expressed as

$$E_{\mathrm{CCD/DCD}}^{\mathrm{c}} = T_{ij}^{ab}(2V_{ab}^{ij} - V_{ba}^{ij}), \tag{4.41}$$

and the total energy is

$$E = E_{\mathrm{HF}} + E_{\mathrm{CCD/DCD}}^{\mathrm{c}}. \tag{4.42}$$

We comment briefly on the relation between CCD and the popular RPA method in the condensed matter community. In Ref. [39], the equivalence between RPA and the ring-CCD was established. The ring-CCD solves the amplitudes equations that have only the ring-type contractions. Its closed-shell amplitudes equation can be written as [34]

$$R_{ij}^{ab} = V_{ij}^{ab} + 4T_{ik}^{ac}V_{cd}^{kl}T_{lj}^{db} + \hat{\mathcal{P}}(ia;jb)\left[f_d^a T_{ij}^{bd} - f_i^k T_{kj}^{ab} + 2T_{ik}^{ac}V_{cj}^{kb}\right]. \tag{4.43}$$

The iterative solutions to these equations scale as $\mathcal{O}(N^6)$, but with some advanced techniques it can be reduced to a lower polynomial scaling with the system size N [39]. The RPA can also be formulated in terms of a resummation of the ring diagrams to the infinite order in the Dyson equation [25, 22], yielding screened Coulomb interaction. This screening effect is crucial in metals where the electrons are free to move around, as studied in Ref. [25] at the high density limit of 3D UEG.

4.5.2 Coupled/Distinguishable Cluster Singles and Doubles

Adding the singles cluster operator into the CCD ansatz, we obtain the CCSD ansatz

$$|\Psi_{\mathrm{CCSD}}\rangle = e^{\hat{T}_1+\hat{T}_2}|\Phi_0\rangle, \tag{4.44}$$

which is necessary when treating real solids. The exponential singles cluster operator generates the singly-excited Slater determinants in the ansatz and

their higher order products, playing the role of orbital rotations according to the *Thouless Theorem* [40], which states

Theorem 4.5.1. *Any N-particle Slater determinant $|D\rangle$ which is not orthogonal to $|D_0\rangle$ can be written in the form*

$$\begin{aligned} |D\rangle &= \left[\prod_{i=1}^{N}\prod_{m=N+1}^{\infty}(1+C_{mi}a_m^\dagger a_i)\right]|D_0\rangle \\ &= \exp\left(\sum_{i=1}^{N}\sum_{m=N+1}^{\infty}C_{mi}a_m^\dagger a_i\right)|D_0\rangle\,, \end{aligned} \tag{4.45}$$

where N is the number of electrons and the coefficients C_{mi} connect $|D\rangle$ and $|D_0\rangle$ uniquely and $|D_0\rangle = \prod_{i=1}^{N} a_i^\dagger |0\rangle$, with $|0\rangle$ being the vacuum state.

In principle, at a large enough basis set, the Thouless theorem ensures that the CCSD/DCSD solution will not be so sensitive to the choice of the orbitals in the reference determinant in the absence of degeneracies in the system, as the exponential singles cluster operator effectively rotates the orbitals into suitable ones. The Thouless theorem also enables the formulation of the HF theory in second quantization. For more details and the proof of this theorem, we refer to Ref. [40].

Here we present the spin-restricted CCSD/DCSD equations for closed-shell systems in a similar fashion as in the previous section. We follow Ref. [34] for CCSD and Ref. [36] for DCSD using the dressed integrals and Fock matrix. With a similarity transformation using the singles cluster operator $\hat{T}_1 = \sum_{ai} T_i^a(a_{a\sigma}^\dagger a_{i\sigma} + a_{a\bar{\sigma}}^\dagger a_{i\bar{\sigma}})$ on the Hamiltonian, with σ and $\bar{\sigma}$ referring to spin up and down, respectively,

$$\tilde{H} = e^{-\hat{T}_1}\hat{H}e^{\hat{T}_1}, \tag{4.46}$$

we get the dressed integrals and Fock matrix (to be introduced soon), with which the CCSD/DCSD doubles amplitude equations can be cast in the same form as the CCD/DCD doubles amplitude equations.

In periodic solids, normally the Coulomb integrals are density-fitted by an auxiliary plane wave basis functions,

$$V_{rs}^{pq} = \Gamma_r^{p\mathbf{G}}\Gamma_{s\mathbf{G}}^{q}, \tag{4.47}$$

where $\mathbf{G}$ is the auxiliary plane wave index. For the dressed Coulomb integrals as a result of Eq. (4.46), we modify the three-index tensor $\Gamma^p_{r\mathbf{G}}$ as follows

$$\begin{aligned}
\tilde{\Gamma}^i_{j\mathbf{G}} &= \Gamma^i_{j\mathbf{G}} + \Gamma^i_{b\mathbf{G}} T^b_j, \\
\tilde{\Gamma}^a_{i\mathbf{G}} &= \Gamma^a_{i\mathbf{G}} - \Gamma^j_{i\mathbf{G}} T^a_j + \Gamma^a_{b\mathbf{G}} T^b_i - \Gamma^j_{b\mathbf{G}} T^a_j T^b_i, \\
\tilde{\Gamma}^i_{a\mathbf{G}} &= \Gamma^i_{a\mathbf{G}}, \\
\tilde{\Gamma}^a_{b\mathbf{G}} &= \Gamma^a_{b\mathbf{G}} - \Gamma^j_{b\mathbf{G}} T^a_j.
\end{aligned} \tag{4.48}$$

So the resulting dressed density-fitted Coulomb integrals, denoted by a tilde on top, are

$$\begin{aligned}
\tilde{V}^{ij}_{kl} &= \tilde{\Gamma}^{i\mathbf{G}}_k \tilde{\Gamma}^j_{l\mathbf{G}}, \\
\tilde{V}^{ab}_{cd} &= \tilde{\Gamma}^{a\mathbf{G}}_c \tilde{\Gamma}^b_{d\mathbf{G}}, \\
\tilde{V}^{ia}_{jb} &= \tilde{\Gamma}^{i\mathbf{G}}_j \tilde{\Gamma}^a_{b\mathbf{G}}, \\
\tilde{V}^{ij}_{ab} &= \tilde{\Gamma}^{i\mathbf{G}}_a \tilde{\Gamma}^j_{b\mathbf{G}}.
\end{aligned} \tag{4.49}$$

The dressed Fock matrix blocks are

$$\begin{aligned}
\tilde{f}^a_i &= f^a_i - f^j_i T^a_j + f^a_b T^b_i - f^j_b T^b_i T^a_j \\
&\quad + 2T^b_j (V^{ja}_{bi} - V^{jk}_{bi} T^a_k + V^{ja}_{bc} T^c_i - V^{jk}_{bc} T^c_i T^a_k) \\
&\quad - T^b_j (V^{ja}_{ib} - V^{jk}_{ib} T^a_k + V^{ja}_{cb} T^c_i - V^{jk}_{cb} T^c_i T^a_k), \\
\tilde{f}^i_a &= f^i_a + 2T^b_j V^{ja}_{bi} - T^b_j V^{ji}_{ab}, \\
\tilde{f}^a_b &= f^a_b + 2T^c_k V^{ka}_{cb} - T^c_k V^{ka}_{bc} \\
&\quad - f^k_b T^a_k - 2T^c_k V^{kl}_{cb} T^a_l + T^c_k V^{kl}_{bc} T^a_l, \\
\tilde{f}^i_j &= f^i_j + 2T^c_k V^{ki}_{cj} - T^c_k V^{ki}_{jc} \\
&\quad + f^i_b T^b_j + 2T^c_k V^{ki}_{cb} T^b_j - T^c_k V^{ki}_{bc} T^b_j.
\end{aligned} \tag{4.50}$$

We point out that the dressed Fock matrix is no longer Hermitian.

Finally, from the singles and doubles amplitude equations

$$\begin{aligned}
\left\langle \Phi^a_i \middle| e^{-\hat{T}_2} \tilde{H} e^{\hat{T}_2} \middle| \Phi_0 \right\rangle = 0, \\
\left\langle \Phi^{ab}_{ij} \middle| e^{-\hat{T}_2} \tilde{H} e^{\hat{T}_2} \middle| \Phi_0 \right\rangle = 0,
\end{aligned} \tag{4.51}$$

we obtain the singles and doubles residuals respectively as

$$R^a_i = \tilde{f}^a_i + \tilde{f}^j_b \tilde{T}^{ab}_{ij} + \tilde{\Gamma}^{a\mathbf{G}}_b \tilde{T}^{bc}_{ij} \Gamma^j_{c\mathbf{G}} - \tilde{\Gamma}^{j\mathbf{G}}_i \tilde{T}^{ab}_{jk} \Gamma^k_{b\mathbf{G}}, \tag{4.52}$$

and

$$\begin{aligned} R_{ij}^{ab} =& \tilde{I}_{ij}^{kl} T_{kl}^{ab} + \tilde{V}_{cd}^{ab} T_{ij}^{cd} + \tilde{Y}_i^{a\mathbf{G}} \tilde{Y}_{j\mathbf{G}}^{b} + X_{cj}^{al} T_{il}^{cb} + \\ &+ \hat{\mathcal{P}}(ia;jb) \left[\tilde{x}_c^a T_{ij}^{cb} - \tilde{x}_i^k T_{kj}^{ab} + \chi_{ci}^{al} (T_{lj}^{bc} - T_{lj}^{cb}) \right. \\ &\left. - \tilde{V}_{ic}^{ka} T_{kj}^{cb} - \tilde{V}_{ic}^{kb} T_{kj}^{ac} \right], \end{aligned} \tag{4.53}$$

where the following intermediates are used:

$$\tilde{Y}_{i\mathbf{G}}^{a} = \tilde{T}_{ij}^{ab} \Gamma_{b\mathbf{G}}^{j} + \tilde{\Gamma}_{i\mathbf{G}}^{a}, \tag{4.54}$$

$$\tilde{I}_{ij}^{kl} = \begin{cases} \tilde{V}_{ij}^{kl} + V_{cd}^{kl} T_{ij}^{cd}, & \text{CC} \\ \tilde{V}_{ij}^{kl}, & \text{DC} \end{cases} \tag{4.55}$$

$$X_{cj}^{al} = \begin{cases} V_{cd}^{kl} T_{kj}^{ad}, & \text{CC} \\ 0, & \text{DC} \end{cases} \tag{4.56}$$

$$\tilde{x}_c^a = \begin{cases} \tilde{f}_c^a - \tilde{T}_{kl}^{ad} V_{dc}^{lk}, & \text{CC} \\ \tilde{f}_c^a - \frac{1}{2} \tilde{T}_{kl}^{ad} V_{dc}^{lk}, & \text{DC} \end{cases} \tag{4.57}$$

$$\tilde{x}_i^k = \begin{cases} \tilde{f}_i^k + \tilde{T}_{il}^{cd} V_{dc}^{lk}, & \text{CC} \\ \tilde{f}_i^k + \frac{1}{2} \tilde{T}_{il}^{cd} V_{dc}^{lk}, & \text{DC} \end{cases} \tag{4.58}$$

$$\chi_{ci}^{al} = \begin{cases} V_{cd}^{kl} T_{ki}^{da}, & \text{CC} \\ 0. & \text{DC} \end{cases} \tag{4.59}$$

The amplitude equations are solved iteratively, in the same way as explained in the previous section. When the undressed integrals and Fock matrix are used, solving Eq. (4.53) alone will yield CCD/DCD doubles amplitudes. The CCSD/DCSD correlation energy is

$$E_{\text{CCSD/DCSD}}^{\text{c}} = (T_{ij}^{ab} + T_i^a T_j^b)(2V_{ab}^{ij} - V_{ba}^{ij}). \tag{4.60}$$

4.5.3 Coupled Cluster Singles, Doubles and Perturbative Triples

In some cases, CCSD/DCSD does not provide satisfactory accurate results and the triple excitations are needed. However, the triples amplitude tensor has six indices. Storing this tensor alone requires a considerable amount of memory space, let alone solving the amplitude equations iteratively involving it. To circumvent the iterative solution to the triples amplitudes, a one-shot perturbative estimate is often used to provide more information on top of a CCSD solution. This method is termed CCSD(T) and was first introduced by Raghavachari

et al. in 1989 [41]. In the CCSD(T) method, the full amplitudes are approximated by $\hat{T} = \hat{T}_1 + \hat{T}_2 + \hat{T}_3$, where the T_1 and T_2 amplitudes are determined from a CCSD solution and the triples amplitudes are determined perturbatively using the CCSD amplitudes

$$T_{ijk}^{abc} = \frac{\left\langle \Phi_{ijk}^{abc} \middle| \left[\hat{V}, \hat{T}_2\right] \middle| \Phi_0 \right\rangle}{\epsilon_i + \epsilon_j + \epsilon_k - \epsilon_a - \epsilon_b - \epsilon_c}, \tag{4.61}$$

and the energy correction is [42]

$$\Delta E_{(\mathrm{T})} = T_i^a \left\langle \Phi_i^a \middle| \left[\hat{H}, \hat{T}_3\right] \middle| \Phi_0 \right\rangle + \frac{1}{2} T_{ij}^{ab} \left\langle \Phi_{ij}^{ab} \middle| \left[\hat{H}, \hat{T}_3\right] \middle| \Phi_0 \right\rangle, \tag{4.62}$$

which is added to the $E_{\mathrm{CCSD}}^{\mathrm{c}}$, yielding

$$E_{\mathrm{CCSD(T)}}^{\mathrm{c}} = E_{\mathrm{CCSD}}^{\mathrm{c}} + \Delta E_{(\mathrm{T})}. \tag{4.63}$$

Although CCSD(T) is very successful in quantum chemistry, it fails to obtain finite correlation energies for metallic solids in the TDL, similar to MP2 [43]. Also due to its steep $\mathcal{O}(N^7)$ scaling with system size, the application of this method has been limited to very small supercells. Its results are mostly used as benchmarks for lower level theories. Substantial theoretical improvements are needed in order for the routine use of this method. For example, both the basis set convergence and finite size convergence should be addressed.

Chapter 5

Quantum Monte Carlo Methods

In this chapter, another important category of theories–QMC methods–will be introduced. QMC methods take advantage of stochastic processes to reduce the curse of dimensionality that plagues severely some of the deterministic methods. Within the scope of this thesis, we review only two variants of QMC, namely FCIQMC and DMC. Both methods rely on the idea of evolution in imaginary time of some initial guess of the true many-electron wavefunction, which at the infinite time limit will project out the higher energy eigenstates while leaving only the ground state component. The imaginary-time-dependent Schrödinger equation is

$$-\frac{\mathrm{d}}{\mathrm{d}\tau}\Psi(\tau) = \hat{H}\Psi(\tau), \tag{5.1}$$

where $\tau = it$ is the imaginary time and $\Psi(\tau)$ is a general wavefunction. Let Φ_0 be an initial guess, it can then be expanded in terms of the eigenstates of the many-electron Hamiltonian,

$$|\Phi_0\rangle = \sum_i C_i \,|\Psi_i\rangle\,, \tag{5.2}$$

which has non-vanishing overlap with the true many-electron ground state wavefunction, i.e. $C_0 = \langle\Phi_0 \,|\, \Psi_0\rangle \neq 0$. The true ground state can then be obtained by applying the evolution operator in imaginary time with a shift subtracted from the diagonal, $e^{-\tau(\hat{H}-S)}$, to the initial guess

$$\begin{aligned} |\Psi_0\rangle = \lim_{\tau\to\infty} e^{-\tau(\hat{H}-S)}\,|\Phi_0\rangle &= \lim_{\tau\to\infty} e^{-\tau(\hat{H}-S)} \sum_i C_i\,|\Psi_i\rangle \\ &= \lim_{\tau\to\infty} \sum_i C_i e^{-\tau(E_i-S)}\,|\Psi_i\rangle\,, \end{aligned} \tag{5.3}$$

which at the infinite time limit and with a value of S chosen to be close to E_0 will leave all high energy states decay exponentially fast to 0, leaving only the ground state component.

One of the main differences between FCIQMC and DMC lies in that the former is formulated in the discrete configurational space, e.g. Slater determinant space, and the latter is in the real continuum space. This difference has many important implications on the two variants of QMC which we will address in the following sections.

5.1 Diffusion Monte Carlo

The similarity between the classical diffusion equation and the imaginary-time Schrödinger equation in real position space was first pointed out by Fermi [44], who proposed that a random walker process can be found to solve the Schrödinger equation. Metropolis and Ulam [45] followed his idea and started the earliest developments of quantum Monte Carlo methods. In real space, we can split the electronic Hamiltonian, Eq. (1.8), into two parts $\hat{H} = -\sum_i^N \frac{1}{2}\nabla_i^2 + \hat{V}$, where the potential operator includes the electron-nucleus, electron-electron potentials (as pointed earlier, we can always add the nucleus-nucleus potential posteriorly). The imaginary-time Schrödinger equation for an arbitrary many-electron wavefunction $\Psi = \Psi(\{\mathbf{r}\}, \tau)$ is

$$-\frac{\partial \Psi}{\partial \tau} = -\sum_i^N \frac{1}{2}\nabla_i^2 \Psi + \hat{V}\Psi. \tag{5.4}$$

Without the potential term, this equation is exactly the same as the classical diffusion equation (in 3N dimensions). DMC employs an ensemble of weighted random walkers, each of which represents a configuration, $\{\mathbf{r}\}$, of the positions of the N electrons. We follow the derivations in Ref. [46] here. The formal solution to this equation is obtained by constructing the Green's function using the exponential operator introduced,

$$\begin{aligned} G(\{\mathbf{r}\} \leftarrow \{\mathbf{r}\}', \delta\tau) &= \left\langle \{\mathbf{r}\} \left| e^{-\delta\tau(\hat{T}+\hat{V}-E_\mathrm{T})} \right| \{\mathbf{r}\}' \right\rangle, \\ &\approx e^{-\delta\tau[V(\{\mathbf{r}\})-E_\mathrm{T}]/2} \left\langle \{\mathbf{r}\} \left| e^{-\delta\tau\hat{T}} \right| \{\mathbf{r}\}' \right\rangle e^{-\delta\tau[V(\{\mathbf{r}\}')-E_\mathrm{T}]/2}. \end{aligned} \tag{5.5}$$

In the above expression, we used the Trotter-Suzuki approximation for the exponential operator at short times, $e^{-\delta\tau(\hat{A}+\hat{B})} \approx e^{-\delta\tau\hat{B}/2}e^{-\delta\tau\hat{A}}e^{-\delta\tau\hat{B}/2} + \mathcal{O}(\delta\tau^3)$, and E_T is the trial energy, which plays a role similar to the shift S in FCIQMC to control the total population of the walkers. Noticing that the exponential operator containing only the kinetic operator $\hat{T}$ will yield a Gaussian distribution

as in the classical diffusion process, we obtain the final Green's function [47],

$$G(\{\mathbf{r}\} \leftarrow \{\mathbf{r}\}', \delta\tau) \approx (2\pi\delta\tau)^{-3N/2} e^{-\frac{(\{\mathbf{r}\}-\{\mathbf{r}\}')^2}{2\delta\tau}} e^{-\delta\tau[V(\{\mathbf{r}\})+V(\{\mathbf{r}\}')-2E_{\mathrm{T}}]/2}. \quad (5.6)$$

This propagator constitutes the following two crucial steps in the dynamics of a DMC simulation:

1. *Diffusion.* All existing walkers diffuse according to the diffusion equation, i.e. exploring the surrounding configurations randomly according to the $3N$ Gaussian distribution. Normally, the Metropolis algorithm [48] is used to update the positions of electrons.

2. *Birth/Death.* For each walker, it survives with the probability $P = e^{-\delta\tau[V(\{\mathbf{r}\})+V(\{\mathbf{r}\}')-2E_{\mathrm{T}}]/2}$, if $P < 1$; if $P \geq 1$, $\mathrm{int}(P)$ copies of the walker survive and an extra walker is created at the same configuration with probability $P - \mathrm{int}(P)$, where the function $\mathrm{int}(P)$ yields the largest integer that is smaller than P.

In principle, repeatedly applying this propagator on an initial wavefunction will yield a wavefunction that corresponds to the lowest eigenenergy of the Hamiltonian. However, since the imaginary-time Schrödinger equation in real position space imposes no antisymmetry on the wavefunction, without imposing additional constraints, the simulation will unavoidably converge to the bosonic ground state which has the same sign for all walkers' weight and always has an energy that is lower than or equal to the eigenenergy of the true fermionic ground state energy. This bosonic ground state is symmetric upon exchanging two identical electrons, which does not fulfill the antisymmetry requirement for fermionic systems. This is the so-called (fermion) sign problem that plagues all projector QMC methods, showing up with different characteristics in different flavors of method.

In DMC, a trial wavefunction Ψ_T is employed, whose nodes, where the wavefunction is 0, are used to impose the antisymmetry of the simulated ground state wavefunction. This is the so-called fixed-node diffusion Monte Carlo (FN-DMC) [49, 50, 47]. Additionally, the energy given by FN-DMC is an upper bound to the true ground state energy [47]. On the other hand, the trial wavefunction is normally also used as the guiding wavefunction for the importance sampling in FN-DMC. When chosen appropriately, the guiding wavefunction can significantly reduce the variance of the calculated properties, such as energy. A common way of choosing the trial wavefunction is using a product of a Slater-Jastrow factor and a Slater determinant (or a linear combination of

Slater determinants),

$$\Psi_T = e^{\hat{J}} \sum_i d_i \left|D_i^{\sigma}\right\rangle \left|D_i^{\bar{\sigma}}\right\rangle, \tag{5.7}$$

where the Slater-Jastrow factor $e^{\hat{J}}$ includes the correlation effects such as the nucleus-electron cusp and the electron-electron cusp, and the Slater determinants, with the spin-up and spin-down parts separated, determine the nodal structure of the trial wavefunction, hence that of the FN-DMC wavefunction, too. The parameters in the trial wavefunction are normally optimised within the VMC-based framework before the trial wavefunction is used in FN-DMC. In principle, the trial wavefunction which fixes the nodal structure and the guiding wavefunction for importance sampling need not be the same [51]. A systematic and efficient way of optimising the nodal structure is not so readily available. Existing methods include employing increasingly many Slater determinants in the trial wavefunction [52, 53] and an extrapolation to reach the exact energy, or using more flexible forms of the trial wavefunction such as artificial neural networks [54, 55, 56], just to name a few examples. For more details on the FN-DMC, we refer to Ref. [49, 50, 47, 44, 57] and the references therein, as they are beyond the scope of this thesis.

5.2 Full Configuration Interaction Monte Carlo

The FCIQMC theory is a stochastic version of the power method for solving for the eigenvector corresponding to the lowest or highest eigenvalue of a (massively large) matrix. It uses an ensemble of random walkers to represent the FCI wavefunction, as introduced in Sec. 3.2. The initial formulation of the method in Ref. [58] starts from the imaginary-time Schrödinger equation in the Slater determinant space, whose derivations will be followed here along with some later developments [59]. We introduce the time dependence in the FCI coefficients so that the wavefunction is also time dependent as it evolves according to the imaginary-time Schrödinger equation,

$$\left|\Psi(\tau)\right\rangle = \sum_i C_i(\tau) \left|D_i\right\rangle. \tag{5.8}$$

We also subtract the HF (or any other reference defined as $\left|D_0\right\rangle$) energy away from the diagonal of the many-electron Hamiltonian,

$$\hat{K} = \hat{H} - E_{\mathrm{HF}}. \tag{5.9}$$

The imaginary-time Schrödinger equation can then be formulated in the Slater determinant space as

$$-\frac{\mathrm{d}C_i}{\mathrm{d}\tau} = (K_{ii} - S)C_i + \sum_{j\neq i} K_{ij}C_j, \tag{5.10}$$

where for simplicity we drop the time dependence of the coefficients, $K_{ij} = \langle D_i|\hat{K}|D_j\rangle$ and S is a shift that is subtracted from the diagonal of the $\hat{K}$ matrix and is adjusted during the simulation to approximate the true ground state correlation energy $E^{\mathrm{c}}_{\mathrm{FCIQMC}}$. However, the above formalism still requires the storage of the full FCI coefficients. To evade this bottleneck, we approximate the coefficients C_i by walkers carrying signed weights w_i, [1] which are stochastically pruned away in each iteration with probability $|w_i|/c_p$ if $|w_i| < c_p$, where c_p is a parameter which is normally chosen to be 1. If not pruned, weights that have smaller magnitude than c_p are set to $w_i = sgn(w_i)c_p$ and those that have magnitude larger than c_p are left untouched. The wavefunction is then stored as a list of walker weights.

Eq. (5.10) can then be cast into a finite difference equation

$$\Delta w_i = -\delta\tau\left[(K_{ii} - S)w_i + \sum_{j\neq i} K_{ij}w_j\right], \tag{5.11}$$

which can be executed in three steps listed below:

1. *Spawning.* For the walker on determinant D_i with weight w_i, we pick randomly a connected determinant D_j, which means $\langle D_j|\hat{H}|D_i\rangle \neq 0$, with probability $p_{\mathrm{gen}}(j|i)$, on which we spawn a new walker with weight $w_j^\alpha = -\frac{\delta\tau K_{ij}w_i}{p_{\mathrm{gen}}(j|i)m_i}$, where we use index α to denote the new walker on the list of spawned walkers, because there might be some other new walkers being spawned to determinant D_j by determinants other than D_i. We loop over all walkers to do the same in the list of the wavefunction. The number of spawning attempts, m_i, each walker tries can be set to be proportional to the magnitude of its weight and $p_{\mathrm{gen}}(j|i)$ can be calculated in a way such that it is approximately proportional to $\frac{|K_{ij}|}{\sum_{j\neq i}|K_{ij}|}$.

2. *Death/Cloning.* We loop over all walkers in the list of the wavefunction, to change the weight of each walker by $d_i = -\delta\tau(K_{ii} - S)w_i$. Depending on the sign of d_i, the process is called either death ($d_i < 0$) or cloning

[1] The very first implementation of FCIQMC used integer weight for each walker, which was later abandoned for real valued weight.

($d_i > 0$). We denote the list of the weights of walkers after this step as $w'_i = w_i + d_i$.

3. *Annihilation.* We combine the lists of the wavefunction and the newly spawned walkers. Using a hash table, one can efficiently find the walkers belonging to the same determinant, combine their weights, and remove repeated entries of the same determinant. The new weights of determinants in the list of the wavefunction is $w''_i = w'_i + \sum_\alpha w_i^\alpha$. w''_i will be used as w_i in the next iteration.

As mentioned above, the pruning of the weights is applied after they are updated, so that we can keep the storage of walkers tractable. As pointed out in Ref. [60], the choice of the time step size has to satisfy $\delta\tau \leq \frac{2}{E_{\max}-E_0}$ for discrete Hilbert space, where $E_{\max}$ (E_0) is the largest (smallest) eigenvalue of $\hat{H}$. The shift S is adjusted during the simulation according to

$$S(\tau) = S(\tau - A\delta\tau) - \frac{\eta}{A\delta\tau}\ln\frac{N_w(\tau)}{N_w(\tau - A\delta\tau)}, \tag{5.12}$$

where $N_w(\tau) = \sum_i |w_i(\tau)|$, η is the damping parameter and A is the period of steps, at which we adjust the value of S. The shift is adjusted so that the total population of the walkers remain constant after reaching a preset target. Using the Slater-Condon rules [61, 62, 16], one can evaluate the Hamiltonian matrix elements efficiently on-the-fly, assuming the integrals are precomputed and stored in computer memory.

Finally, the projected correlation energy is calculated as

$$\begin{aligned} E^{\mathrm{c}}_{\mathrm{FCIQMC}} &= \frac{\langle D_0|\hat{K}|\Psi\rangle}{\langle D_0|\Psi\rangle} \\ &= \frac{\sum_{j\neq 0} K_{0j} w_j}{w_0}, \end{aligned} \tag{5.13}$$

which at convergence should agree with the shift S. The original FCIQMC requires a system-dependent critical number of walkers to reach the exact solution, which underpins the exponential growth in computational cost with system size of the algorithm. If a smaller number of total walkers are used than the critical number, the simulation will collapse to an undesired solution that has a lower energy than the true ground state energy, signalling a typical behavior of the sign problem.

Later development introduced the *initiator approximation* [59] which removes the need to reach the system-dependent critical number of walkers in order to sustain a stable simulation. However it introduces some bias which

can be reduced systematically as the target number of walkers is increased to infinity. The bias associated with this approximation is called the *initiator error* and the algorithm is named *i*-FCIQMC. We recap briefly the main ingredients of this approximation. Firstly, an initiator criteria c_{ini} is set, for example to 3, which divides the list of walkers into the initiator and non-initiator space. The walkers in the initiator space have weights larger than c_{ini} and can spawn child walkers to determinants that do not exist in the current list of walkers, while the non-initiator walkers have weights smaller than c_{ini} and can only spawn child walkers to the already existing determinants in the list of walkers, with an exception when two non-initiator walkers on two different determinants spawn child walkers with the same sign on the same new determinant.

5.3 Discussion

FCIQMC operates in discrete configurational space, which has the antisymmetry built in the many-electron basis, such as the Slater determinants. This has two advantages: 1. Positive and negative walkers can be easily identified to be on the same Slater determinant or not, hence easily annihilate each other; 2. With the antisymmetry built in, the correct wavefunction can emerge automatically once a sufficient number of walkers are used. In contrast, DMC uses walkers in real space, which can have continuous and infinitely many possible configurations. On one hand, this gives it an edge that by construction DMC yields energy at the CBS limit. On the other hand, no antisymmetry is present in the generic walker representation of the wavefunction, and annihilation between positive and negative walkers is not so straightforward to implement. Fortunately, in real space, the wavefunction has well separated positive and negative regions and the walker dynamics given by Eq. (5.6) at each short time step does not move/create walkers in a non-local fashion, therefore it is feasible to use the fixed-node approximation to enforce the antisymmetry of the wavefunction. Unlike the Hamiltonian in real space representation, the Hamiltonian in Slater determinant space representation normally has complicated sign structures, hence the signs of walkers change during the dynamics. Due to the fact that it is not so straightforward to define neighboring Slater determinants, defining the nodal structure as in DMC becomes hard, if not impossible, in FCIQMC. The origin of the sign problem in FCIQMC is well explained in Ref. [63] as a collapsing to the ground state of a Hamiltonian which has the off-diagonal elements being $-|H_{ij}|$ when not enough walkers are used and positive and negative walkers barely meet to annihilate each other.

This "bosonic" Hamiltonian has a lower ground state energy than the original Hamiltonian, so that the signal of the true wavefunction decays exponentially $e^{-\Delta E \tau}$, where ΔE is the energy difference between the true fermionic ground state energy and the "bosonic" ground state energy [2]. In DMC, the situation is similar, the wavefunction will collapse into the bosonic wavefunction exponentially fast when no external antisymmetry is imposed, for example by the fixed-node approximation [49, 50].

[2] In rare cases, the "bosonic" and fermionic ground state energies are the same and no sign problem exist in these systems in FCIQMC

Chapter 6

Finite Size Corrections

For periodic solids, properties calculated at the TDL are needed in order to compare with experiments meaningfully. Because, on one hand, in any supercell that comprises a finite number of unit cells, the momenta of the electrons are quantized, see Eq. (1.18), as a result of which strong fluctuations in the calculated properties as a function of the size of the supercell can occur, which will not go away until large enough supercells are used and the possible values of the momenta become more or less continuous; on the other hand, some electronic correlations span a distance that is longer than the length of the supercells. We define the finite size errors of a calculated property as the difference between the ideal value at TDL and the one that is currently simulated with a size N. For example, for the ground state energy it is defined as

$$\Delta E_{\mathrm{FS}} = E_{\infty} - E_N. \tag{6.1}$$

The most straightforward way to reach the TDL is to simulate increasingly larger numbers of supercells or denser k-meshes in reciprocal space, and then extrapolate the quantity in question to the TDL. The bad news is that many of the methods that we have discussed so far have very steep scaling in computational cost with the system size, which renders this obvious way intractable with modern computers. In the following two sections, we discuss two ways to correct the finite size errors: one is to tackle the problem caused by the quantized momenta; the other is to recover the long range correlations that are missing in small supercells.

6.1 Twist-averaging Technique

The basic idea of twist-averaging (TA) is to use the average of an ensemble of simulations that sample the first Brillouin zone coarsely at different k-points, i.e. Δk_i (twists), to approximate the ideal situation where the first Brillouin

zone is densely sampled. For example, the twist-averaged correlation energy is

$$E^{\mathrm{c}}_{\mathrm{TA}} = \frac{1}{\sum_i w_i} \sum_i w_i E^{\mathrm{c}}_{\Delta k_i}, \tag{6.2}$$

where Δk_i is a twist that applies to the Γ-point in the first Brillouin zone, assuming that only the Γ-point is sampled, and w_i is the weight of this shift, which is determined by the number of equivalent k-points, generated by symmetry operations, to Δk_i in the first Brillouin zone. The number of twists can be increased until the twist-averaged quantity does not change any more. For more details, we refer to Ref. [64, 65, 66, 67, 68].

6.2 Long Range Correlations

The correlation energy of wavefunction-based quantum chemical methods, such as MP2, CCSD and FCIQMC can be expressed in general as

$$E^{\mathrm{c}} = C^{ab}_{ij}(2V^{ij}_{ab} - V^{ij}_{ba}), \tag{6.3}$$

where C^{ab}_{ij} are the coefficients of the doubly excited SDs. For example, in CCSD, $C^{ab}_{ij} = T^{ab}_{ij} + T^a_i T^b_j$.

In the plane wave basis, the Coulomb integrals, Eq. (4.4), can be calculated as

$$V^{ab}_{ij} = \sum_{\mathbf{G}\neq\mathbf{0}} D^{i*}_a(\mathbf{G}) V(\mathbf{G}) D^b_j(\mathbf{G}), \tag{6.4}$$

where $D^a_i(\mathbf{G}) = \int \mathrm{d}\mathbf{r}\varphi^*_a(\mathbf{r})\varphi_i(\mathbf{r})e^{\mathrm{i}\mathbf{G}\cdot\mathbf{r}}$ and $V(\mathbf{G}) = \frac{4\pi}{|\mathbf{G}|^2}$ is the Fourier transformed Coulomb potential. In practice, the $\mathbf{G} = \mathbf{0}$ component is normally left out in the summation, due to the integrable divergence in $V(\mathbf{G})$ at this point. This is one of the main sources for the finite size errors.

If we insert Eq. (6.4) into Eq. (6.3) and change the order of summations in Eq. (6.3), such that the $abij$ indices are summed over first and the $\mathbf{G}$ index is summed over next, we obtain the following expression, where we use explicit summations to indicate the order of summations,

$$E^{\mathrm{c}} = \sum_{\mathbf{G}\neq\mathbf{0}} V(\mathbf{G}) \sum_{abij} C^{ab}_{ij} \left(2D^{i*}_a(\mathbf{G}) D^b_j(\mathbf{G}) - D^{i*}_b(\mathbf{G}) D^a_j(\mathbf{G})\right). \tag{6.5}$$

Following Ref. [69, 70], we define the transition structure factor as

$$S(\mathbf{G}) = \sum_{abij} C^{ab}_{ij} \left(2D^{i*}_a(\mathbf{G}) D^b_j(\mathbf{G}) - D^{i*}_b(\mathbf{G}) D^a_j(\mathbf{G})\right), \tag{6.6}$$

using which the correlation energy can be written compactly as

$$E^{\mathrm{c}} = \sum_{\mathbf{G}\neq\mathbf{0}} V(\mathbf{G})S(\mathbf{G}). \tag{6.7}$$

We notice that the $S(\mathbf{G})$ is a function defined on a three-dimensional grid, $\mathbf{G}$. To recover the missing contribution at $\mathbf{G} = \mathbf{0}$, the original $S(\mathbf{G})$ is interpolated on a much finer grid $\mathbf{g}$ and the discrete summation over the coarse $\mathbf{G}$ grid is replaced by the summation over $\mathbf{g}$, which can be effectively expressed by an integral

$$E^{\mathrm{c}}_{\infty} = \int \mathrm{d}\mathbf{g} V(\mathbf{g})\tilde{S}(\mathbf{g}), \tag{6.8}$$

where we use $\tilde{S}(\mathbf{g})$ as the interpolated $S(\mathbf{G})$.

Due to the orthogonality between the occupied and the virtual orbitals, $S(\mathbf{0}) = 0$. So that the Taylor expansion of $S(\mathbf{G})$ around $\mathbf{G} = \mathbf{0}$ has the first nonzero term proportional to $\mathbf{G}^2$, hence the product $V(\mathbf{G})S(\mathbf{G})$ approaches a constant as $\mathbf{G} \to \mathbf{0}$. As larger supercells or denser k-meshes are used, the shortest $\mathbf{G}_{\mathrm{min}}$ gets closer to the origin, thus more long range correlations are recovered. Using Eq. (6.8), not only the missing contribution at $\mathbf{G} = \mathbf{0}$ can be recovered, but also the quadrature errors from a summation over a very coarse grid $\mathbf{G}$ can be reduced. Similar methodologies [64, 65, 67, 68] are used in DMC, where the structure factor is used for this purpose.

Chapter 7

A Perturbative Approach to the Electron-Phonon Interactions

Phonons are the collective motions of atoms inside of a lattice. They are bosons. So far, we have ignored the motions of the nuclei, which in reality can have important contributions to the properties of solids. For example, the band gaps in solids can change due to the motions of atoms, compared to the values at 0 K. Even at the 0 K, the atoms are still in motion, due to the zero point fluctuations, arising from the uncertainty principle. Especially, for those solids that consist of light elements, such as the solid hydrogen phases, the EPIs are strong and not negligible.

Within the BO approximation, the motions of nuclei are determined by Eq. (1.9), with the potential being the ground state energy of the electronic Schödinger equation. With small displacements around their equilibrium positions, the nuclei can be modelled by the quantum Harmonic oscillators, of which the Hamiltonian can be written in terms of phonon creation and annihilation operators

$$\hat{H}_n = \sum_{\mathbf{q}\nu} \omega_{\mathbf{q}\nu} \left(c^\dagger_{\mathbf{q}\nu} c_{\mathbf{q}\nu} + \frac{1}{2} \right), \tag{7.1}$$

where $\omega_{\mathbf{q}\nu}$ is the frequency (energy) [1] of a phonon mode with crystal momentum $\mathbf{q}$ on branch ν. The $\frac{1}{2}$ inside of the bracket constitutes the zero point energy of the nuclei.

In this chapter, a perturbative approach will be introduced to include to some extend the effects of EPI on properties such as the band gaps in solids. At this stage, we reiterate the KS single-particle Hamiltonian,

$$\hat{H}_{\mathrm{KS}} = -\frac{1}{2}\nabla_i^2 - \sum_{\mu}^{K} \frac{Z_\mu}{|\mathbf{r} - \mathbf{R}_\mu|} + \int \mathrm{d}\mathbf{r}' \frac{n(\mathbf{r}')}{|\mathbf{r} - \mathbf{r}'|} + V_{\mathrm{XC}}[n(\mathbf{r})]. \tag{7.2}$$

[1] In atomic units, these two are the same, since $\hbar = 1$.

The three potential terms either depend explicitly or implicitly on the nuclei's positions, which we group together as

$$V_{\mathrm{KS}}(\mathbf{r};\{\mathbf{R}\}) = -\sum_{\mu=1}^{K}\frac{Z_\mu}{|\mathbf{r}-\mathbf{R}_\mu|} + \int \mathrm{d}\mathbf{r}'\frac{n(\mathbf{r}')}{|\mathbf{r}-\mathbf{r}'|} + V_{\mathrm{XC}}[n(\mathbf{r})], \tag{7.3}$$

where we introduce explicitly the positions of the nuclei as a dependence in the KS potential. When the nuclei are allowed to move around their equilibrium positions $\{\mathbf{R}^0\}$, Eq. (7.3) can be expanded around those positions as

$$\begin{aligned} V_{\mathrm{KS}}(\mathbf{r};\{\mathbf{R}\}) = V_{\mathrm{KS}}(\mathbf{r};\{\mathbf{R}^0\}) &+ \sum_\mu \nabla_{\mathbf{R}_\mu} V_{\mathrm{KS}}(\mathbf{r};\{\mathbf{R}\})\big|_{\mathbf{R}_\mu=\mathbf{R}^0_\mu}\Delta\mathbf{R}_\mu \\ &+ \frac{1}{2}\sum_\mu\sum_{\mu'}\nabla_{\mathbf{R}_\mu}\nabla_{\mathbf{R}_{\mu'}} V_{\mathrm{KS}}(\mathbf{r};\{\mathbf{R}\})\Big|_{\mathbf{R}_\mu=\mathbf{R}^0_\mu;\mathbf{R}_{\mu'}=\mathbf{R}^0_{\mu'}}\Delta\mathbf{R}_\mu\Delta\mathbf{R}_{\mu'} + \dots. \end{aligned} \tag{7.4}$$

In the theory developed by Allen and Heine [71] and a later development by Allen and Cardona [72], which is called the HAC or AHC theory, only the diagonal terms in the second order derivatives are considered. We define two perturbations as

$$\begin{aligned} \hat{H}_1 &= \sum_\mu \nabla_{\mathbf{R}_\mu} V_{\mathrm{KS}}(\mathbf{r};\{\mathbf{R}\})\big|_{\mathbf{R}_\mu=\mathbf{R}^0_\mu}\Delta\mathbf{R}_\mu, \\ \hat{H}_2 &= \frac{1}{2}\sum_\mu \nabla_{\mathbf{R}_\mu}\nabla_{\mathbf{R}_\mu} V_{\mathrm{KS}}(\mathbf{r};\{\mathbf{R}\})\big|_{\mathbf{R}_\mu=\mathbf{R}^0_\mu}\Delta\mathbf{R}_\mu\Delta\mathbf{R}_\mu. \end{aligned} \tag{7.5}$$

According to Ref. [71], the perturbatively corrected KS energies, up to the second order in nuclei displacements, are

$$\tilde{\epsilon}_{n\mathbf{k}}(\{\Delta\mathbf{R}\}) = \epsilon_{n\mathbf{k}} + \left\langle \varphi_{n\mathbf{k}} \middle| \hat{H}_1 + \hat{H}_2 \middle| \varphi_{n\mathbf{k}} \right\rangle + {\sum_{n'\mathbf{k}'}}' \frac{\left|\left\langle \varphi_{n'\mathbf{k}'} \middle| \hat{H}_1 \middle| \varphi_{n\mathbf{k}} \right\rangle\right|^2}{\epsilon_{n\mathbf{k}} - \epsilon_{n'\mathbf{k}'}}, \tag{7.6}$$

where the prime on the summation indicates that the term when $n = n'$ and $\mathbf{k} = \mathbf{k}'$ is omitted. The temperature dependence is introduced in the quasiparticle energies by replacing the parts involving the displacements $\Delta\mathbf{R}$ with their thermally averaged counterparts, see Equation (4) in Ref. [71].

Here we show the temperature dependent quasiparticle energies from Ref. [73, 74, 75, 76], where some further developments are made based on the HAC theory,

$$\tilde{\epsilon}_{n\mathbf{k}}(T) = \epsilon_{n\mathbf{k}} + \left[1 - \frac{\partial \mathrm{Re}\Sigma^{\mathrm{Fan}}_{n\mathbf{k}}(\omega,T)}{\partial\omega}\bigg|_{w=\epsilon_{n\mathbf{k}}}\right]^{-1}\left[\Sigma^{\mathrm{Fan}}_{n\mathbf{k}}(\epsilon_{n\mathbf{k}},T) + \Sigma^{\mathrm{DW}}_{n\mathbf{k}}(T)\right], \tag{7.7}$$

where the Fan term is

$$\Sigma_{n\mathbf{k}}^{\mathrm{Fan}}(\omega,T)=\sum_{n'\mathbf{q}\nu}\frac{|g_{nn'\nu}^{\mathrm{Fan}}(\mathbf{k},\mathbf{q})|^2}{N_q}\left[\frac{n_{\mathbf{q}\nu}(T)+1-f_{n'\mathbf{k}-\mathbf{q}}}{\omega-\epsilon_{n'\mathbf{k}-\mathbf{q}}-\omega_{\mathbf{q}\nu}+\mathrm{i}\eta\mathrm{sgn}(\omega)}+\frac{n_{\mathbf{q}\nu}(T)+f_{n'\mathbf{k}-\mathbf{q}}}{\omega-\epsilon_{n'\mathbf{k}-\mathbf{q}}+\omega_{\mathbf{q}\nu}+\mathrm{i}\eta\mathrm{sgn}(\omega)}\right], \tag{7.8}$$

and the Debye-Waller term is

$$\Sigma_{n\mathbf{k}}^{\mathrm{DW}}(T)=-\frac{1}{2}\sum_{n'\mathbf{q}\nu}\frac{g_{nn'\nu}^{\mathrm{DW}}(\mathbf{k},\mathbf{q})}{N_p}\left[\frac{2n_{\mathbf{q}\nu}(T)+1}{\epsilon_{n\mathbf{k}}-\epsilon_{n'\mathbf{k}'}}\right]. \tag{7.9}$$

In the above two expressions, $n_{\mathbf{q}\nu}(T)$ and $f_{n'\mathbf{k}-\mathbf{q}}$ refer to the Bose-Einstein and Fermi-Dirac distribution functions, respectively. The expressions for the matrix elements $g_{nn'\nu}^{\mathrm{Fan}}(\mathbf{k},\mathbf{q})$ and $g_{nn'\nu}^{\mathrm{DW}}$ can be found, for example, in Ref. [75, 76].

The perturbative corrections are based on the BO approximation and the model of Harmonic oscillator for the nuclei motions. In many situations when the atoms are heavy and the temperature is low, both are good approximations. But they can break down when the atoms are light and the temperature is high.

Part III

New Theoretical Developments

Chapter 8

MP2 Forces and Structural Optimisation

This chapter contains partly the work published in the paper titled "Structural and Electronic Properties of Solid Molecular Hydrogen from Many-electron Theories", by Ke Liao, Tong Shen, Xin-Zheng Li, Ali Alavi and Andreas Grüneis on Physical Review B, 103, 054111. Ke Liao implemented the MP2 forces algorithm, with helpful discussions with Andreas Grüneis.

8.1 Motivations

The relative cheap cost of DFT enables it to do massive crystal structure search. Although DFT can find relevant structures that are of interest, the approximate XC functionals used in DFT cause uncontrollable errors in the resulting structures. These structures can result in inaccurate predictions compared to experiments, such as transition pressures in pressure induced structural transitions or band gaps when studying the electronic properties. Hence, a more accurate source of atomic forces is needed. From the wavefunction methods, MP2 is such a candidate. A direct motivation for the development and implementation of the MP2 forces is that in this thesis we aim to predict the atomic structures of crystalline molecular hydrogen phases and related properties, enabling a more rigorous study of band gaps and vibrational frequencies. For more details, we refer to chapter 11. In the meantime, to the best of our knowledge, we notice that a theoretical formulation and an implementation of the MP2 forces using a pure plane wave basis set is still missing in the literature.

8.2 Theoretical Formulation

In this section, we briefly recapitulate the general theoretical formulation of analytical gradients given by the MP2. For the more details, we refer to [77, 78,

79], in particular we follow the derivation from Ref. [78] closely. We point out that in these Refs, either pure localised Gaussian basis functions or a mixture of Gaussian and plane wave basis functions are used.

Starting from the mean-field HF method, MP2 theory adds correlation effects to observables. For example, the total energy can be expressed as

$$E_{\mathrm{MP2}} = E_{\mathrm{HF}} + E_{\mathrm{MP2}}^{\mathrm{corr}}. \tag{8.1}$$

Therefore the nuclear gradients

$$\mathbf{F} = -\frac{\partial E}{\partial \mathbf{R}}, \tag{8.2}$$

where $\mathbf{R}$ is a vector of all nuclear coordinates, can also be written as a sum of two contributions

$$\mathbf{F} = \mathbf{F}_{\mathrm{HF}} + \mathbf{F}_{\mathrm{MP2}}^{\mathrm{corr}}. \tag{8.3}$$

For a closed-shell system, the MP2 correlation energy can be expressed as

$$E_{\mathrm{MP2}}^{\mathrm{corr}} = \sum_{ijab} T_{ij}^{ab} V_{ab}^{ij}, \tag{8.4}$$

$$T_{ij}^{ab} = \frac{2V_{ij}^{ab} - V_{ij}^{ba}}{\epsilon_i + \epsilon_j - \epsilon_a - \epsilon_b}, \tag{8.5}$$

where the indices i, j and a, b refer to the occupied and unoccupied HF orbitals, respectively, and the $\epsilon_{i,j,a,b}$ are the corresponding orbital energies. Here we adopt the convention to use $i, j, k, l, \ldots$, $a, b, c, d, \ldots$ and $p, q, r, s, \ldots$ as occupied, unoccupied and general orbital indices, respectively. In the present work, all (pseudo) orbitals are expressed as linear combinations of the underlying plane wave basis functions, *i.e.*

$$\phi_p(\mathbf{r}) = \sum_{\mu} c_{\mu p} e^{i\mathbf{G}_\mu \cdot \mathbf{r}}, \tag{8.6}$$

where the coefficients $c_{\mu p}$ are determined through a self consistent minimisation of the HF energy. $\mathbf{G}_\mu$ is a plane wave vector and $\mathbf{r}$ is the electronic coordinate.

Within the Born-Oppenheimer approximation, the orbitals and their energies depend parametrically on the nth nuclear position $\mathbf{R}_n$, which are not shown in equation 8.5. Using a plane wave basis, the derivative of the MP2 correlation energy with respect to $\mathbf{R}_n$ can be expressed concisely as

$$E_{\mathrm{MP2}}^{\mathrm{corr}'} = \frac{\partial E_{\mathrm{MP2}}^{\mathrm{corr}}}{\partial \mathbf{R}_n} = 2 \sum_{pq} P_{pq} F'_{pq}, \tag{8.7}$$

where the prime on quantities refer to their derivatives with respect to $\mathbf{R}_n$, the density matrix is defined as a direct sum of the occupied-occupied, unoccupied-unoccupied and occupied-unoccupied blocks

$$P_{pq} = P_{ij} \oplus P_{ab} \oplus P_{ai}, \tag{8.8}$$

and the derivative on the Fock matrix is

$$F'_{pq} = \sum_{\nu\mu} c_{\nu p} c_{\mu q} h'_{\nu\mu}, \tag{8.9}$$

where $h'_{\nu\mu} = \nabla_{\mathbf{R}} < \nu|\frac{1}{\mathbf{R}-\mathbf{r}}|\mu >$ can be obtained by taking the derivative in momentum space.

The occupied-occupied and unoccupied-unoccupied blocks of the density matrix can be expressed in the following closed expressions

$$P_{ij} = -\sum_{abk} T_{ik}^{ab} \frac{V_{ab}^{jk}}{\epsilon_i + \epsilon_k - \epsilon_a - \epsilon_b}, \tag{8.10}$$

$$P_{ab} = \sum_{ijc} T_{ij}^{ac} \frac{V_{bc}^{ij}}{\epsilon_i + \epsilon_j - \epsilon_b - \epsilon_c}. \tag{8.11}$$

The occupied-unoccupied block, which includes the orbital relaxation effects as we perturb the nuclear coordinates, can be obtained by solving the Z-vector equation

$$L"_{ai} - L_{ia} - \sum_{pq} A_{apiq}(P_{ij} + P_{ab}) = (\epsilon_a - \epsilon_i)P_{ai} + \sum_{bm} A_{abim} P_{bm}, \tag{8.12}$$

where the intermediate quantities are defined as

$$L_{ia} = 2\sum_{cbj} T_{ij}^{cb} V_{cb}^{aj}, \tag{8.13}$$

$$L"_{ai} = 2\sum_{bkj} T_{kj}^{ab} V_{bi}^{jk}, \tag{8.14}$$

$$A_{prqs} = 4V_{qs}^{pr} - V_{sq}^{pr} - V_{rq}^{ps}. \tag{8.15}$$

An iterative conjugate gradient solver is well suited for solving the Z-vector equation (8.12).

8.3 Structure Optimisation Using Symmetrised MP2 Forces

Computing the MP2 forces is computationally much more expensive than the DFT forces. Therefore we employ structures optimised on the level of DFT-PBE as a suitable starting point. Since the DFT energy minima are close to the MP2's, a simple gradient descent solver suffices to update the structures and find the most stable MP2 structures. Additionally, due to numerical noise and other possible convergence errors, the computed gradients may not preserve the space group symmetry of the initial structure. Therefore, after a few iterations of updating the nuclear positions, the structures can slide into another space group symmetry. This is not necessarily an unwanted feature in, for example, random searches for the most stable configurations. However, in this work we want to keep the space group symmetries fixed. We achieve this goal by symmetrising the computed gradients using the corresponding symmetry operations.

8.3.1 Gradient Descent Method

In the gradient descent method, we approximate the energy changes with respect to the changes in the nuclear positions using the first gradient

$$\Delta E = \sum_{\mathbf{n}} \frac{\partial E}{\partial \mathbf{R}_n} \Delta \mathbf{R}_n, \tag{8.16}$$

and choose the changes in nuclei positions to be

$$\Delta \mathbf{R}_n = -\delta \sum_{\mathbf{n}} \frac{\partial E}{\partial \mathbf{R}_n} = \delta \mathbf{F}_n, \tag{8.17}$$

where δ is a small positive constant which we denote as the time step during the structure optimisation procedure. In this case, after we update the nuclei positions, comparing to the previous configuration, the energy is lowered by

$$\Delta E = -\delta \sum_{\mathbf{n}} \left| \frac{\partial E}{\partial \mathbf{R}_n} \right|^2 = -\delta \sum_{\mathbf{n}} |\mathbf{F}_n|^2 < 0. \tag{8.18}$$

8.3.2 Symmetrising the Forces Using Space Group Symmetries

A space group element (operation) is a combination of a point group operation (rotation) $\mathbf{M}$ and a translation operation $\mathbf{T}$. Considering a space group which

has N elements, we have N pairs of $\mathbf{R}$ and $\mathbf{T}$ operations. Applying one element to the coordinates of the nuclear positions $\{\mathbf{R}\}$, we get

$$\mathbf{R}_i'^n = \mathbf{M}_n\mathbf{R}_i + \mathbf{T}_n, \tag{8.19}$$

where i denotes the ith nuclear position in $\{\mathbf{R}\}$ and n represents the nth element from the space group. As per definition of a symmetry operation, we should have two equivalent sets of coordinates $\{\mathbf{R}'\} \equiv \{\mathbf{R}\}$. Concomitantly, the forces are also transformed by the rotation operation and we use the information from equation (8.19) to determine the atoms which they act upon. So the transformed forces are

$$\mathbf{F}_i'^n = \mathbf{M}_n\mathbf{F}_i, \tag{8.20}$$

and the average of forces from all the equivalent atoms resulting from all the operations are the symmetrised forces

$$\bar{\mathbf{F}}_i = \frac{1}{N}\sum_n \mathbf{F}_i'^n. \tag{8.21}$$

As mentioned before, the HF forces are calculated using the primitive cells and dense k-meshes, while the MP2 forces are calculated using large supercells and the Γ-point only. To update the coordinates of atoms inside of the primitive cell, the following 4-step procedure is carried out:

1. symmetrising the MP2 forces using the space group symmetries of the supercell cell.

2. downfolding the supercell to the primitive cell by mapping the indices, positions and forces of the atoms between the supercell and the primitive cell.

3. symmetrising the MP2 and HF forces using the space group symmetries of the primitive cell.

4. updating the atomic positions.

8.4 Implementation Details

Compared to the formulation using atom-centered Gaussian basis sets, plane wave basis functions simplify the expressions for the gradients significantly. However a relatively large number of plane waves are required to describe the core regions of the wavefuntions that are close to the nuclei. In general, the

projector augmented wave (PAW) method[80, 81], which is implemented in `VASP`[82], reduces the required plane wave basis set size. However, in this work we did not employ the PAW method when computing the MP2 contribution to the gradients. Only the HF forces are computed within the PAW framework, as implemented in `VASP`. We also note that for systems consisting of light atoms, e.g. hydrogen, it is not so difficult to converge the MP2 forces with respect the number of plane wave basis functions. The MP2 analytical gradient has been implemented in `CC4S`, which uses the `Cyclops Tensor Framework` (CTF)[83] as the backend for massively parallel tensor operations. For the HF part, we sample the 1st Brillouin zone using dense k-mesh; for the MP2 part, we use only the Γ-point and employ large supercells instead. The Python library Spglib [84] is used for symmetry operations.

Chapter 9

Combining Transcorrelation and Coupled Cluster Theory

This chapter contains partly the work in the paper titled "Towards efficient and accurate *ab initio* solutions to periodic systems via transcorrelation and coupled cluster theory", by Ke Liao, Thomas Schraivogel, Hongjun Luo, Daniel Kats and Ali Alavi, published on Physical Review Research, 3, 033072 (2021). Ke Liao, Daniel Kats and Ali Alavi conceived this project and contributed to the writing of the manuscript; Ke Liao implemented the TC-CC algorithm; Thomas Schraivogel contributed to the resolving of several important bugs; Hongjun Luo contributed to the full 3-body interactions in the FCIQMC algorithm and some theoretical developments in the TC integrals.

9.1 Motivations

The coupled cluster (CC) methodologies [85, 86, 32] at the level of singles and doubles (CCSD) and perturbative triples (CCSD(T)) [41] have become the *de facto* standard of single-reference *ab initio* quantum chemistry, and can be applied to systems consisting of hundreds of electrons [87, 88, 89, 90]. In the past few years, these methods have also shown promise in applications to the solid state [91, 69, 92, 70, 93, 94], although significant challenges remain before they can be routinely applied, as for example density functional theories are. On the one hand, because of quite steep computational scaling ($\mathcal{O}(N^6)$ and $\mathcal{O}(N^7)$ for CCSD and CCSD(T) respectively), it is desirable to keep the methods at the lowest possible CC level, namely CCSD, whilst maintaining accuracy. The more accurate CCSD(T), as a perturbative correction to CCSD, additionally fails for metals [43]. It is also desirable that the CC methods can be extended to more strongly correlated systems, where the single reference nature of these approximations breaks down. There have been various attempts to develop modified CCSD methods with a higher accuracy for weakly [95, 96, 97, 98]

and strongly [99, 100, 101, 102, 103] correlated systems. The distinguishable cluster singles and doubles (DCSD) [35, 104] is one such method, which has shown promise in improving CCSD in weakly and strongly correlated molecular systems [105, 106, 107].

In a separate development, there has been renewed interest in so-called transcorrelated (TC) methods [108, 2, 3, 109, 110, 111, 112, 113, 114, 115, 116, 117, 118, 119, 120], based on Jastrow factorisation of the electronic wavefunction, which result in effective similarity transformed (ST) Hamiltonians [116, 119]. Although TC methods were originally proposed as a way to accelerate basis set convergence in electronic wavefunctions, it has become apparent that such similarity transformations can also be extremely helpful in the context of strongly correlated systems. For example, in the repulsive 2D Fermi-Hubbard model, it was found that, with a suitable Gutzwiller correlator, extremely compact forms of ground state right eigenvectors of the ST Hubbard Hamiltonian could be obtained [118], dominated by the Hartree-Fock (HF) determinant. Since single-reference coupled cluster methods work best when the wavefunction is dominated by the HF determinant, and furthermore, since the coupled cluster method can itself be cast in terms of a similarity transformation of the Hamiltonian, it is natural to ask if the two concepts - coupled cluster and transcorrelation - can be usefully combined into a single framework, whereby the compactification generated by the TC method is exploited by the CC method, to extend its range of applicability into more strongly correlated systems.

9.2 Transcorrelation

In the transcorrelation framework the many-electron wavefunction is written as

$$\Psi = e^{\hat{\tau}}\Phi \tag{9.1}$$

where $\hat{\tau} = \frac{1}{2}\sum_{i\neq j} u(\mathbf{r_i}, \mathbf{r_j})$ is a correlator consisting of pair correlations $u(\mathbf{r_i}, \mathbf{r_j})$, whose form will be discussed later. Φ should satisfy the similarity-transformed eigenvalue equation

$$\hat{H}_{\text{tc}}\Phi = E\Phi, \quad \hat{H}_{\text{tc}} = e^{-\hat{\tau}}\hat{H}e^{\hat{\tau}}. \tag{9.2}$$

It is worth pointing out that at this stage, no approximations have been made, and the spectra E of $\hat{H}_{\text{tc}}$ are the same as of the original Hamiltonian.

The similarity-transformed Hamiltonian can be expanded by the Baker-Campbell-Hausdorff expansion. Due to the fact that the correlator is a function of the spatial coordinates of electrons, the expansion truncates at the double

commutation as follows [116]

$$\begin{aligned}\hat{H}_{\text{tc}} &= \hat{H} + \left[\hat{H}, \hat{\tau}\right] + \frac{1}{2}\left[\left[\hat{H}, \hat{\tau}\right], \hat{\tau}\right] \\ &= \hat{H} - \sum_i \left(\frac{1}{2}\nabla_i^2\hat{\tau} + \nabla_i\hat{\tau}\cdot\nabla_i + \frac{1}{2}(\nabla_i\hat{\tau})^2\right).\end{aligned} \tag{9.3}$$

The TC Hamiltonian has additional 2-body and 3-body interactions. The last term in Eq. (9.3) gives rise to a 2-body and the 3-body terms. Due to one of the additional 2-body interactions, the TC Hamiltonian is non-hermitian. This fact can pose some difficulties for variational methods, but not so for projection methods such as full configuration interaction Monte Carlo (FCIQMC) [58, 91] and CC.

9.3 Approximations to the Three-body Operator

In general, we can write the TC Hamiltonian in second quantization as

$$\begin{aligned}\hat{H}_{\text{tc}} = \hat{H} &+ \frac{1}{2}\sum_{\sigma\sigma'}\sum_{pqrs}\omega_{pq}^{rs}a_{p,\sigma}^\dagger a_{q,\sigma'}^\dagger a_{s,\sigma'}a_{r,\sigma} \\ &+ \frac{1}{6}\sum_{\sigma\sigma'\sigma''}\sum_{pqorst}\omega_{pqo}^{rst}a_{p,\sigma}^\dagger a_{q,\sigma'}^\dagger a_{o,\sigma''}^\dagger a_{t,\sigma''}a_{s,\sigma'}a_{r,\sigma},\end{aligned} \tag{9.4}$$

where we group all the additional 2-body integrals as ω_{pq}^{rs}.

The additional 3-body operator when treated without approximations will increase the computational scaling of CCD or DCD from N^6 to N^7. To seek a good balance between the computational cost and the accuracy, we include only up to effective 2-body operators arising from normal-ordering the 3-body operator. In this approximation, only the normal-ordered 3-body operator is excluded. We can justify this approximation by analogy to the HF approximation, which constructs a mean-field solution by including only the single and double contractions from the Coulomb operator. In cases where the mean-field approximation is reasonably good, the contribution of the missing normal-ordered Coulomb operator is small, compared to the single and double contractions. In contrast to the HF approximation, the parameters in the correlator in general allow a tuning of the strength of the missing normal-ordered 3-body operator, which we will discuss in detail in Sec. 12.2 when we apply the theory on the model system of 3D UEG.

In general, we can write our approximated Hamiltonian as

$$\begin{aligned}\hat{H}_{\mathrm{tc}} = \tilde{E}_{\mathrm{HF}} &+ \sum_{\sigma}\sum_{p} \tilde{\epsilon}_p \{a^\dagger_{p,\sigma} a_{p,\sigma}\} \\ &+ \frac{1}{2}\sum_{\sigma\sigma'}\sum_{pqrs} \tilde{V}^{rs}_{pq} \{a^\dagger_{p,\sigma} a^\dagger_{q,\sigma'} a_{s,\sigma'} a_{r,\sigma}\} \\ &+ E_{\mathrm{T}} + \sum_{\sigma}\sum_{p} \tilde{\omega}_p \{a^\dagger_{p,\sigma} a_{p,\sigma}\} \\ &+ \frac{1}{2}\sum_{\sigma\sigma'}\sum_{pqrs} \tilde{w}^{rs}_{pq} \{a^\dagger_{p,\sigma} a^\dagger_{q,\sigma'} a_{s,\sigma'} a_{r,\sigma}\},\end{aligned} \tag{9.5}$$

where E_T refers to the triply-contracted 3-body operator contribution, $\tilde{\omega}_p$ is the doubly-contracted 3-body integral and $\tilde{\omega}^{rs}_{pq}$ is the singly-contracted 3-body integral. The curly brackets indicate that the operators are normal-ordered with respect to the HF vacuum (Fermi sphere). We emphasize that in Eq. (9.5) the "HF" energy $\tilde{E}_{\mathrm{HF}}$ and "orbital energy" $\tilde{\epsilon}_p$ are calculated now with the modified 2-body integrals $\tilde{V}^{rs}_{pq} = w^{rs}_{pq} + V^{rs}_{pq}$.

9.4 Transcorrelated Coupled Cluster Framework

For clarity, we outline the procedures of our TC-CCD/DCD framework.

1. Evaluating ω^{rs}_{pq} and V^{rs}_{pq} and combining them into $\tilde{V}^{rs}_{pq} \leftarrow w^{rs}_{pq} + V^{rs}_{pq}$;
2. Calculating $\tilde{\epsilon}_p = \frac{\mathbf{k}_p^2}{2} + \sum_i (2\tilde{V}^{pi}_{pi} - \tilde{V}^{pi}_{ip})$;
3. Calculating $\tilde{E}_{\mathrm{HF}} = 2\sum_i^{N/2} \tilde{\epsilon}_i - \sum_{ij}(2\tilde{V}^{ij}_{ij} - \tilde{V}^{ij}_{ji})$ and E_{T};
4. Evaluating $\tilde{\omega}_p$, and defining $\epsilon_p \leftarrow \tilde{\epsilon}_p + \tilde{\omega}_p$;
5. Evaluating the singly-contracted 3-body integral $\tilde{w}^{rs}_{pq}$ and redefining $V^{rs}_{pq} \leftarrow \tilde{V}^{rs}_{pq} + \tilde{w}^{rs}_{pq}$;
6. Solving the usual CCD/DCD amplitude equations using ϵ_p and V^{rs}_{pq} for T_2 and obtaining E_{c};
7. The total energy is $E = \tilde{E}_{\mathrm{HF}} + E_{\mathrm{T}} + E_{\mathrm{c}}$.

We point out that the above outlined framework is general for any *ab initio* systems. In the case of 3D UEG, the detailed expressions for the singly-, doubly- and triply-contractions of the 3-body operator can be found in Sec. 12.5 when we study the model system in more details.

Part IV

Applications

In this part of the thesis, we focus on applications of the theories as discussed in the previous parts of the thesis on solid hydrogen at high pressures and the three dimensional uniform electron gas. The motivations for the studies on these two systems are summarised here.

Firstly, determining the phase diagram of solid hydrogen phases at extremely high pressures is a very challenging task experimentally, due to the light mass of the hydrogen atom and the extreme conditions required to obtain just a very small sample. On the other hand, the popular density functional theories fail to obtain accurate predictions of the phase diagrams, because of the high accuracy required to resolve the tiny energy differences between different solid hydrogen phases. Quantum chemical methods, most of which are systematically improvable, provide a reliable way to approach this hard problem. Of course, accurate quantum Monte Carlo method has been applied to study these systems before and improve to a large extend the agreement with experiments. However, the statistical noise makes it hard to tell precisely where the phase transitions happen. And it would be reassuring that the results obtained by quantum Monte Carlo can be confirmed by quantum chemical methods. Along with the techniques that improve the efficiency of coupled cluster in simulating solids, such as finite size corrections, we are at a good position to put our methods into test against the state-of-the-art diffusion Monte Carlo, by demonstrating that our methods are competitive in terms of efficiency and accuracy in studying these challenging systems. What's more, all previous studies rely on structures obtained by approximate density functional theories, which contain uncontrollable errors. This motives us to develop the nuclear forces based on perturbation theory, in order to optimize the structures used as models for different solid hydrogen phases.

Although we obtain good agreement between CCSD and DMC on most of the solid hydrogen phases, there is still one disagreement between the two theories on a metallic phase. Further theoretical developments are needed in order to resolve it. The possible sources of error from the coupled cluster side can be the not fully converged finite size errors or the insufficient accuracy in treating metallic systems with CCSD. To eliminate the possible residual finite size errors, one needs to simulate larger cells containing more electrons. To this end, methodologies that improve the efficiency of CCSD are desired. On the other hand, systematic and comparative studies on metallic systems using different methods are still missing in literature, possibly because of some theoretical difficulties. For example, in CCSD, one might not be able to get convergent energies due to the degeneracies in the single-particle energies; and

in fixed-node diffusion Monte Carlo, generally speaking, the fixed-node error is larger in metallic systems than in other systems and an efficient and systematic way to reduce this error is still missing. The combination of transcorrelation and coupled cluster theory is an attempt to address both the efficiency and accuracy problems as discussed in the canonical coupled cluster theory. We apply this combination scheme on 3D UEG with a wide range of densities, covering both weakly and strongly correlated regimes, to show the proof that it has the potential to be extended to the studies on real periodic solids with highly improved efficiency and accuracy.

Chapter 10

Studies of High Pressure Solid Hydrogen Phases at 0 K

The work in this chapter contains partly the work published in the paper titled "A Comparative Study Using State-of-the-art Electronic Structure Theories on Solid Hydrogen Phases under High Pressures", by Ke Liao, Xin-Zheng Li, Ali Alavi and Andreas Grüneis on npj Computational Materials, 5, 110 (2019). Ke Liao performed the calculations to produce the main results; Andreas Grüneis designed and led the research; Andreas Grüneis and Ke Liao wrote the paper; Xin-Zheng Li provided the crystal structures and Ali Alavi advised and provided the tools to perform the FCIQMC calculations.

10.1 Introduction

Hydrogen is the lightest and most abundant element in the Universe, yet its phase diagram at high pressures and low temperatures remains elusive. Due to the subtle interplay of quantum nuclear and electronic correlation effects [121, 122, 123, 124, 125, 126], the question as to which state of matter is stable at high pressures is controversial. Likely candidates for high pressure phases include various orientationally ordered molecular crystals [127, 128, 129, 130, 131, 132, 133], (liquid) metallic [134, 135, 136, 137, 138, 139, 140, 141, 142], superconducting [143] and superfluid systems [144]. These potentially exotic states of matter and their crucial importance for astrophysical, planetary as well as materials sciences has led to intensified investigations using both experimental and theoretical techniques. However, currently available calculated as well as measured equilibrium phase boundaries vary strongly with respect to the employed methods and suffer partly from uncontrolled sources of error.

Experiments that seek to determine properties of hydrogen under high pressures are hindered by various problems; for example, the low X-ray scattering

cross section of hydrogen, the small sample sizes and the diffusive nature of hydrogen. Recent claims of experimentally measured metallic phases [142, 145] are therefore under debate [146], while earlier experimental results [135, 147, 148] have not been able to conclusively detect metallic behaviour up to a pressure of 320-342 GPa.

Determining the Wigner-Huntington transition [134] using theoretical methods is extremely challenging. Despite the significant advancements of modern *ab initio* theories in the past decades, the predicted metallisation pressure varies significantly in a range of around 150 to 450 GPa depending on the employed method [149, 150, 137, 151, 124, 152]. Most *ab initio* studies of solid hydrogen are based either on DFT [149, 153, 137, 132] or quantum Monte Carlo calculations [154, 123, 155, 151, 122, 124, 152]. DFT is considered the workhorse method in computational materials science and can be used to calculate lattice enthalpies on the level of various approximate exchange and correlation (XC) energy functionals. Furthermore the Hellmann-Feynman theorem provides access to atomic forces and allows for optimizing structures as well as calculating phonons on the level of DFT [132]. Calculated and measured infrared and Raman spectra serve as a reliable tool for a direct comparison between theory and experiment [127, 128, 156, 129, 157, 133, 158, 159]. However, different parameterisations of the XC functional in DFT give inconsistent predictions, e.g. PBE predicts a too low metallisation pressure compared to experiments, while other exchange functionals produce higher pressures than DMC [155, 124, 160].

Instead, more accurate methods including DMC have been employed to predict more reliable pressure temperature phase diagrams [123, 151, 122, 124, 152], which correct the underestimation of the metallisation pressure by DFT-PBE to a large extent. However, DMC calculations rely on the fixed-node approximation and most of the current studies use crystal structures optimised using DFT. A critical assessment of the errors introduced by these approximations is still missing in literature and requires computationally efficient and concomitantly accurate methods.

In this chapter we show that quantum chemical wavefunction theories hold the promise to serve as an efficient and accurate tool for the investigation of high pressure phases of solid hydrogen. In particular, we find that coupled cluster theory [32, 33] achieves a good trade-off between computational cost and accuracy when employing recently developed techniques that allow for simulating the thermodynamic limit of periodic systems in an efficient manner [69, 70]. We note that these finite size corrections have paved the way for a number of *ab initio* studies including predictions of molecule–surface interactions [107, 70,

161, 162] and pressure-temperature phase diagrams of carbon and boron nitride allotropes [163]. The studies referred to above have demonstrated that coupled cluster methods achieve a similar level of accuracy as DMC for solid state systems that are not strongly correlated. Moreover coupled cluster methods have been benchmarked against various more accurate methods in model hydrogen systems [164], showing the high accuracy of the methods in weakly correlated situations. Furthermore we employ FCIQMC [58, 59, 91] in the present work for small systems to examine the validity of the coupled cluster method.

10.2 Results

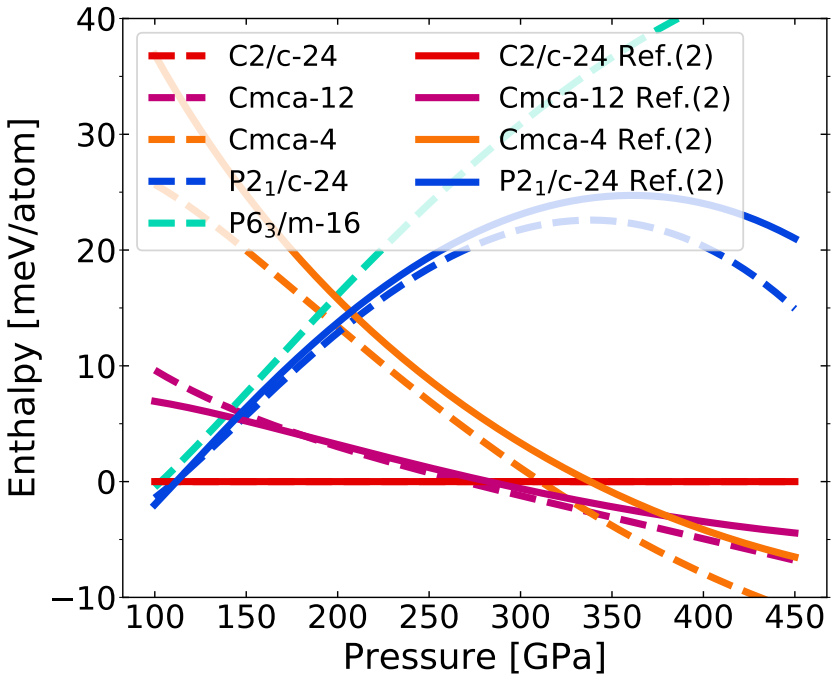

FIGURE 10.1: (Color online) DFT-PBE relative enthalpies. The DFT-PBE relative enthalpies of structures that are used for CCSD calculations in this work (dashed lines) and that of the structures from Ref. [122] (full lines). DFT favours the atomic phase Cmca-4 at high pressures.

We investigate theoretical results for the static lattice enthalpies of solid hydrogen phases computed on different levels of theory. The static lattice enthalpy is defined by

$$H = E + PV, \tag{10.1}$$

where P is the pressure estimated from the $E - V$ relation and V corresponds to the volume per atom. E refers to the total ground state energy per atom

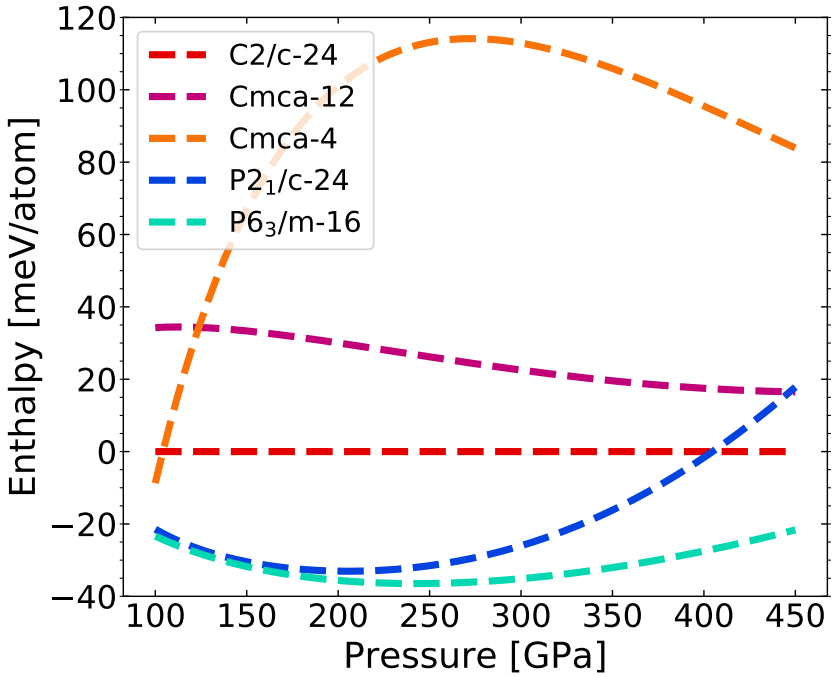

FIGURE 10.2: (Color online) HF relative enthalpies. The HF relative enthalpies of structures that are used in this work. In contrast to the DFT result, the atomic phase Cmca-4 is unfavoured at high pressures.

obtained using DFT, HF or CC theory in the Born-Oppenheimer approximation. In passing we note that the importance of quantum nuclear effects for transition pressures of solid hydrogen phases has been explored in Refs. [121, 122, 123, 124, 125, 125]. In the present work we will focus on the accuracy of the employed electronic structure theories only, disregarding such contributions. The CCSD energy is defined as the sum of the HF and the corresponding electronic correlation energy [33]. The pressure-volume relation of each phase, $P(V) = -\frac{\mathrm{d}E}{\mathrm{d}V}$, is obtained in the following manner. The total energy retrieved as a function of the volume per atom, $E(V)$, is fitted with a polynomial function of V^{-1} in an optimal order that minimises the fitting residual and provides smooth curves. We find that a third-order polynomial fitting is adequate for all phases except for phase P2$_1$/c-24 which is fitted using a fourth-order polynomial. A further increase in the fitting order can result in artificial wiggling behaviours of the $H(P)$ curves. The derivative with respect to the volume is readily obtained in an analytic manner using the fitted $E(V)$ function, yielding smooth $P(V)$ curves. We present all static lattice enthalpies relative to the C2/c-24 phase unless stated otherwise. In total, we study five solid hydrogen phases: Cmca-4 (Cmca-Low), Cmca-12, C2/c-24, P2$_1$/c-24 and P6$_3$/m-16, where we

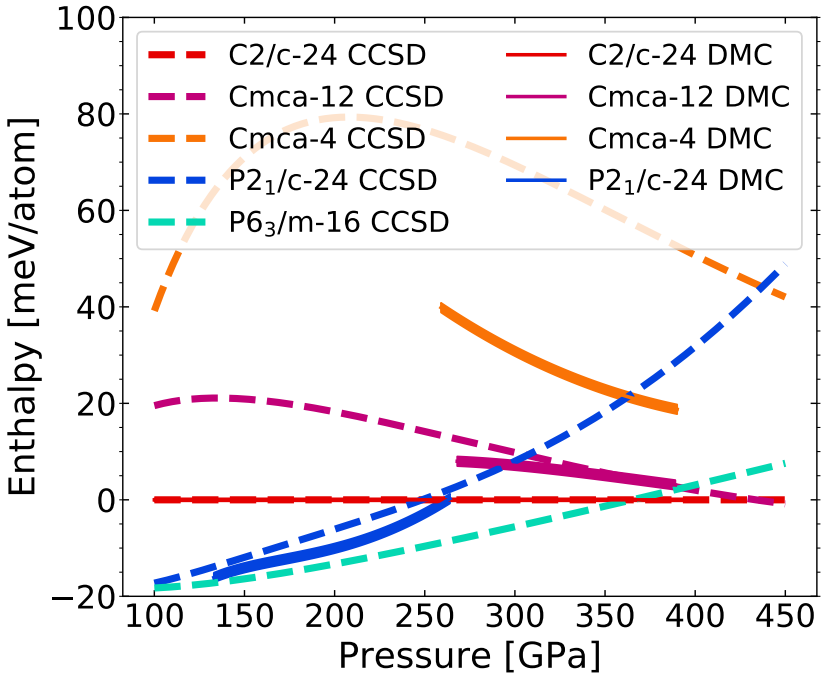

FIGURE 10.3: (Color online) CCSD relative enthalpies. The CCSD relative enthalpies of structures that are used in this work (dashed lines) and the DMC relative enthalpies of structures from Ref. [122] (full lines). The thickness of the full lines refer to the standard deviations of stochastic sampling of the 1st Brillouin zone while performing twist-averaging in the DMC calculations. In this work the 1st Brillouin zone is sampled using a dense regular grid such that the errors are converged to within 1 meV/atom. CCSD and DMC [122] agree very well in the most stable molecular phases, i.e. C2/c-24, P2$_1$/c-24 and Cmca-12, while the only discrepancy exists in the Cmca-4 phase, which is predicted by DFT-PBE to be metallic at high pressures. The phase transition between P6$_3$/m and C2/c-24 predicted by CCSD happens at approximately 350 GPa, which agrees reasonably well with the DMC transition pressure range 250-350 GPa from Ref. [123].

have adopted the convention of naming the structures by their symmetries followed by the number of atoms in the primitive cells. Phase Cmca-4, Cmca-12 and C2/c-24 consist of layered hydrogen molecules whose bonds lie within the plane of the layer, forming distorted hexagonal shapes. Whereas some bonds of hydrogen molecules in phase P6$_3$/m-16 lie perpendicularly to the plane of the layer. P2$_1$/c-24 consists of molecules arranged on a distorted hexagonal close-packed lattice.

These structures have previously been selected as potential candidates as the most stable high pressure phases of hydrogen [132] and have been studied by DMC methods. We notice that a family of 'mixed' structures are also identified

as promising candidates in Ref. [132], however, for the current comparative studies among CCSD, DFT-PBE and DMC, they are not included here but could be an interesting topic for future work.

We have optimized the geometries of the structures employing the DFT-PBE functional [165]. The DFT calculations have been performed using the Vienna *ab initio* simulation package (`VASP`) employing a plane wave basis set in the framework of the projector augmented wave method [82]. More details about the structures can be found in Ref. [132, 122].

We first discuss results of the investigated high pressure phases on the level of DFT. Figure 1 depicts the DFT-PBE static lattice enthalpies relative to the C2/c-24 phase. DFT-PBE predicts the C2/c-24 phase as the most stable phase at pressures ranging from about 100 GPa to 290 GPa. In a small range of pressures around 300 GPa the Cmca-12 phase is found to be thermodynamically stable, whereas the metallic Cmca-4 phase becomes stable at pressures exceeding approximately 330 GPa. Experimentally no metallic phases have been observed in this pressure range and quantum nuclear effects do not account for this discrepancy either [124]. The too low metallisation pressure can be attributed to the lacking of van der Waals interactions in PBE functional [160], resulting in underestimation of the stability in the molecular structures. We note that Figure 1 also depicts static lattice enthalpies from Ref. [122] obtained using DFT-PBE. We attribute the minor differences between the static lattice enthalpies to small differences in the employed structures and the fitting procedure that is employed to compute the lattice enthalpies from the total energies retrieved as a function of the volume per atom. We stress that the computed enthalpies are very sensitive to the employed structures.

In contrast to approximate XC functionals employed in DFT calculations, quantum chemical many-electron methods allow for approximating the electronic XC energy in a more systematic manner, albeit at significantly larger computational cost. The simplest wavefunction based method is the HF approximation that neglects electronic correlation effects by definition, employing a single Slater determinant as Ansatz for the electronic wavefunction. Figure 2 depicts the static lattice enthalpies computed in the HF approximation relative to C2/c-24. In contrast to DFT-PBE results, we find that HF theory significantly reduces the stability of the Cmca-4 and Cmca-12 phases, shifting their transition pressures far above 400 GPa. However, the HF method is not a good approximation for metallic systems despite the fact that it is free from self-interaction errors. In particular, HF band gaps are usually significantly

overestimated compared to experiment. Moreover, the lack of electronic correlation in the HF Ansatz leads to the neglect of van der Waals contributions that are crucial for a correct description of relative stabilities of molecular crystals [166]. We note that van der Waals contributions to the binding energy of molecular crystals become in general larger for smaller volumes due to the polynomial decay of the dispersion interaction with respect to the intermolecular distance. Due to the reasons outlined above, the static lattice enthalpies calculated on the level of HF theory are expected to exhibit significant errors compared to more accurate electronic structure theories and will serve as a reference for post-HF methods only.

Here, we employ the CCSD method to account for electronic correlation effects using a HF reference. Periodic CCSD theory results for the static lattice enthalpies relative to the C2/c-24 phase are shown in Figure 3. Compared to HF theory, CCSD stabilises the Cmca-4 phase by approximately 40 meV/atom at pressures above 300 GPa. Similarly, the relative static lattice enthalpy of Cmca-12 is lowered by about 20 meV/atom in CCSD compared to HF. For the $P2_1/c$-24 and $P6_3/m$-16 phases we observe an opposite effect of the CCSD correlation energy contribution, reducing their stability relative to C2/c-24 by approximately 30 meV/atom at pressures exceeding 250 GPa. We note that CCSD theory reduces the differences in the relative static lattice enthalpies of the considered phases compared to the HF approximation.

The CCSD energy is the sum of the HF energy and an approximation to the electronic correlation energy that is computed using an exponential Ansatz for the wavefunction. Due to the many-electron nature of the employed Ansatz, CCSD theory is exact for two-electron systems. The coupling between electron pairs is, however, approximated by truncating the many-body perturbation expansion in a computationally efficient manner and performing a resummation to infinite order of certain contributions only [33]. As a consequence, CCSD theory is expected to yield highly accurate results for the molecular hydrogen crystals. This is confirmed by comparing to the corresponding DMC results from Ref. [122] for C2/c-24 and $P2_1/c$-24 depicted in Figure 3 that agree very well with our CCSD findings. Furthermore static lattice enthalpies obtained on the level of CCSD and DMC (only shown in Ref. [122]) for Cmca-12 relative to C2/c-24 are in good agreement as well and the transition pressure between $P6_3/m$-16 and C2/c-24 by CCSD (≈ 350 GPa) and DMC ($\approx 250-350$ GPa only shown in Ref. [123]) are in reasonable agreement. However, we note that the DMC and CCSD results differ by about 40 meV/atom for the relative static lattice enthalpy of the Cmca-4 phase. In particular, the difference of the

static lattice enthalpies of Cmca-4 and C2/c-24 at 350 GPa are approximately 100 meV/atom, 60 meV/atom and 20 meV/atom using HF, CCSD and DMC, respectively.

10.3 Discussions

We now discuss possible reasons for the discrepancy between DMC and CCSD results for the Cmca-4 phase. DMC calculations employ the fixed-node approximation, whereas CCSD theory truncates the particle-hole excitation operator in the exponent of the wavefunction Ansatz. Fixed-node DMC gives the upper bounds [47] to the total energies of each phase. However it is not necessarily the case that the lower enthalpy difference between Cmca-4 and C2/c-24 predicted by DMC is more reliable than that by CCSD, since the fixed-node errors in each phase do not necessarily cancel out accurately. The fixed-node errors in the total DMC energy can be estimated using backflow transformations and by comparing to FCIQMC [58, 91] results for the uniform electron gas [167, 168]. It has been shown that the fixed-node errors are approximately 1 mHa per electron (27.2 meV/electron) in the high density regime. In the case of solid hydrogen, the authors of Ref. [155] report in their Supplemental Material that the energy in phase C2/c-24 is lowered by 1 mHa/atom (27.2 meV/atom) when employing backflow transformations and Ref. [123] reports that for Cmca-4 the backflow transformations lower the energy by only 10 meV/atom. This indicates that backflow transformations can depend significantly on the phases. Even though a large part of the fixed-node errors are expected to cancel when the energy difference between phases is computed, the remaining errors can still be on the scale of 10 meV/atom. On the other hand, we stress that the change from HF to CCSD relative static lattice enthalpies is on the scale of 40 meV/atom, indicating that a better approximation to the many-electron wavefunction than employed by CCSD theory could be necessary to achieve the required level of accuracy. We have also performed calculations using higher level theories, including FCIQMC, for smaller supercells containing 24 atoms at volumes corresponding to a DFT pressure of 400 GPa. These findings indicate that post-CCSD corrections to static lattice enthalpy differences for Cmca-4 and $P2_1/c$-24 are expected to be roughly 10 meV/atom. In short, both DMC and CCSD rely on good cancellations in errors introduced by their respective approximations to produce accurate predictions, especially when phases of different physical natures are compared. In addition to the inherent errors of DMC and CCSD theory, finite size and basis set errors can also be significant.

The latter only applies to CCSD calculations and has been checked carefully as outlined in the supplementary information. As regards the finite size error, we study supercells containing 96 atoms and employ twist averaging as well as structure factor interpolation methods for our CCSD calculations to achieve a level of precision that is comparable to DMC results. Despite the above considerations, we can currently not draw any firm conclusion about the reason for the discrepancy between DMC and CCSD results for Cmca-4. However, we note that recently developed basis set convergence acceleration techniques will enable future studies of bigger systems using CCSD [169] and FCIQMC [116] theory that can hopefully provide more insight.

Despite the discrepancy between CCSD and DMC findings for Cmca-4, we point out that the good agreement for the static lattice enthalpies of the most stable high-pressure hydrogen phases is encouraging. Achieving accurate thermodynamic limit results for such systems on the level of CCSD theory has only become possible recently due to the development of corresponding finite size corrections as outlined in Ref. [69, 70]. Furthermore we note that the computational cost of the corresponding CCSD calculations is still moderate compared to methods with a similar accuracy. A single CCSD ground state energy calculation for a system containing 96 atoms using 400 bands requires approximately 250 CPU hours, implying that it will become possible in the near future to perform structural relaxation of the employed crystal structures rather than relying on structures optimized using DFT-PBE. This is necessary for truly reliable predictions of high pressure phases of solid hydrogen.

We have presented static lattice enthalpies for high pressure phases of solid hydrogen calculated using state-of-the-art electronic structure methods including coupled cluster theory. We find that CCSD theory results agree well with DMC findings from Ref. [122]: phase C2/c-24 becomes more stable than phase $P2_1/c$-24 at around 250 GPa; phase Cmca-4 and Cmca-12 are less stable than phase C2/c-24 in the pressure range from 100 GPa to 400 GPa. The only discrepancy between CCSD and DMC is found for the Cmca-4 phase and we have discussed possible sources of error. Future work will include the effects of the nuclei motions which are crucial in making theoretical predictions comparable with experiments. Based on the presented findings, the required computational cost of the employed CCSD implementation and recent methodological advancements [169], we conclude that prospective CCSD studies will make it possible to optimise structures of solid hydrogen phases at high pressures with DMC accuracy. This will enable complementary CCSD and DMC studies with a significantly improved level of accuracy and achieve unprecedented physical insight

into the Wigner-Huntington transition of solid hydrogen.

10.4 Computational Details

The CCSD calculations have been performed employing the coupled cluster for solids (`CC4S`) code interfaced to the Vienna *ab initio* simulation package (`VASP`). The projector augmented wave method, as implemented in `VASP` [170, 171, 82], is used for all calculations. This section provides the details of the computational methods and convergence techniques employed in this work.

10.4.1 Geometries

The structures have been optimised using DFT-PBE and are similar to those employed in Ref. [132]. The forces on the atoms of the optimized structures are not larger than 0.1 eV/Å. With hindsight it would have been preferable to use exactly the same structures as published in Ref. [122]. However, for the purpose of the present work the agreement between the structures suffices. For the CCSD calculations we employ supercells containing up to 96 atoms that are as isotropic as possible and are obtained using the same method as described in the supplementary note 2 of Ref. [122]. In this manner finite size errors can be significantly reduced.

10.4.2 CCSD Basis Set Convergence

For the equilibrium phase boundaries in the pressure-temperature phase diagram only relative enthalpies are relevant. Therefore we have converged the energy differences with respect to the basis set only. MP2 natural orbitals (MP2NOs) [30] provide faster convergence than canonical Hartree-Fock orbitals (HFOs) computed from the full plane wave basis set. The convergence tests of the CCSD correlation energy differences with respect to the number of orbitals per atom relative to phase C2/c-24 have been carried out using supercells containing 24 atoms for all phases, except for phase $P6_3/m$-16 which contains 16 atoms in the supercells. We note that the basis set incompleteness errors are mainly due to the electronic cusp conditions, which are very local effects and are not dependent on the supercell size [172]. We first outline the procedure to obtain the basis set converged CCSD correlation energies. Prior to the correlation energy calculations, we compute the occupied HF orbitals using a Γ-point sampling of the first Brillouin zone (BZ) for each phase at different volumes. We use a plane wave basis set corresponding to a kinetic energy cutoff of 700 eV.

In addition, all occupied orbitals are constrained to be doubly occupied, avoiding fractional occupation numbers. This is achieved by utilising the `FERWE` and `ISMEAR` flags in `VASP`. We note that this could prevent the HF orbitals (HFOs) from converging to the energetically lowest possible solution. However, the CCSD method can largely compensate for this constraint.

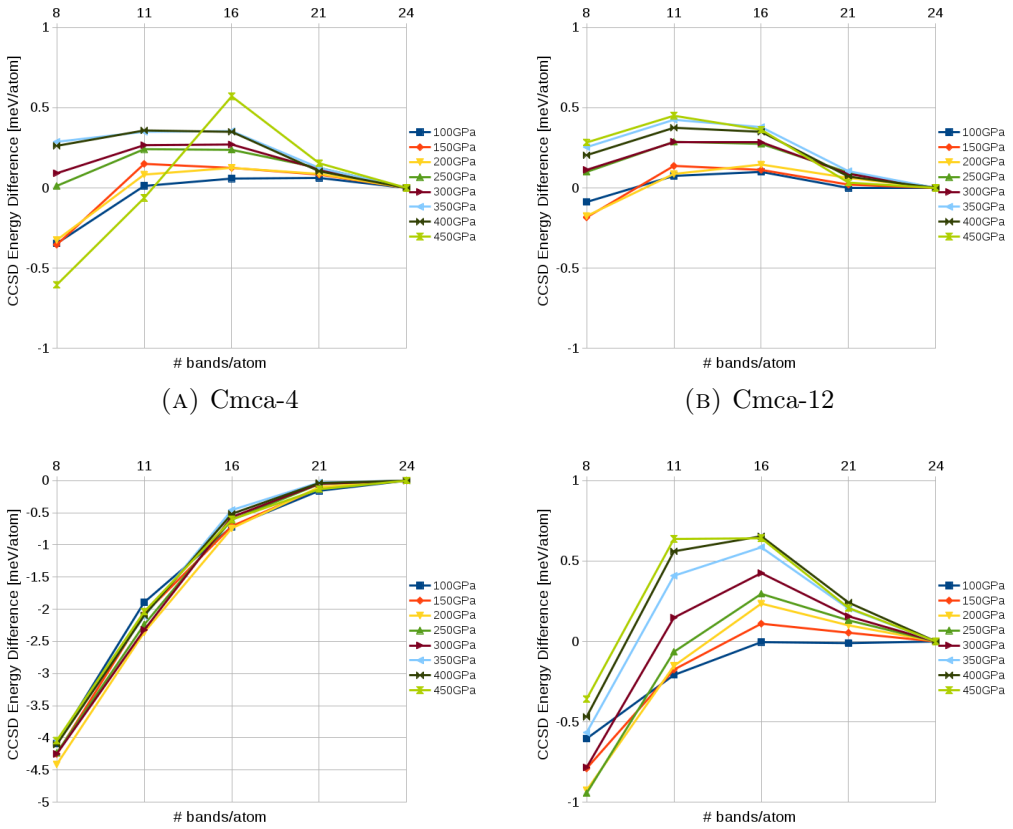

(A) Cmca-4 (B) Cmca-12

(C) $P2_1/c$-24 (D) $P6_3/m$-16

FIGURE 10.4: (Color online) CCSD correlation energy difference convergence with respect to the number of bands per atom. Fig. 10.4a shows that the correlation energy difference between phase Cmca-4 and C2/c-24 converges to within 1 meV/atom with 8 bands per atom (1 occupied HFOs + 7 MP2NOs) at all pressures and the same accuracy is achieved with 8 bands per atom in Fig. 10.4b and Fig. 10.4d for phase Cmca-12 and $P6_3/m$-16, respectively. Fig. 10.4c shows that the correlation energy difference between phase $P2_1/c$-24 and C2/c-24 converges to within 1 meV/atom with 16 bands per atom (1 occupied HFOs + 15 MP2NOs) at all pressures. 24-atom cells are used for phase Cmca-4, Cmca-12 and $P2_1/c$-24, while 16-atom cell is used for phase $P6_3/m$-16.

Following the HF ground state calculation, a full diagonalisation of the Fock operator is carried out in the space of all employed basis functions, whose dimension is equal to the number of plane waves. We further construct MP2NOs by

TABLE 10.1: Summary of the number of bands per atom required to reach 1 meV/atom accuracy in the relative CCSD correlation energy for each phase at all pressures and the number of atoms in the simulation cells employed for this convergence test.

Phases	C2/c-24	Cmca-4	Cmca-12	$P2_1/c$-24	$P6_3/m$-16
number of atoms in cell	24	24	24	24	16
number of bands per atom	/	8	8	16	8

diagonalising the virtual-virtual block of the one-body reduced density matrix in the HFO basis. As shown in Ref. [30], only a small fraction of the total MP2NOs can be used for the CCSD calculation without compromising the accuracy. We note that the Fock operator is not diagonal in the truncated MP2NO basis, thus it is necessary to recanonicalise in the subspace of the employed MP2NOs. The occupied HFO space is not affected by this procedure. In Fig. 10.4 we show the convergence of the correlation energies relative to phase C2/c-24 with respect to the number of natural orbitals per atom for Cmca-4, Cmca-12, $P2_1/c$-24 and $P6_3/m$-16. These calculations are carried out using the Γ-point sampling of the first BZ and the employed supercell sizes are summarised in Table 10.1. Compared to 24 bands/atom, we find that 8 bands/atom suffice to achieve a basis set convergence for the relative correlation energy to within 1 meV/atom, except for $P2_1/c$-24, where the remaining error is approximately 4 meV/atom. Based on these findings, we conclude that for the 96-atom supercell, 800 bands (48 occupied HFOs + 752 MP2NOs) should yield a converged correlation energy difference to within a precision of approximately 1 meV/atom for all phases except for phase $P2_1/c$-24. We stress that the CCSD correlation energy differences converge much faster than the CCSD correlation energies of each phase alone due to error cancellations. The plane wave basis set cutoff for the overlap integrals is set to 600 eV in this step.

We stress that HF energies and the correlation energies computed on the level of CCSD are converged to the complete basis set limit and the thermodynamic limit (TDL) separately using different schemes. We note that the total computational cost in obtaining the CCSD static enthalpy diagram is around 200 thousand CPU hours.

10.4.3 HF Finite Size Convergence

The HF energies are converged to within 1 meV/atom using increasingly large supercells or dense k-meshes sampling the first Brillouin zone.

TABLE 10.2: Effective system size used to converge the HF energy of each phase to within 1 meV/atom at all pressures. The effective system size is defined as the product of the number of sampled k-points in the first BZ and the number of atoms in the supercell.

	Cmca-4	Cmca-12	C2/c-24	$P2_1/c$-24	$P6_3/m$-16
Effective system size	4096	8232	5184	5184	8192

To obtain the converged Hartree–Fock energies per atom E^{HF} with respect to basis set, we use a kinetic energy cutoff for the plane wave basis of 700 eV. To be consistent with the HF step in the correlation energy calculations, we fix the occupancies in the manner described above. Moreover, sufficiently dense k-meshes are used to eliminate finite size errors. We use the effective system size, which is the product of the total number of k-points and the number of atoms in the supercell, as a measure of the system size. Table 10.2 summarises the employed system sizes used to reach an accuracy of 1 meV/atom for E^{HF}.

10.4.4 CCSD Finite Size Convergence

The twist-averaging technique [64] and finite size corrections [69, 70], based on the interpolation of the transition structure factor, are applied on 96-atom supercells to approximate the thermodynamic limit of the CCSD correlation energies.

For the CCSD calculations, only one k-point is used to sample the first BZ of the 96-atom supercells. However, the twist-average (TA) technique [64] and finite size correction scheme [69, 70] are used to reach the thermodynamic limit and minimize finite size errors. The TA procedure corrects mostly for the one-body contribution to the correlation energy and the latter retrieves mainly the missing two-body contribution to the correlation energy at large distances that exceed the size of the employed supercell. We denote the total two-body finite size error corrected (FS) CCSD correlation energy as E^{FS}. The total twist-averaged correlation energy (TA) can be expressed as

$$E^{\mathrm{TA+FS}} = \frac{1}{W}\sum_{i}^{N_t} E_i^{\mathrm{FS}} w_i, \tag{10.2}$$

where $N_t \approx 13$ is the total number of twists that are generated using the irreducible wedge of a $3\times3\times3$ k-mesh. w_i is the number of equivalent k-points to the ith irreducible k-point and $W = \sum_j^{N_t} w_j = 27$ is the total weight. Applying a twist means that the first BZ is sampled with a shifted k-vector $\Delta\mathbf{k}_i$. We have

checked the convergence with respect to the size of k-mesh used to generate the twists for Cmca-4 at 400 GPa. A $4\times4\times4$ k-mesh ($W = 64$) yields twist-averaged correlation energies that agree to within 1 meV/atom with the energies obtained using a $3\times3\times3$ k-mesh. We stress that TA accelerates convergence to the TDL mainly in small gapped systems. Therefore a single test on the Cmca-4 phase at high pressure ensures the convergence of the TA procedure with respect to the employed k-mesh in all other phases and pressures. We note in passing that 24 stochastic twists are used to sample the first BZ in Ref. [122] for carrying out TA. We stress that in CCSD theory, the total energy is partitioned into the mean field (HF) part and correlation energy part. Therefore relative fewer twists are needed for CCSD correlation energy calculations to reach convergence.

An acceleration scheme to reach the basis set convergence using MP2NOs is employed in conjunction with the twist-averaging technique: 400 bands (48 occupied HFOs + 352 MP2NOs) are used for each twist, and the basis set incomplete error is estimated as the energy difference between two calculations with 800 and 400 bands at the Γ-point,

$$\Delta E^{\mathrm{bse}} = E_0^{\mathrm{FS},800} - E_0^{\mathrm{FS},400}. \tag{10.3}$$

The justification is that the contribution of the high energy bands is independent of the positions of the sampled k-points. This procedure saves a large amount of computational resources.

The total CCSD energy per atom is expressed as

$$E = \frac{1}{N}(E^{\mathrm{c}}_{\mathrm{TA+FS}} + \Delta E^{\mathrm{bse}}) + E_{\mathrm{HF}}, \tag{10.4}$$

where $N = 96$ is the total number of atoms in the supercell used in the CCSD calculations.

10.4.5 Post-CCSD Error Estimates

We applied some higher level theories, including DCSD [35, 104], CCSD(T) [41, 33] and FCIQMC, to estimate the post-CCSD error.

CCSD yields accurate results for systems composed of weakly interacting electron pairs. For the present study it is important to determine if the considered solid hydrogen phases belong to this class of systems and what accuracy can be expected from CCSD. We now estimate the error of the CCSD correlation energies by using more accurate post-CCSD wavefunction based theories; *e.g.* DCSD [35, 104], CCSD(T) [41, 33] and FCIQMC. DCSD has been shown

in Refs. [35, 104] to achieve qualitatively good ground state energies even in the dissociation limit of hydrogen systems by ignoring exchange interactions between electron pairs. In the dissociation limit, CCSD is not expected to provide even qualitatively correct results. Thus DCSD is a valuable tool to determine whether CCSD works reliably at high pressures, where the inter-atomic distances become comparable to the inter-molecular distances, especially in the potential metallic phase Cmca-4 where CCSD and DMC show a discrepancy. We note in passing that due to the perturbative nature of CCSD(T), reliable results in the thermodynamic limit for metallic periodic systems can not be obtained [43]. However, CCSD(T) results in a finite supercell are meaningful. FCIQMC [58, 91] and its initiator approximation [59] can obtain the exact ground state solution to the non-relativistic Schrödinger equation in a give basis set.

DCSD, CCSD(T) and FCIQMC Using Γ-point

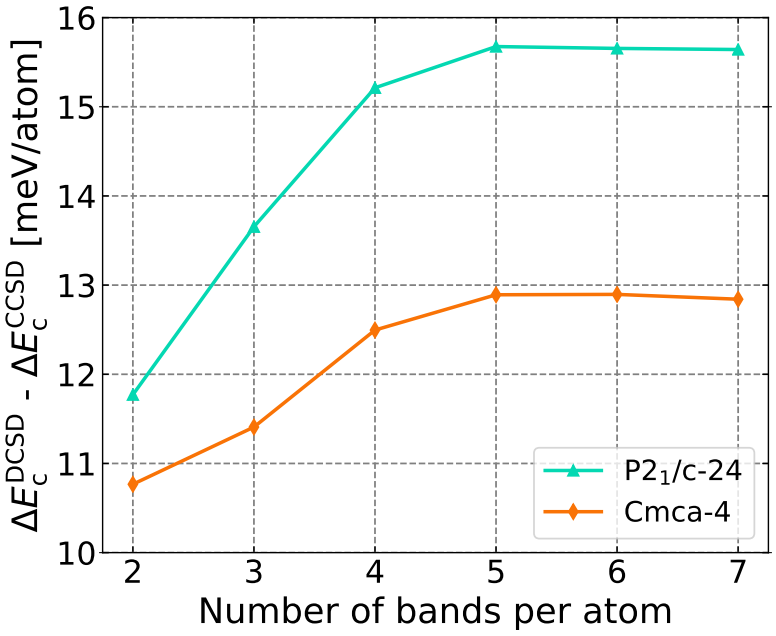

FIGURE 10.5: (Color online) Difference of relative correlation energies (relative to phase C2/c-24) between DCSD and CCSD with respect to the number of bands (occupied HFOs + MP2NOs) per atom. 24-atom cells at 400 GPa DFT pressure are used in all three phases.

We have performed calculations using DCSD, CCSD(T) and FCIQMC for phase C2/c-24, Cmca-4 and P2$_1$/c-24 at 400 GPa DFT pressure. Due to the

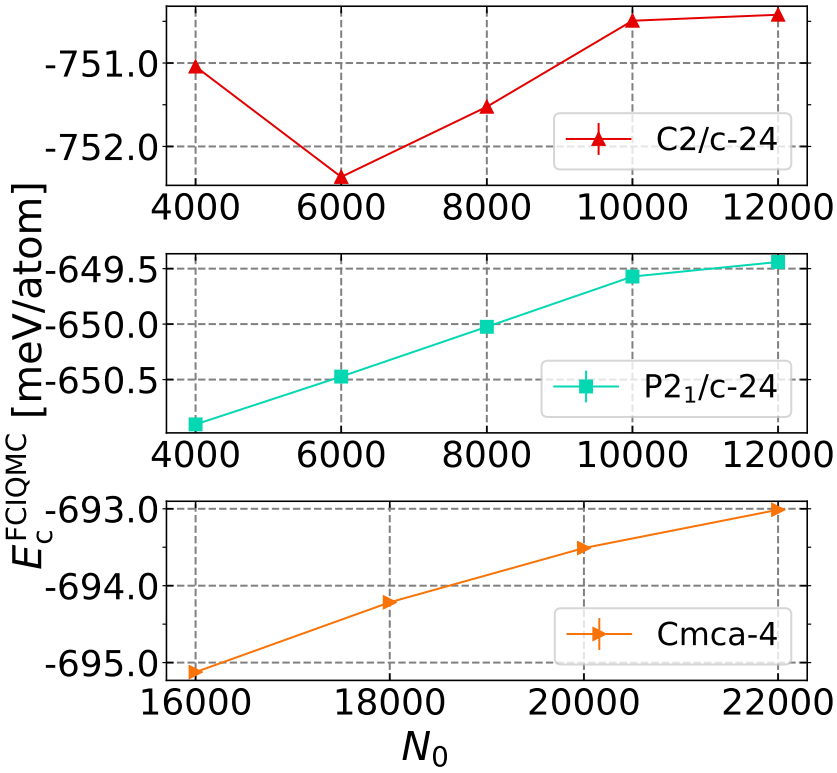

FIGURE 10.6: (Color online) *i*-FCIQMC correlation energy E_c^{FCIQMC} convergence with respect to the number of walkers on the HF determinant N_0. The statistical noise is smaller than the size of markers. 24-atom cells at 400 GPa DFT pressure are used and 60 bands (12 HFOs + 48 MP2NOs) are used for each phase.

unfavourable scaling of the computational complexity with system size, supercells that contain 24 atoms have been employed and the first BZs are sampled at the Γ-point only. Furthermore the computational cost of FCIQMC limits the number of MP2NOs. However, it is possible to obtain an error estimate of CCSD already using a very small basis set. As already shown in Fig. 10.4, CCSD correlation energies for various phases *relative to C2/c-24*, $\Delta E^{\text{c}}_{\text{CCSD}}$, converge rapidly with respect to the employed number of bands. Fig. 10.5 depicts the difference between $\Delta E^{\text{c}}_{\text{CCSD}}$ and $\Delta E^{\text{c}}_{\text{DCSD}}$, which corresponds to the *difference of the difference*, retrieved as a function of the number of bands per atom. We stress that the convergence of $\Delta E^{\text{c}}_{\text{CCSD}} - \Delta E^{\text{c}}_{\text{DCSD}}$ with respect to the number of bands is even faster than that of $\Delta E^{\text{c}}_{\text{CCSD}}$. Already 2 bands per atom are sufficient to converge the difference between CCSD and DCSD to within 4 meV/atom. For the comparative studies between CCSD, DCSD, CCSD(T) and initiator FCIQMC in the 24-atom supercells, we will therefore use only 60 bands.

The initiator FCIQMC correlation energies, $E^{\text{c}}_{\text{FCIQMC}}$, are converged to within

TABLE 10.3: Correlation energies obtained by CCSD, DCSD, CCSD(T) and *i*-FCIQMC on 24-atom cells for phase C2/c-24, $P2_1/c$ and Cmca-4 at DFT pressure 400 GPa using 60 bands (12 HFOs + 48 MP2NOs) in total. A small number of bands are used because of the limited computational resources. All energies in meV/atom.

	E_c C2/c-24	E_c $P2_1/c$	E_c Cmca-4	ΔE_c ($P2_1/c$ - C2/c-24)	ΔE_c (Cmca-4 - C2/c-24)
CCSD	-707.658	-627.121	-665.296	80.537	42.362
DCSD	-732.558	-640.325	-680.188	92.233	52.370
CCSD(T)	-742.638	-650.317	-684.629	92.321	58.009
i-FCIQMC	-750.42(1)	-649.44(0)	-693.01(3)	100.98(1)	57.40(8)

1 meV/atom with respect to the number of walkers on the HF determinant, N_0, using the recently developed auto-adaptive-shift method in the `NECI` code [173], which requires much fewer walkers to remove the initiator errors and converges to the exact ground state energy. The convergence of the correlation energies retrieved as a function of the number of walkers on the HF determinant for different phases are shown in Fig. 10.6.

Table 10.3 lists the correlation energies and their differences of phase C2/c-24, Cmca-4 and $P2_1/c$-24 using CCSD, DCSD, CCSD(T) and FCIQMC, respectively. We find differences in the correlation energies on the order of 10-20 meV/atom. We note that DCSD is closer to *i*-FCIQMC than CCSD and deviates by less than 10 meV/atom for the relative correlation energies. However, we stress that these error estimates are obtained sampling the Γ-point only. In the TA technique, we also have to account for correlation energy contributions from *k*-meshes centered at different *k*-points. In the following section we will assess the difference between CCSD and DCSD in the thermodynamic limit.

DCSD vs. CCSD in the Thermodynamic Limit

To estimate the difference between $\Delta E_c^{\mathrm{CCSD}}$ and $\Delta E_c^{\mathrm{DCSD}}$ in the thermodynamic limit, twist-averaging and finite size corrections for increasing supercell sizes are used. The convergence of the relative correlation energy differences between DCSD and CCSD retrieved as a function of the system size are shown in Fig. 10.7. We find that DCSD and CCSD agrees very well in the thermodynamic limit, which indicates that all considered phases at 400 GPa can be described accurately by CCSD theory. In the light of this and based on the deviation of DCSD from *i*-FCIQMC for the relative energies in the 24-atom cells, we estimate the post-CCSD corrections to be roughly 10 meV/atom.

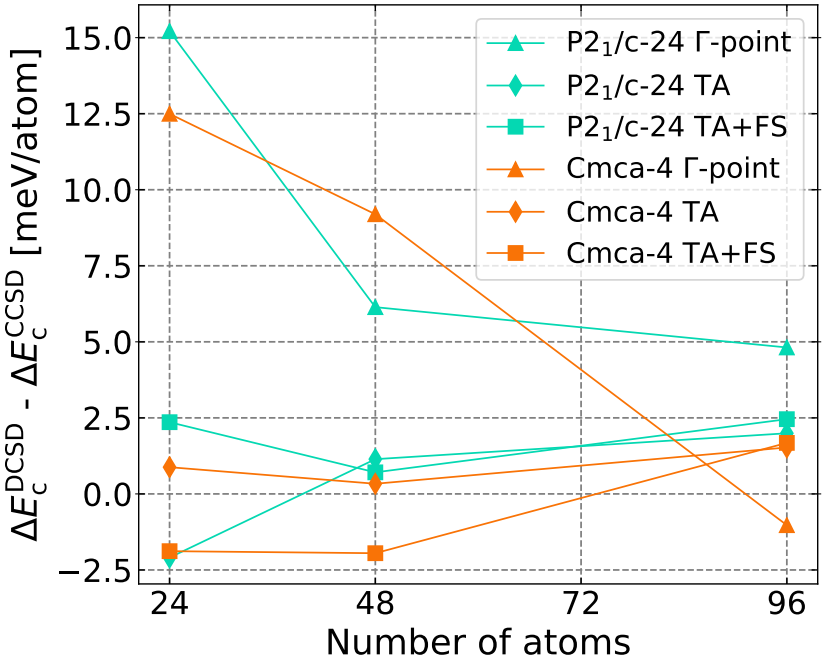

FIGURE 10.7: (Color online) Relative correlation energy difference between DCSD and CCSD with respect to system size employing Γ-point sampling of the first Brillouin zone (Γ-point), twist-averaging (TA) and twist-averaging plus finite size correction (TA+FS), respectively, for phase $P2_1/c$ and Cmca-4. Phase C2/c-24 is used as the reference. 200, 400 and 400 bands are used in total in 24-atom, 48-atom and 96-atom cells, respectively.

Chapter 11

Structural and Electronic Properties of High Pressure Solid Hydrogen

This chapter contains partly the work published in the paper titled "Structural and Electronic Properties of Solid Molecular Hydrogen from Many-electron Theories", by Ke Liao, Tong Shen, Xin-Zheng Li, Ali Alavi and Andreas Grüneis on Physical Review B, 103, 054111. Ke Liao implemented the MP2 forces algorithm, optimised the structures and carried out the calculations that contribute to the productions of the main results; Andreas Grüneis conceived and led this project, produced the figure of the band structures using DFT-PBE and MP2 structures, and calculated the G_0W_0 band gaps; Tong Shen carried out the calculations involving the electron-phonon interactions and the relevant figures; Ali Alavi and Xin-Zheng Li provided some theoretical support; all authors contributed to the writing of the paper.

11.1 Introduction

The seminal work of Wigner and Huntington – that first predicted a metallisation of hydrogen [134] in 1935 at a pressure of about 25 GPa – has sparked a continuous interest in the pressure-temperature phase diagram of hydrogen. However, state-of-the-art experiments [135, 147, 148] have not been able to conclusively detect metallic behaviour with the exception of some recent experimental studies [142, 145, 174] that are still under debate [146, 175]. Until today, one of the most reliable experimental estimates for the metallisation pressure range is approximately 425 GPa-450 GPa [174]. The lower value was obtained by the discontinuous pressure evolution in the infrared absorption, assuming a structural phase transition to the atomic structure, whereas the higher value was obtained by extrapolation of the band gap, assuming hydrogen remains in

phase III. Determining the metallisation pressure accurately is extremely challenging. This is partly reflected by the disagreement of the measured H_2 vibron frequency peaks as a function of the pressure, which is crucial for pressure calibration in many experiments [175]. In addition to the electronic structure, questions concerning the atomic structure are also difficult to address. Using X-ray scattering to determine the crystal structure experimentally is hampered by the low scattering cross section of hydrogen. Depending on pressure and temperature, hydrogen has been predicted to condense in different orientationally ordered molecular crystals [127, 128, 129, 130, 131, 132, 133] or (liquid) metallic [134, 135, 136, 137, 138, 139, 140, 141, 142] phases.

Accurate theoretical predictions of the equilibrium phase boundaries and other properties of high pressure hydrogen require an appropriate treatment of quantum nuclear and many-electron correlation effects [121, 122, 123, 124, 125, 126], which can only be achieved using state-of-the-art *ab initio* methods. Hitherto, most *ab initio* studies of solid hydrogen are based either on DFT [149, 153, 137, 132] or quantum Monte Carlo calculations [154, 123, 155, 151, 122, 160, 124]. DFT employing approximate exchange and correlation (XC) energy functionals can be applied to compute infrared and Raman spectra as well as equilibrium phase boundaries, facilitating a direct comparison between theory and experiment [127, 129, 157, 128, 156, 133, 158, 159]. However, different parameterisations of the XC functional in DFT yield inconsistent predictions [160, 155, 124]. Diffusion Monte Carlo (DMC) produces more reliable pressure temperature phase diagrams [123, 151, 122, 152, 124]. Furthermore DMC can also be used to compute quasiparticle gaps including nuclear quantum effects [176]. Recently we have shown that CCSD theory predicts static lattice enthalpies of solid hydrogen phases with high accuracy and computational efficiency [93]. CCSD results for the most stable model phases including phase II and III are in good agreement with those obtained using diffusion Monte Carlo.

11.2 Results

11.2.1 Structural Optimisation Employing MP2 Forces

We fully relax the internal degrees of freedom of DFT-PBE structures by minimizing the atomic forces computed on the level of MP2 theory, while keeping the lattice vectors fixed and maintaining the space group symmetry. For the purpose of the following discussion we will focus on the shortest hydrogen bond length in these structures, which represents the most striking difference between

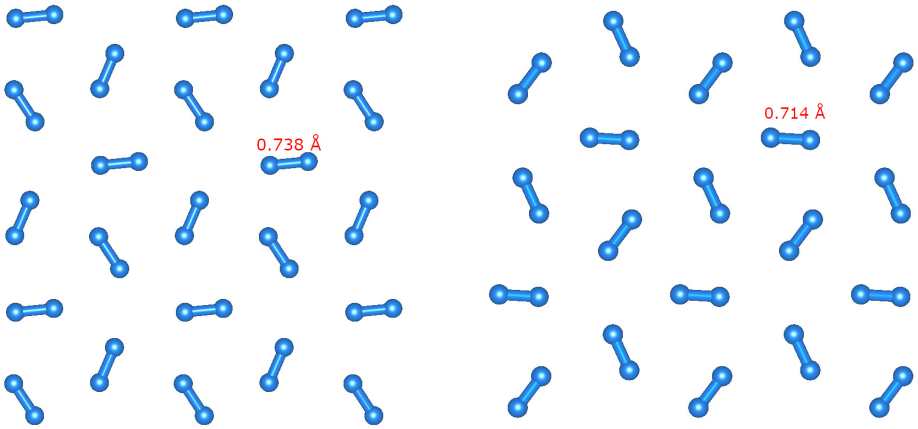

FIGURE 11.1: Structures optimized by (A) DFT-PBE and (B) MP2 forces at DFT-PBE pressure of 100 GPa. The main difference between the two structures lies in the bond length. For DFT-PBE, it is ≈ 0.74 Å whereas for MP2, it is ≈ 0.71 Å.

MP2 and DFT-PBE results. As shown in Fig. 11.1, at a pressure of 100 GPa, the shortest hydrogen molecule bond length in the DFT-PBE structures for phase III is ≈ 0.74 Å whereas MP2 theory predicts it to be ≈ 0.71 Å. Similar findings apply to the structures at other pressures. In passing we note that the shortest hydrogen molecule bond length obtained using the vdW-DF functional [177] is 0.72 Å, which is fortuitously close to our MP2 findings and agrees with findings reported in Ref. [124]. However, it is important to assess the reliability of these newly optimised structures further by comparing to CCSD results. Fig. 11.2 illustrates that the total MP2 energy per atom of phase III at a volume of 1.57 Å^3/atom (corresponding to a DFT-PBE pressure of 250 GPa) is lowered by about 5 meV/atom during the structural relaxation. The initial 11 steps of the relaxation were carried out using a 72-atom supercell only, whereas all further optimisation steps have been performed using a 96-atom supercell, indicating that finite size effects become negligible. The shortest bond length is only changed by about 0.01 Å betweeen the 11th and the final step. After 14 steps the remaining forces on the atoms are smaller than 0.05 eV/Å. Fig. 11.2 also depicts that the CCSD energy is lowered in total by 11 meV/atom during the full MP2 relaxation trajectory, which is similar to the change in MP2 theory. The latter observation is important because it demonstrates that MP2 and CCSD equilibrium structures are expected to deviate only slightly. This justifies the main assumption of the present work which states that MP2 structures for phase III are very accurate. To further substantiate this claim, we note that MP2 theory predicts lattice constants for a wide range of solids with significantly

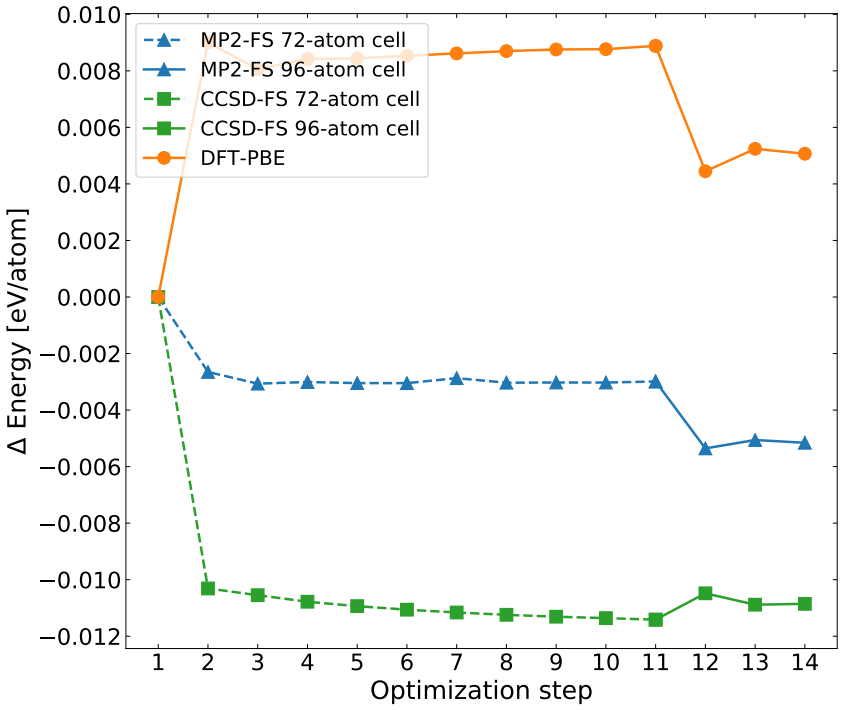

FIGURE 11.2: The energy changes during the structural relaxation as a function of the optimisation steps. This example at the DFT pressure of 250 GPa shows that the MP2 and CCSD total energies per atom are lowered in a similar fashion and provides evidence that the optimised MP2 structures are close to the CCSD structures. The MP2 and CCSD energies are corrected by finite-size corrections [70] and are labelled by MP2-FS and CCSD-FS, respectively,

higher accuracy than DFT-PBE when compared to experiment [178].

11.2.2 DFT-PBE Band Structures

As a first demonstration for the far-reaching consequences of the structural changes, we discuss its impact on the quasiparticle band gap of model phase III (C2/c-24). Fig. 11.3 depicts the electronic band structure for phase III at a pressure of 250 GPa employing the atomic structures optimised using DFT-PBE and MP2 theory. The Kohn-Sham band structures are computed using the PBE functional, exhibiting an indirect band gap with the valence band maximum at X and the conduction band minimum at L. The direct gap is located at Γ. The direct and indirect PBE band gaps for the MP2 structure are 2.97 eV and 1.9 eV, respectively. However, due to the reduced hydrogen bond length, the direct and indirect band gaps are about 1 eV larger in the MP2 structure compared to the DFT-PBE structure.

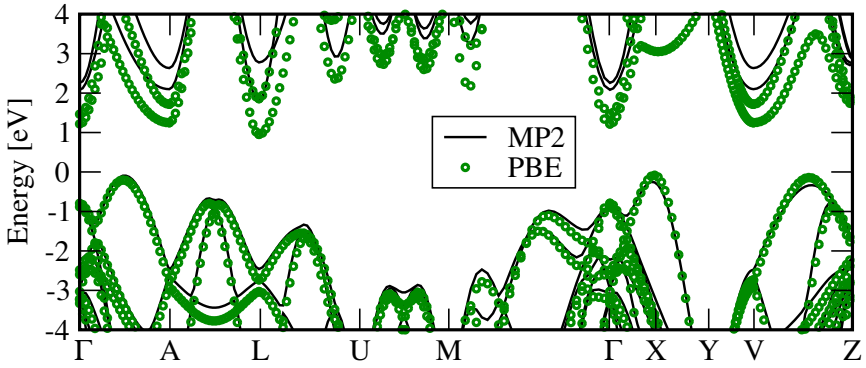

FIGURE 11.3: Electronic band structure of model phase III (C2/c-24) obtained using DFT-PBE. Black (green) lines correspond to MP2 (DFT-PBE) equilibrium geometries at the pressure of 250 GPa.

11.2.3 G_0W_0 Band Gaps of the Static Crystal

We note that this increase in the band gap persists for the more accurate quasiparticle band gaps computed on the level of the G_0W_0 approximation, see Fig. 11.4. We stress that due to the strong dependence of the electronic gap on the pressure, an underestimation of the band gap by 1 eV results in a decrease in the predicted metallisation pressure by more than 50 GPa. We note that the previously employed vdW-DF structures in Refs. [124, 176] yield band gaps that agree with our findings obtained using the MP2 structures to within about 0.1 eV. The direct and indirected PBE band gaps computed using the vdW-DF structures are 2.88 eV and 1.74 eV, respectively.

11.2.4 Renormalised G_0W_0 Band Gaps by Electron-phonon Interactions

We now turn to the comparison between the computed G_0W_0 band gaps and experimental findings. As shown in Ref. [176], the inclusion of zero point vibrational effects to the quasiparticle gaps is crucial. At 0 K, this is termed as zero-point renormalisation (ZPR). At finite Ts, T-dependent band gap renormalisation also exists, originating from the Fan and Debye-Waller terms as described in the dynamical HAC theory. More details can be found in Ref. [179, 76]. Unfortunately a seamless inclusion of the electron-phonon coupling contributions to the band gap on the level of MP2 theory would be computationally too expensive at the moment. Therefore we estimate these renormalisations using DFT-PBE phonons and include them in the G_0W_0 quasiparticle band gaps. Our calculations yield a ZPR of the direct and indirect gap of about -1 eV,

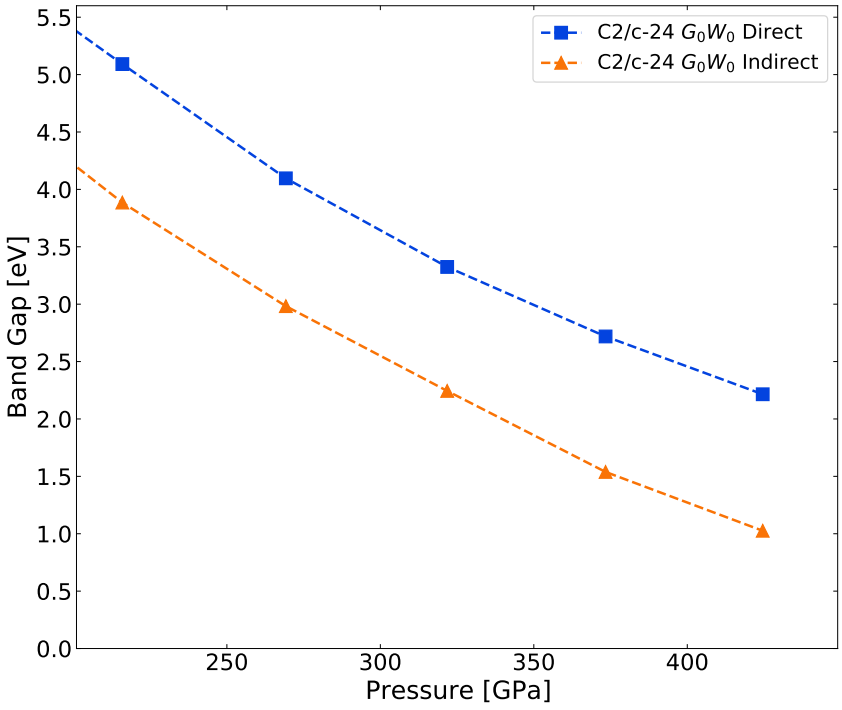

FIGURE 11.4: Pressure dependence of the direct and indirect G_0W_0 band gaps of the ideal C2/c-24 crystal optimised by MP2 forces.

which is by coincidence a similar magnitude as the band gap increase caused by structural relaxation but significantly smaller in magnitude than the -2 eV ZPR reported previously [176].

The computed G_0W_0 gaps with EPIs are depicted in Fig. 11.5 for a range of pressures alongside experimental findings[148, 174, 133, 176]. We note that the direct G_0W_0 gaps includes ≈-0.12 eV exciton binding energy in order to enable a direct comparison to the optical measurements from Ref. [148, 174]. Furthermore we plot the G_0W_0 gaps with respect to the CCSD pressures computed from the enthalpy versus volume curves, enabling an accurate and direct comparison to experimental findings. Compared to experiments the direct and indirect quasiparticle band gaps are overestimated when our EPI values are used. Replacing our EPI contribution with the estimate by Gorelov *et. al.* (≈-2 eV) yields underestimated band gaps compared to experiment. From the relatively large difference between the EPI contributions computed in this work and Ref. [176], we conclude that this contribution is the remaining leading order error in our study. However, the experimental metallisation pressure of about 450 GPa lies within our theoretical uncertainties. In a recent work by Monacelli *et. al.* [180], quantum nuclear effects are included in a nonperturbative

way, which shows a reduction of the band gaps by approximately 3 eV. Their metallisation pressure agrees well with experiment. Their structures, however, are optimised on the level of DFT using the BLYP exchange-correlation functional. Another study on the band gap that achieves very good agreement with experiment was carried out by Dogan *et. al.* [181] using DFT-PBE optimised and static crystal structures. From the above analysis, we expect that this good agreement is probably the result of fortuitous error cancellation due to the two compensating effects: (i) the underestimation of the band gap by using the DFT-PBE structures and (ii) not taking into account EPIs which reduce the band gap.

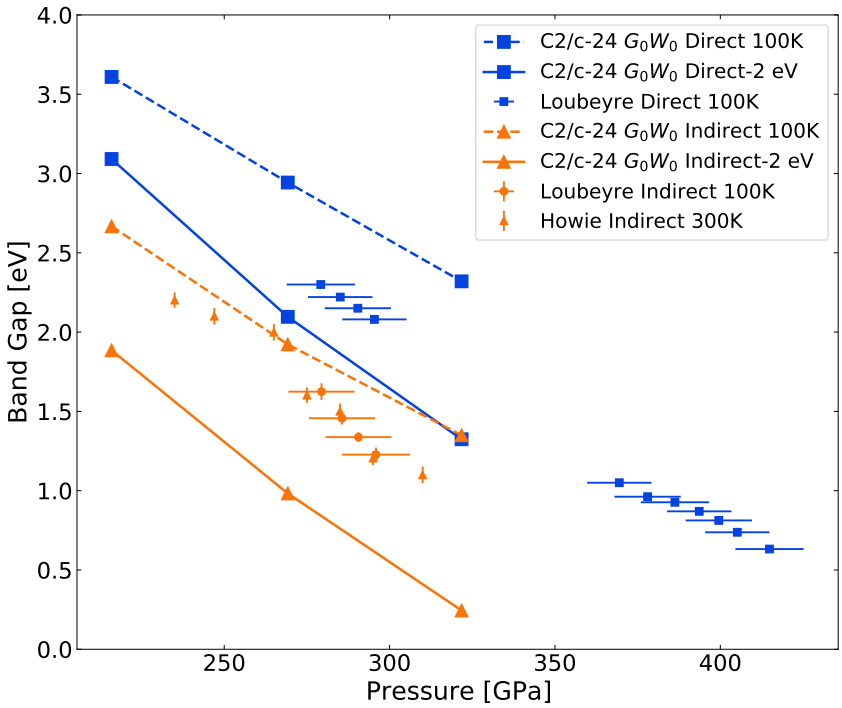

FIGURE 11.5: Pressure dependence of the direct and indirect G_0W_0 band gaps including EPI contributions from this work (dashed lines) and ≈ -2 eV EPI contributions from Ref. [176] (full lines). The direct G_0W_0 band gaps include ≈-0.12 eV exciton binding energy. The experimental estimates have been taken from Ref. [148, 174, 133, 176].

11.2.5 T-dependent Direct and Indirect Band Gap Renormalisations

The difference of the T-dependent indirect band gap renormalisations in Ref. [176] between 200 K and 300 K is about 0.2 eV, which is an order of magnitude larger

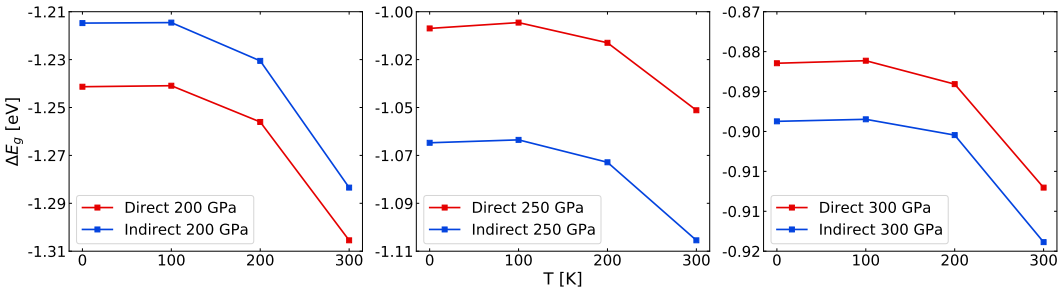

FIGURE 11.6: T-dependent renormalisations due to EPIs on the direct and indirect band gaps of model phase III (C2/c-24) obtained using DFT-PBE at 200, 250 and 300GPa, calculated using dynamical HAC theory. 100 random q-points, 300 electronic bands and a $4 \times 4 \times 4$ k-mesh are used.

than our estimate of 0.02 eV, see Fig. 11.6. The difference in the experimental indirect band gaps between 100 K [148] and 300 K [133] is about 0.02 eV, which agrees much better with our result. These discrepancies signal that further careful examinations of the employed structures in different studies and the treatment of different contributions are needed.

11.2.6 Pressure Dependence of H_2 Vibron Frequencies

For a deeper understanding of the comparison with experiments, we also assess the reliability of the experimental pressure calibration. This is done by analyzing the dependence of the H_2 vibron peak frequency as a function of the pressure. As pointed out in Refs. [182, 175, 174] and depicted in Fig. 11.7, the currently available experimental estimates for the H_2 vibron peak frequency vary significantly at high pressures, questioning the reliability of experimentally determined pressures. Possible reasons for the experimental uncertainties are summarised in Ref. [175]. However, theoretical estimates of the vibron peak frequency with respect to pressure also vary significantly with respect to the employed XC parametrisation on the level of DFT [124, 174]. We have estimated the vibrational frequency for the MP2 structures by computing the MP2 and CCSD energies as a function of H_2 bond lengths around the equilibrium. Molecular orientations, locations of the centers of mass and volumes are fixed while changing the bond lengths in accordance with Ref. [124]. The change of the harmonic frequency with respect to the pressure can be used as a reliable calibration for pressures depicted in Fig. 11.7. We find that both the MP2 and CCSD frequencies have a similar slope as the H_2 vibron frequency peak measured by Loubeyre *et. al.* in Ref. [174, 183]. From this we conclude that the

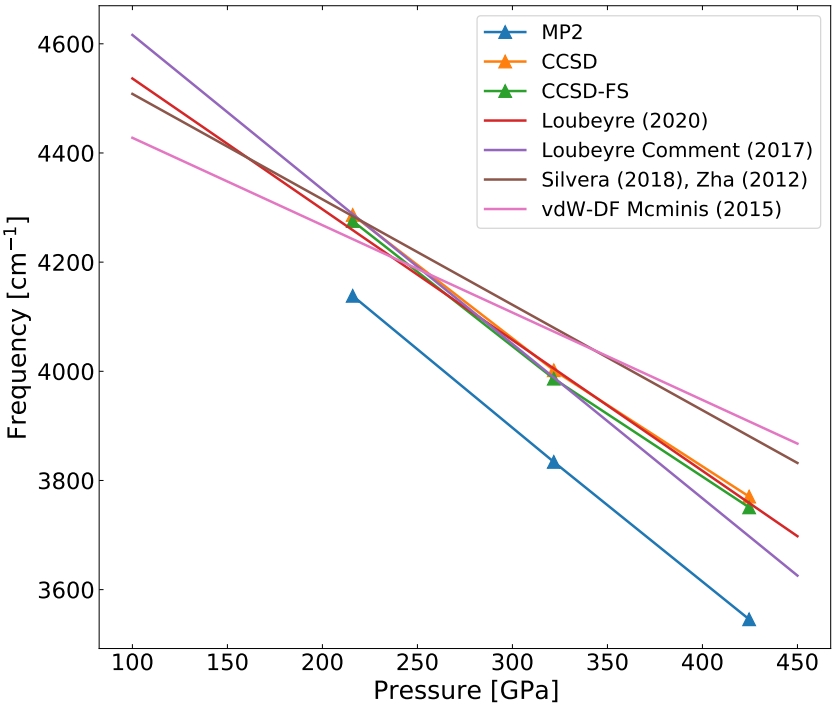

FIGURE 11.7: Experimentally measured and theoretically calculated H_2 vibron peak frequencies as a function of pressures. The approximate vdW-DF (taken from the Supplemental Material of Ref. [124]), MP2 and CCSD harmonic frequencies are shown by the pink, blue and green solid lines, respectively. The brown solid line shows the experimentally measured relation between the H_2 vibron frequencies and pressures from Silvera (2018) [182] and Zha (2012) [157]. Another two experimental data lines are from Loubeyre (2020) [174] (red) and Loubeyre (2017) [183] (purple).

experimental band gaps depicted Fig. 11.5 correspond to pressures that are in good agreement with our most accurate estimates. In passing we note that despite the good agreement of vdW-DF structures with our MP2 structures, vdW-DF vibrational frequencies are in better agreement with experimental results of Ref. [182, 157]. However, we argue that this agreement is most likely fortuitous, because both MP2 and the more accurate CCSD vibrational frequencies exhibit a very similar and steeper slope with respect to pressure. From the above findings, we conclude that the vibrational frequencies of high pressure hydrogen phases are very sensitive to the structural parameters and the corresponding electronic structure method. This has potential implications for estimates of the zero point motion energy contribution to the lattice enthalpies of accurate *ab initio* calculations of transition pressures [122]. Having established the good agreement between our pressure estimates and those reported in Ref. [174], we

can also comment on the observed evidence of a phase transition at 425 GPa. As predicted by both DMC and CCSD calculations [122, 124, 93] at low temperature, phase III (C2/c-24) transforms into Cmca-12 at this pressure. However, these calculations have been performed using DFT optimised structures. We have investigated the lowering of static lattice enthalpies resulting from MP2 lattice relaxations for both structures at a selected volume corresponding to the DFT pressure of 450 GPa, finding that changes to the previously calculated transition pressures are negligible. This is surprising given the relatively large changes to the H_2 bond lengths.

11.3 Discussions

Our work demonstrates the strengths and weaknesses of widely-used approximate DFT methods for simulating high pressure phases of hydrogen by comparing to more accurate results obtained using many-electron methods including coupled cluster theory. Although approximate DFT is a computationally efficient tool for performing random structure searches [132], further structural optimisation is required to achieve good agreement of band gaps and vibrational frequencies with experimental findings in solid hydrogen. Here, we demonstrate that periodic many-electron perturbation theory calculations using plane wave basis sets have become increasingly efficient in previous years [70, 93], making such optimisations feasible for systems with an increasing number of atoms. Our findings show that compared to MP2 theory, DFT-PBE structures exhibit too large hydrogen bond lengths causing too small band gaps. Although vdW-DF calculations predict structures that are closer to MP2 theory, vibrational frequencies that agree with experiment for a wide range of pressures can only be obtained on the level of CCSD. Furthermore we have demonstrated that the remaining leading order error of *ab initio* band gaps in solid hydrogen crystals is likely to originate from approximations used to estimate the EPI contributions. Nevertheless, it is worth pointing out that T-dependent fundamental band gap renormalisation based on DFT-PBE structure is in better agreement with the experimental data. Combining accurate benchmark results with hybrid or non-local XC functionals using adjustable parameters could be useful for materials modeling in this case. Alternatively, machine-learning from MP2 forces or even more accurate *ab initio* data could be used to produce accurate potential energy surfaces and corresponding vibrational entropy contributions. Future work will focus on a seamless integration of electron-phonon interaction

on the level of many-electron theories to further improve the accuracy of such *ab initio* simulations.

11.4 Computational Details

We optimise the atomic structure of model phase III using nuclear gradients calculated on the level of MP2 theory and a plane wave basis set. We note there are some earlier implementions of MP2 forces in periodic solids using Gaussian basis set [77, 78, 79]. All periodic calculations have been performed using the Vienna *ab initio* simulation package (`VASP`) [82] in the framework of the projector augmented wave method [81, 80], interfaced to our coupled cluster code [184] that employs an automated tensor contraction framework (`CTF`) [83]. We use Hartree–Fock orbitals in all post Hartree–Fock methods [30]. Although MP2 theory can be considered a low-order approximation to CCSD theory, it predicts lattice constants for a wide range of solids with higher accuracy than DFT-PBE when compared to experiment [178]. Due to the many-electron nature of the employed Ansatz, CCSD theory is exact for two-electron systems. The coupling between electron pairs is, however, approximated by truncating the many-body perturbation expansion in a computationally efficient manner and performing a resummation to infinite order of certain contributions only.

Phase III is modelled by C2/c-24 crystals [132] initially predicted by *ab initio* simulations and random structure searches [132, 122]. The structure is labelled by its symmetry followed by the number of atoms in the primitive cell. C2/c-24 consists of layered hydrogen molecules whose bonds lie within the plane of the layer, forming a distorted hexagonal shape. We note that previous DMC studies employed structures that have been optimised using a range of approximate density functionals, indicating that an appropriate choice is crucial [124]. In this work we employ supercells containing up to 96 atoms for the relaxation of the atomic positions. The convergence with respect to computational parameters such as number of virtual orbitals, k-meshes for the Hartree–Fock energy contribution and energy cut offs for the employed plane wave basis set have been checked carefully in the following subsections.

Beyond the static lattice model, the T-dependent band gap renormalisation of the single particle excitation energy due to electron-phonon interactions (EPIs) was also studied, using a dynamical extension of the static EPIs theory originally proposed by Heine, Allen, and Cardona (HAC) [185, 72]. The quasiparticle approximation (QPA) was used to correct the DFT-PBE eigenvalues based on the EPIs self-energies. These calculations are performed using

QUANTUM ESPRESSO (QE) [186] and YAMBO [187, 179, 188]. The excitonic effects were obtained by solving the Bethe-Salpeter equation (BSE), as implemented in VASP. The EPIs and the excitonic effects are calculated using DFT-PBE optimised primitive cell structure. Those effects are detailed in the following corresponding subsections.

11.4.1 HF and MP2 Forces' Convergence with Respect to Plane Wave Basis Energy Cutoff

The HF forces are calculated using the PAW pseudopotential with an energy cutoff of 400 eV. A test using a 500 eV cutoff shows that the maximum error in the HF forces is 0.029 eV/Å. The energy cutoffs used for the orbital plane wave basis and the auxiliary plane wave basis (used for computing Coulomb integrals) are both set to 600 eV in the MP2 part. A test carried out at 300 GPa for phase C2/c-24 using 800 eV for the energy cutoffs shows that the MP2 forces are converged to an accuracy of 0.01 eV/Å.

11.4.2 MP2 Forces' Convergence with Respect to Number of Bands

At 300 GPa, we have tested the convergence of the MP2 forces with respect to the number of bands, using 8, 9, 10 and 11 bands per atom to show that the maximum errors in the forces are well converged to 0.003 eV/Å, see figure (11.8).

11.4.3 Structural Convergence with Respect to Employed Supercell Size

The structure optimisations are carried out in two stages. The first stage (about 10 optimisation steps) uses computationally less expensive settings, whereas the second and final stage (remaining optimisation steps) employs increased supercell sizes and k-mesh densities to achieve a high numerical precision of the final relaxed geometries. In the first stage we compute the HF contribution to the gradients employing 4x4x4 k-meshes and 24-atom primitive cells. The MP2 gradient contribtions are obtained by sampling only the Γ-point in the first Brillouin zone of the 72-atom supercell. In the final stage, the HF gradients are computed using a $6 \times 6 \times 6$ k-mesh, whereas the MP2 contributions are computed using 96-atom supercells with all other parameters unchanged. A further increase in the size of the k-mesh or the supercell size is not expected to change the final results.

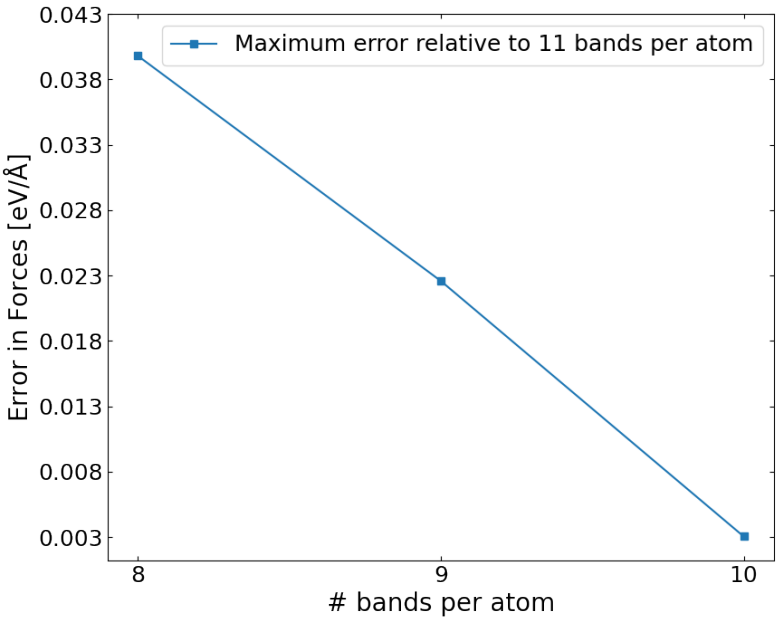

FIGURE 11.8: The maximum error in forces relative to using 11 bands per atom as a function of number of bands.

11.4.4 Effects of Relaxing the Cell Shape

Relaxing the cell shapes on the MP2 level would require the calculation of the stress tensor, which at the current stage is not implemented. However, the effects of relaxing the cell parameters can be estimated using the HF forces and stress tensors. To this end, we first relax the internal degrees of freedom of the PBE structures while keeping the cell parameters fixed; on the second stage, we also allow the latter to change. By observing how the HF energy is further lowered during the second stage, we can estimate the impact of the relaxed cell shape.

The above procedure is carried out on the DFT-PBE C2/c-24 structure at 300 GPa, using a $5\times5\times5$ k-mesh sampling the 1st BZ and an energy cutoff of 400 eV along with PAW potential. Figure (11.9) shows that between the first and second stage, the HF energy is lowered by 1.1 meV in total (0.047 meV/atom) only, demonstrating that further effects resulting from the relaxation of the lattice vectors can be disregarded.

11.4.5 Electron-phonon Interactions

Electron-phonon interactions (EPIs) were considered by combining `QUANTUM ESPRESSO` (`QE`) [186] and `YAMBO` [179]. In the `QE` calculations, the DFT ground

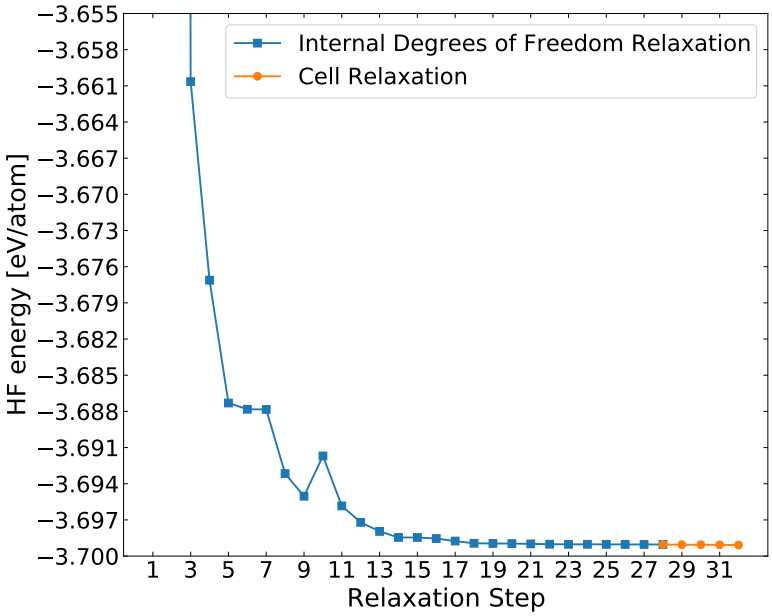

FIGURE 11.9: Two stages of relaxing the C2/c-24 at the DFT pressure 300 GPa using HF forces. On the first stage, the internal degrees of freedom are relaxed, while the cell shape is fixed. During the second stage the cell shape is also allowed to relax. The relaxation of the cell shape has negligible effects on the HF energy.

states were obtained using Optimised Norm-Conserving Vanderbilt Pseudopotential (ONCVPSP) pseudopotential file [188] with a kinetic energy cutoff at 100 Ry (1360.569 eV) and a uniform $4\times4\times4$ k-mesh. In the `YAMBO` calculations, the electron-phonon self-energies were obtained using 100 random q-points in the phonon Brillouin zone, a uniform $4\times4\times4$ k-mesh for electronic Brillouin zone and 300 electronic bands. The convergence tests are given as follows.

11.4.6 Exciton Binding Energy

The electron-hole interactions were obtained using Vienna *ab initio* simulation package (`VASP`) in solving Bethe-Salpeter equation (BSE). 800 eV energy cutoff and 96 electronic bands are used. A dense uniform $4\times4\times4$ k-mesh is necessary to converge the oscillator strength (see Fig. 11.13).

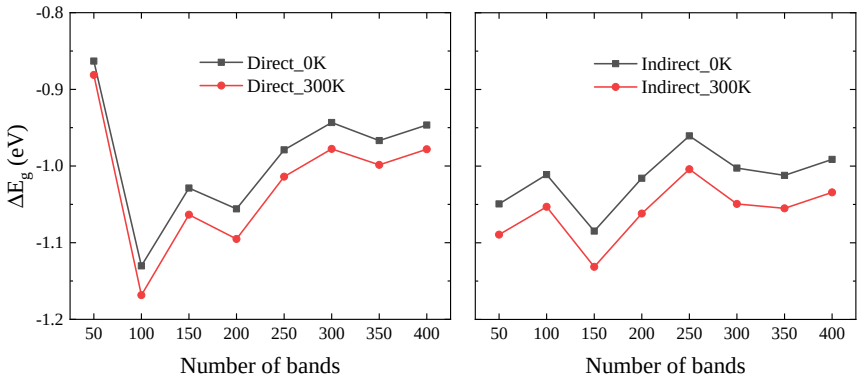

FIGURE 11.10: The convergence test of the direct (black) and indirect (red) band gaps renormalisation as a function of the number of electronic bands at 0 K and 300 K, respectively. The structure is model phase III (C2/c-24) obtained using DFT-PBE at 250 GPa. 5 random q-points and $4 \times 4 \times 4$ k-mesh are used.

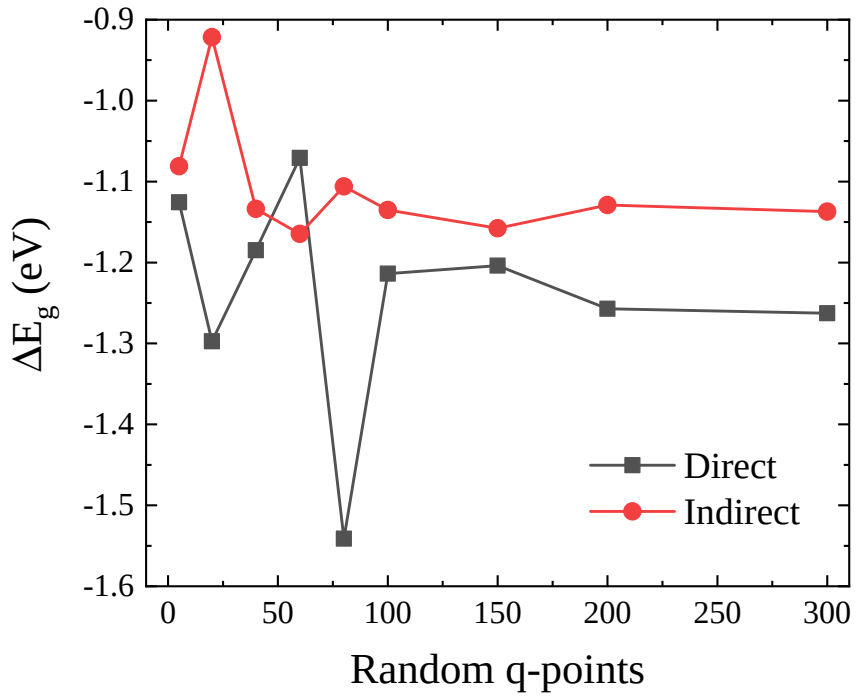

FIGURE 11.11: The convergence test of the direct (black) and indirect (red) band gaps renormalisation as a function of the number of random q-points. The structure is model phase III (C2/c-24) obtained using DFT-PBE at 250 GPa. The number of electronic bands is 64 and $4 \times 4 \times 4$ k-mesh is used.

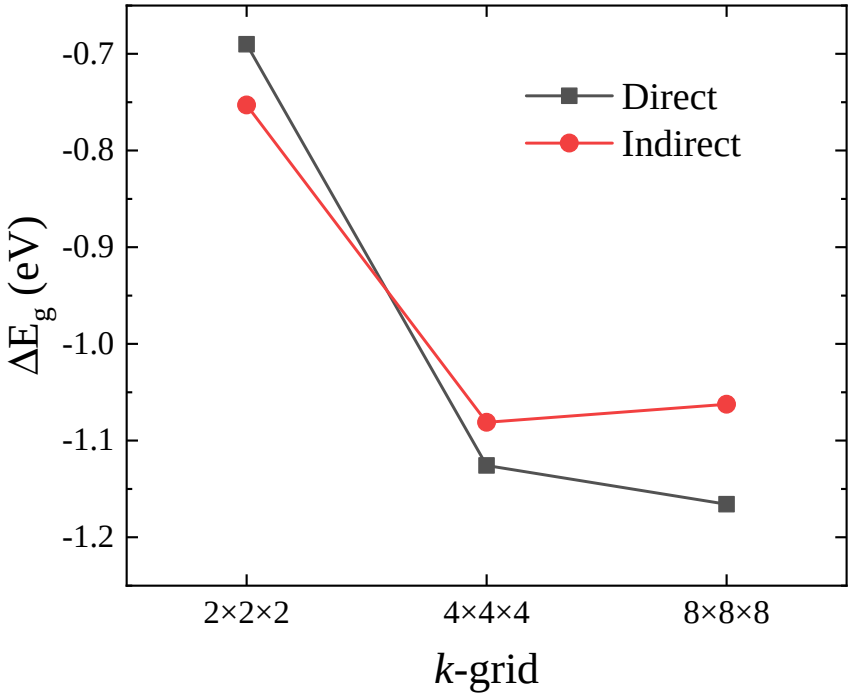

FIGURE 11.12: The convergence test of the direct (black) and indirect (red) band gaps renormalisation as a function of the number of k-points. The structure is model phase III (C2/c-24) obtained using DFT-PBE at 250 GPa. 5 random q-points and 64 electronic bands are used.

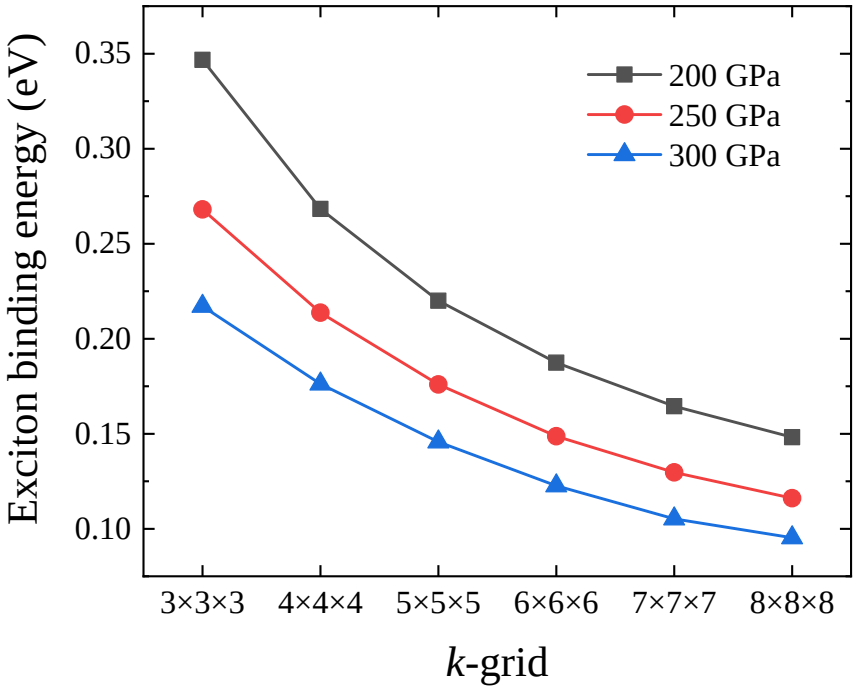

FIGURE 11.13: The convergence tests of the exciton binding energy as a function of the number of k-mesh. The structure is model phase III (C2/c-24) obtained using DFT-PBE at 200, 250 and 300 GPa, respectively.

Chapter 12

Transcorrelated Coupled Cluster Studies on 3D UEG

This chapter contains work in the manuscript titled "Towards efficient and accurate *ab initio* solutions to periodic systems via transcorrelation and coupled cluster theory", by Ke Liao, Thomas Schraivogel, Hongjun Luo, Daniel Kats and Ali Alavi. It can be found online at this link: https://arxiv.org/abs/2103.03176. As of the time the thesis is written, it is accepted by Physical Review Research. Ke Liao, Daniel Kats and Ali Alavi conceived this project and contributed to the writing of the manuscript; Ke Liao implemented the TC-CC algorithm and carried out the calculations to produce the main results; Thomas Schraivogel contributed to the resolving of several important bugs that improved the main results; Hongjun Luo contributed to the full three body interactions in the FCIQMC algorithm and some theoretical developments in the TC integrals.

12.1 Introduction

The 3D UEG model assumes that the background is evenly and positively charged, and that the electrons interact with each other via the Coulomb interaction. As simple as it is, the UEG possesses an intricate phase diagram [189, 190], which can only be accurately described by theories that perform consistently well over a broad range of densities. Historically, the UEG model has also played an important role in the development of many useful approximations. For example, several successful local and gradient-corrected density functionals [191, 192, 165] are based on the UEG; the random phase approximation (RPA) [24, 25] was developed in a pursuit of understanding metals using the UEG as a model. In recent years, the UEG has attracted studies from various highly accurate *ab initio* methods and spurred the development of several new methods [111, 167, 193, 43, 194, 195, 196, 168, 116, 197].

When applying CC to the UEG, we work in a plane wave basis; momentum conservation then excludes all single excitations from the CC ansatz, greatly simplifying the resulting amplitude equations. We refer to Sec. 4.5 for the details of CCD and DCD theories. As a result, the TC Hamiltonian can be treated with relative ease, allowing us to investigate whether the CC method can be beneficially applied to the TC Hamiltonian.

As shown in Ref. [116], the second quantized form of the $\hat{H}_{\text{tc}}$ in a plane wave basis for 3D UEG is

$$\begin{aligned}\hat{H}_{\text{tc}} = \hat{H} &+ \frac{1}{2}\sum_{\sigma\sigma'}\sum_{pqrs}\omega_{pq}^{rs}a_{p,\sigma}^{\dagger}a_{q,\sigma'}^{\dagger}a_{s,\sigma'}a_{r,\sigma} \\ &+ \frac{1}{2}\sum_{\sigma\sigma'\sigma''}\sum_{pqorst}\omega_{pqo}^{rst}a_{p,\sigma}^{\dagger}a_{q,\sigma'}^{\dagger}a_{o,\sigma''}^{\dagger}a_{t,\sigma''}a_{s,\sigma'}a_{r,\sigma},\end{aligned} \tag{12.1}$$

where momentum conservation requires $\mathbf{k} \equiv \mathbf{k}_r - \mathbf{k}_p$, $\mathbf{k}' \equiv \mathbf{k}_q - \mathbf{k}_s$ and $\mathbf{k}_o = \mathbf{k}_t + \mathbf{k} - \mathbf{k}'$, and we define

$$\begin{aligned}\omega_{pq}^{rs} = &\frac{1}{\Omega}\left[k^2\tilde{u}(\mathbf{k}) - (\mathbf{k}_r - \mathbf{k}_s)\cdot\mathbf{k}\tilde{u}(\mathbf{k})\right] \\ &+ \frac{1}{\Omega}\sum_{\mathbf{k}'}(\mathbf{k}-\mathbf{k}')\cdot\mathbf{k}'\tilde{u}(\mathbf{k}-\mathbf{k}')\tilde{u}(\mathbf{k}'),\end{aligned} \tag{12.2}$$

$$\omega_{pqo}^{rst} = -\frac{1}{\Omega^2}\tilde{u}(\mathbf{k})\tilde{u}(\mathbf{k}')\mathbf{k}\cdot\mathbf{k}'. \tag{12.3}$$

We will investigate the CCD and DCD approximations, in the context of the TC Hamiltonian (TC-CCD/TC-DCD), using the framework as outlined in Sec. 9.4 with the approximations to the 3-body terms as discussed in Sec. 9.3. The necessary contractions for the approximations are presented at the end of this chapter. We show that with a suitable form of the correlator, the basis set convergence can be greatly accelerated (as expected), but in addition highly accurate energies can be obtained across a broad range of densities $0.5 \leq r_s \leq 50$, covering both the weakly and strongly correlated regimes. This gives us confidence that the method, once suitably generalised to real systems (which will need to include the singles contribution), will allow a highly accurate yet efficient methodology for the solid state.

We demonstrate our scheme for choosing the optimal parameters in the correlator in Sec. 12.2; we showcase and discuss our TC-CCD/DCD results in comparison with benchmark data in Sec. 12.3; and finally we conclude the chapter in Sec. 12.4 with some outlooks for future directions.

12.2 Choice and Optimization of the Correlator

Past experience with the TC method has shown that the form of the correlator $\hat{\tau}$ is of extreme importance in the TC method, otherwise the benefit of transcorrelation is lost – Φ can be simpler than Ψ only if the correlator captures the correct physics of the pair correlations in the system. An inappropriate correlator can actually lead to a harder problem than the original Schrödinger equation. In our previous study of the exact TC method in the UEG, we proposed a form of the correlator (shown below) which was found to work successfully in accelerating convergence to the basis set limit, without changing the correlation that could be captured with the basis set by a FCI level Φ function. In the present study, since we will be approximating the Φ with the CC ansatz, we additionally require the correlator $\hat{\tau}$ to capture some of the correlation inside the Hilbert space.

Here we propose a physically motivated correlator that mimics the behavior of the correlation hole between two unlike-spin electrons as r_s varies in 3D UEG. The correlation hole can be examined by the pair-correlation function $g(r_{12})$ in real space, as studied in Ref. [198], which shows that the correlation hole between two unlike-spin electrons grows deeper and wider as the Wigner-Seitz radius r_s increases or as the electron density decreases. Fig. 12.1 provides a sketch of the Jastrow factor with our proposed correlator $u(r_{12})$ as the exponent, which captures the desired behavior. We point out that the functional form of this correlator, which reads in real and reciprocal space respectively as

$$u(r) = -\frac{r}{\pi}\left(\mathrm{si}(k_c r) + \frac{\cos(k_c r)}{k_c r} + \frac{\sin(k_c r)}{(k_c r)^2}\right), \tag{12.4}$$

$$\tilde{u}(\mathbf{k}) = \begin{cases} -\frac{4\pi}{k^4}, & |\mathbf{k}| > k_c, \\ 0, & |\mathbf{k}| \leq k_c, \end{cases} \tag{12.5}$$

where $\mathrm{si}(x) = -\int_x^\infty \frac{\sin(t)}{t}\mathrm{d}t$, was first reported in Ref. [116] to satisfy the cusp condition between two electrons with opposite spins at short inter-electron distance and its influence is reduced to nonexistence as the complete basis set (CBS) limit is reached. This was done by choosing k_c to be the same as the plane wave cutoff momentum, k_F, which defines how many plane waves are included as basis functions. In contrast, to mimic the behavior of the pair-correlation function, as a first attempt in the present study we choose the parameter in this correlator such that the first nonzero root of Eq. (12.4) is fixed to be at r_s,

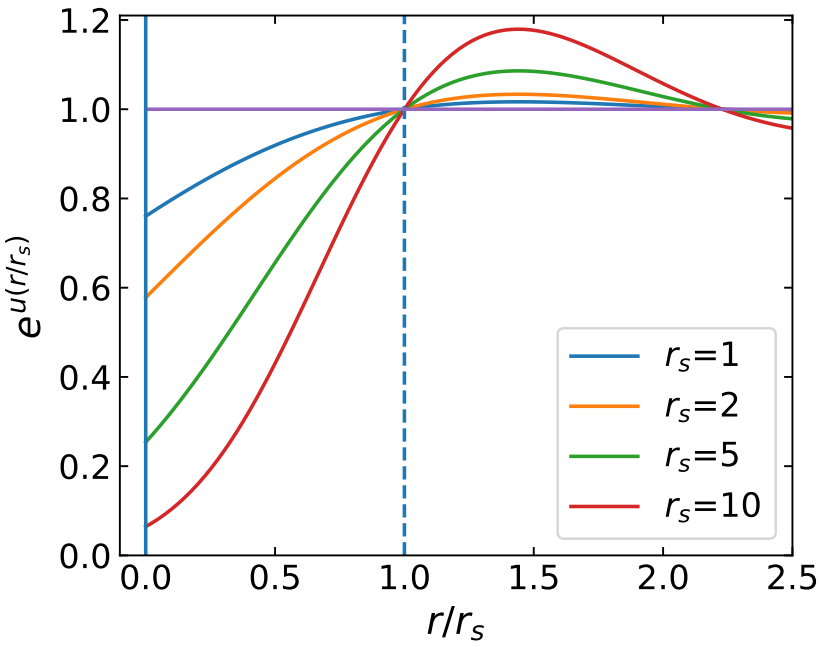

FIGURE 12.1: A sketch of the Jastrow factor with the proposed correlator as the exponent.

irrespective of the basis set. This is achieved by setting

$$k_c = \frac{R_1}{r_s}, \tag{12.6}$$

where $R_1 \approx 2.322502989$. This choice can be rationalized by the physical picture that at lower densities, electrons prefer to stay further away from each other. Furthermore, this correlator, regardless of the choice of k_c, retains the cusp condition for two electrons with unlike-spins at $r = 0$ [116] and should increase the convergence rate of the computed energies with respect to the employed basis set towards the CBS limit.

To further justify the choice of this correlator, we show that for UEG with 14 electrons at $r_s = 5$, where traditional CCD exhibits a large error, the most compact expansion of the wavefunction in Slater determinant space is reached at this value of k_c. In Fig. 12.2, we show the weights of the HF determinant extracted from TC-FCIQMC simulations using different k_c values, without making approximations to the 3-body operator. We note that due to the discrete momentum mesh as a result of using a finite simulation cell, the possible choices are $k_c = \frac{2\pi\sqrt{n}}{L}$, $n \in \mathbb{N}$ [1], where L is the length of the cubic cell. In this case, $k_c = \frac{R_1}{r_s}$ is equivalent to $k_c = \frac{2\sqrt{2}\pi}{L}$, and for this choice of k_c the exact ground

[1] $n = n_1^2 + n_2^3 + n_3^2$, where n_1, n_2, n_3 are the components of a $\mathbf{k}$ vector in units of $\frac{2\pi}{L}$. So the possible values of n are 0, 1, 2, 3, 4, 5, 6, 8, ...

state wavefunction of the transcorrelated Hamiltonian has the highest weight on the HF determinant.

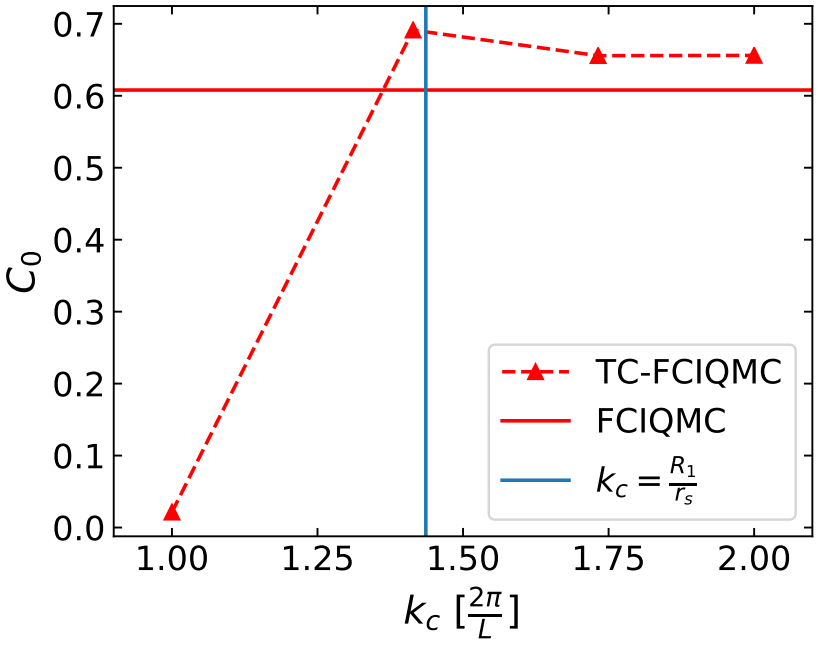

FIGURE 12.2: The weights of the HF determinant (Fermi sphere) as a function of k_c extracted from their corresponding TC-FCIQMC simulations (red dashed line), and that of the normal FCIQMC simulation (horizontal red solid line). The system consists of 14 electrons with $r_s = 5$ and a basis set including 57 plane waves. 5×10^8 walkers are used in all simulations and the initiator threshold is set to 3. No approximations are made to the 3-body interactions.

However, we find that this intuitive choice of k_c is not always the optimal, especially at extremely low density regimes. It is reasonable to expect that the optimal k_c for those systems should deviate slightly from $\frac{R_1}{r_s}$. So we scan a range of k_c values around it to locate the one that minimizes the norm of the closed-shell amplitudes for double excitations of electrons with opposite spins, $\|T_2^{\downarrow\uparrow}\|$, in the TC-CCD/DCD calculations with a small basis set, see Fig. 12.3 [2].

Ideally, two separate correlators should be used for electrons with parallel and anti-parallel spins, and their parameters should be optimized simultaneously using the norm of the full amplitudes in a similar manner. For the present study, we argue that the correlations between two parallel-spin electrons are dominated by the exchange effects, which are already captured by

[2]Since the $\|T_2^{\downarrow\uparrow}\|$ in TC-CCD and TC-DCD show the same trend as a function of k_c, we show only the latter in the figure.

the anti-symmetry in the Slater determinants. Therefore, we focus on capturing the correct physics between electrons with opposite spins in the correlator, i.e. the changing depth and width of the correlation hole as a function of r_s [198], and minimizing the corresponding amplitudes in the CC ansätze. Indeed, we found in practice the minima in $\|T_2^{\downarrow\uparrow}\|$ as a function of k_c are more pronounced, and thus easier to spot than those in the norm of the full amplitudes, $\|T_2\|$. We stress that this compact form of wavefunction at the optimal choice of k_c should greatly benefit approximate methods like CCD and DCD, whose accuracy relies on the assumption that the true ground state wavefunction is compact around the reference determinant, which is normally chosen to be the HF determinant.

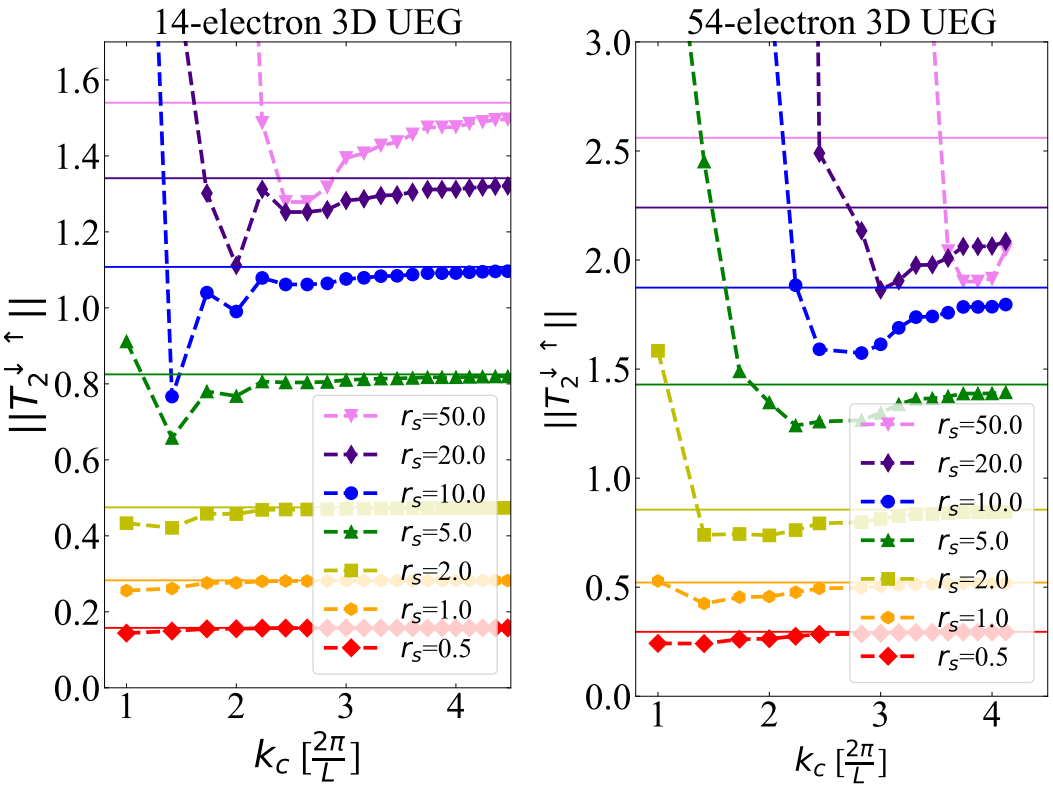

(A) (B)

FIGURE 12.3: The norm of the amplitudes for excitations of unlike-spin electron pairs, $\|T_2^{\downarrow\uparrow}\|$, as a function of k_c, calculated by TC-DCD method. The 14-electron and 54-electron systems use a basis set including 57 and 257 plane waves, respectively. All possible contractions from the 3-body interactions are included, excluding the normal-ordered 3-body interactions. The solid horizontal color lines represent the $\|T_2^{\downarrow\uparrow}\|$ in the canonical DCD calculations with the same settings as their TC counterparts.

By including the most important contractions, the error of neglecting the rest

of the 3-body interactions are well under control in that it scales approximately as $\tilde{u}^2(k)k^2 \sim \frac{1}{k^6}$. We note in passing that if we choose correlators that do not truncate at small k, such as the Yukawa-Coulomb correlator in Ref. [19] or the Gaskell correlator in Ref. [199], the iterative solution of the amplitude equations becomes too unstable to converge at low densities. We attribute this instability in these cases to the large missing normal-ordered 3-body interactions, similar to the instability in a HF self-consistent solution when the missing normal-ordered Coulomb interactions are large.

The FCIQMC calculations are carried out using the NECI program [200]. The CCD and DCD along with the TC integrals are implemented in a Python program using the automatic tensor contraction engine CTF [83] and the NumPy package [201].

12.3 Results

TABLE 12.1: Total energy (a.u./electron), including the Madelung constant, of the 14-electron 3D UEG using different methods. TC-FCIQMC data are from Ref. [116] and BF-DMC data are from Ref. [194]

r_s	k_c $(\frac{2\pi}{L})$	CCD	DCD	TC-CCD	TC-DCD	TC-FCIQMC	BF-DMC
0.5	1	3.41278	3.41252	3.41258	3.41244	3.41241(1)	3.41370(2)
1.0	1	0.56975	0.56909	0.56891	0.56859	0.56861(1)	0.56958(1)
2.0	$\sqrt{2}$	-0.00623	-0.00748	-0.00707	-0.00800	-0.00868(2)	-0.007949(7)
5.0	$\sqrt{2}$	-0.07618	-0.07788	-0.07816	-0.07929	-0.08002(2)	-0.079706(3)
10.0	$\sqrt{2}$	-0.05137	-0.05289	-0.05420	-0.05509	N/A	-0.055160(2)
20.0	2	-0.02924	-0.03035	-0.03136	-0.03201	N/A	-0.0324370(8)
50.0	$\sqrt{6}$	-0.01261	-0.01323	-0.01350	-0.01384	N/A	-0.0146251(3)

TABLE 12.2: Total energy (a.u./electron), including the Madelung constant, of the 54-electron 3D UEG using different methods. TC-FCIQMC data are from Ref. [116] and the BF-DMC data are from Ref. [202]

r_s	k_c $(\frac{2\pi}{L})$	CCD	DCD	TC-CCD	TC-DCD	TC-FCIQMC	BF-DMC
0.5	$\sqrt{2}$	3.22079	3.22052	3.22077	3.22071	3.22042(2)	3.22112(4)
1.0	$\sqrt{2}$	0.53069	0.53001	0.52982	0.52968	0.52973(3)	0.52989(4)
2.0	2	-0.01162	-0.01286	-0.01324	-0.01379	N/A	-0.01311(2)
5.0	$\sqrt{5}$	-0.07492	-0.07655	-0.07750	-0.07837	N/A	-0.079036(3)
10.0	$2\sqrt{2}$	-0.05016	-0.05157	-0.05230	-0.05322	N/A	-0.054443(2)
20.0	3	-0.02846	-0.02925	-0.03055	-0.03113	N/A	-0.032047(2)
50.0	4	-0.01223	-0.01267	-0.01263	-0.01281	N/A	N/A

We first examine the basis set convergence behavior of TC-CCD/DCD compared to the canonical ones. In Fig. 12.4 we present the total energy per electron

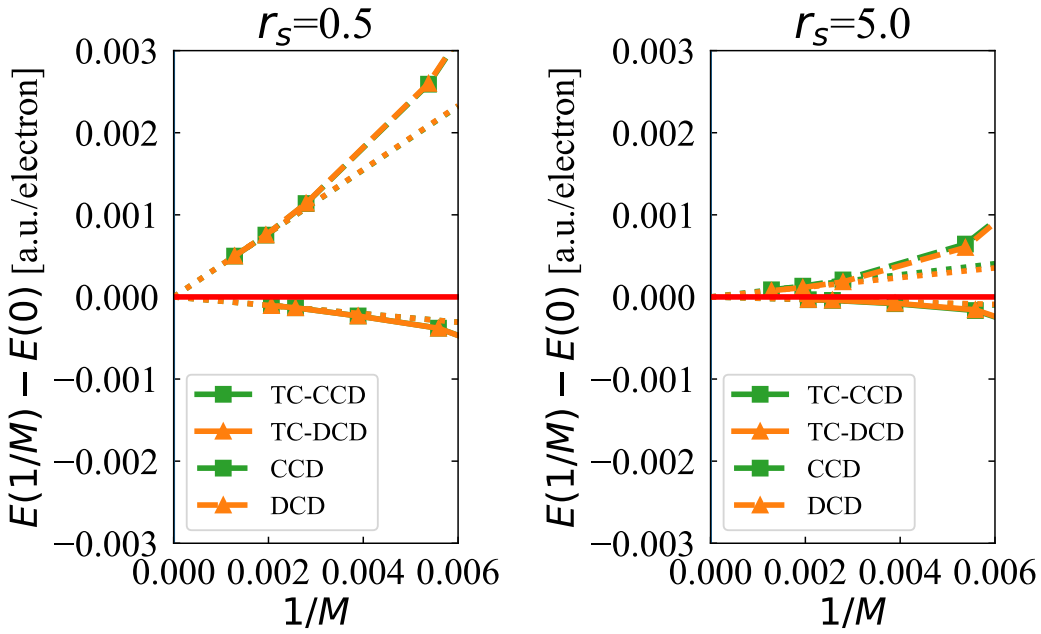

(A) (B)

FIGURE 12.4: Total energy per electron relative to the extrapolated value retrieved as a function of $1/M$, where M is the number of plane wave basis functions for 3D UEG with 14 electrons. Linear extrapolations using the left most two points are used in all cases.

relative to the extrapolated value for each method, retrieved as a function of the inverse of the employed number of plane waves, $1/M$. As mentioned before, our correlator satisfies the cusp condition at the coalescence point of two electrons with opposite spins. So the accelerated convergence behavior in the TC methods compared to the canonical ones is not surprising. The acceleration is the most obvious at high density regimes, since at low densities the required number of basis functions to reach convergence in both the TC and non-TC methods is relatively small. These observations are consistent with those of the TC-FCIQMC reported in Ref. [116].

The optimal k_c values, (TC-)CCD/DCD energies at CBS and the benchmark data are listed in Table 12.1 and 12.2 for the 14- and 54-electron 3D UEG, respectively. In Fig. 12.5 we present the errors of total energies per electron calculated by TC-CCD, TC-DCD, CCD and DCD relative to the most accurate FCIQMC [116, 193, 196] and backflow DMC (BF-DMC) [202, 194] results on the 14- and 54-electron 3D UEG. The finite basis set errors in our methods have been carefully eliminated by extrapolation to the CBS limit.

In general the accuracies of the TC methods are greatly improved compared

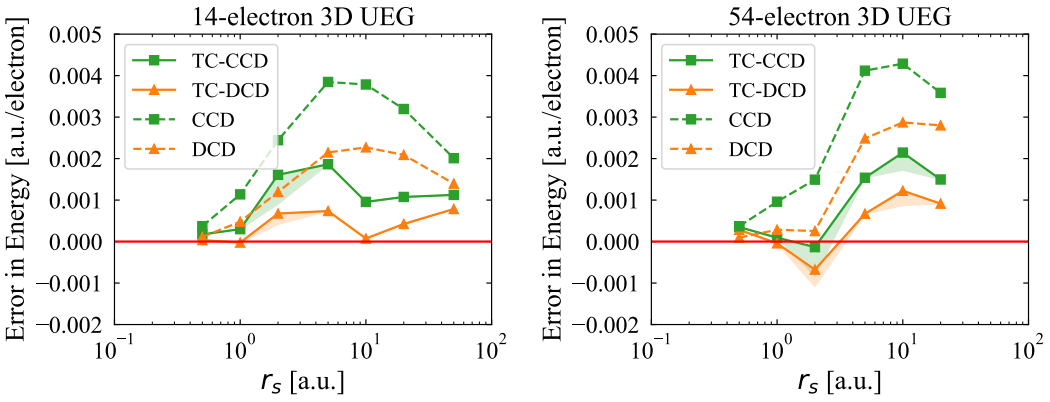

(A) (B)

FIGURE 12.5: Errors in energy per electron relative to benchmark data on the 3D UEG using TC-CCD, TC-DCD, CCD and DCD methods. (a) Results for 14 electrons. For $r_s = 0.5 - 5$, TC-FCIQMC data [116] are used and for the rest BF-DMC data [194] are used for benchmark. (b) Results for 54 electrons. For $r_s = 0.5 - 1$, TC-FCIQMC data [116] are used and for the rest BF-DMC data [202] are used for benchmark. The grey shaded areas stand for the ± 0.001 a.u./electron accuracy relative to the reference data. The colorful shaded areas reflect the uncertainties in the TC-CCD and TC-DCD energies due to slightly different choices of the k_c values.

to their canonical counterparts, especially in regions ($r_s = 5 - 50$) where the latter exhibit the largest errors. More importantly, the improved accuracies are retained when going from the 14- to the 54-electron system. We highlight that the TC-DCD achieves an accuracy of ≤ 0.001 a.u./electron across a wide range of densities, i.e. $r_s = 0.5 - 50$ for the 14-electron and $r_s = 0.5 - 20$ for the 54-electron 3D UEG, with an exception at $r_s = 10$ for the latter where it drops slightly out of the 0.001 a.u./electron accuracy. We argue that with the next possible smaller value of $k_c = \sqrt{6}$, which yields a marginally higher $\|T_2^{\downarrow\uparrow}\|$, instead of the current choice of $k_c = 2\sqrt{2}$, the 0.001 a.u./electron accuracy at $r_s = 10$ can be regained. The discrete grid of the k-mesh makes it hard to pick the optimal k_c in Fig. 12.3b. However, as the system gets larger and the k-mesh gets finer, the $\|T_2^{\downarrow\uparrow}\|$ as a function of k_c will also be smoother, and the choice of the optimal k_c will become more definite. We use colorful shaded areas in Fig. 12.5 to reflect the uncertainties due to the possible choices of k_c which yield similar $\|T_2^{\downarrow\uparrow}\|$ values in Fig. 12.3.

At high densities, i.e. $r_s = 0.5 - 2$, the canonical DCD is already very accurate, and the main benefit from TC there is in accelerating the basis set convergence. Overall, DCD exhibits smaller errors than CCD, which agrees

with earlier comparative studies between DCSD and CCSD [35, 104, 105].

12.4 Discussions

We demonstrated that the correlator Eq. (12.4), used with transcorrelated coupled cluster theory, drastically improves the accuracy of approximate methods, i.e. CCD and DCD, for 3D UEG across a wide range of densities. The basis set convergence rate is also improved thanks to the fact that the correlator satisfies the cusp condition at the coalescence point of two unlike-spin electrons. We have explored the mechanism behind the improved accuracy of the TC-CCD and TC-DCD methods, which is related to a compactification of the many-electron wavefunction in Slater determinant space when the dominant pair correlations between electrons with unlike spins are directly included in the correlator. The optimization of the parameter in the correlator is seamlessly incorporated within the TC-CCD/DCD framework, without requiring an external algorithm. We notice that a range-separation scheme of CCD can also achieve similar accuracy in 3D UEG, but without improving the basis set convergence rate [194]. Comparatively speaking, our methods are systematically improvable, in that a more flexible form of the correlator can be designed by a combination of a series of functions [119] or by a general function approximator, e.g. an artificial neural network, to include further correlation effects such as nuclear-electron correlations and correlations between two parallel-spin electrons in more complicated systems. Other systematic ways of optimizing the correlator in combination with VMC [119] can also be explored. When going to real periodic solids, TC-CCSD and TC-DCSD will be needed; extra efforts are also required to compute the additional integrals besides the Coulomb integrals, where the most computationally demanding part is the singly-contracted 3-body integrals which scales like $\mathcal{O}(N_o N_p^4)$, where N_o and N_p are the number of occupied and total orbitals, respectively. Fortunately, the computation of the extra integrals scales no worse than the CCSD or DCSD algorithm and it can be compensated by the accelerated convergence rate towards CBS limit in the TC framework. These perspectives will be important in extending the encouraging performance of the current TC-CCD and TC-DCD methods from the UEG to real periodic solids with moderate to strong correlation.

12.5 Computational Details

12.5.1 Internal Contractions in the Three-body Integrals

The 3-body integrals can be written as an asymmetric form

$$\hat{W}_3 = -\frac{1}{2\Omega^2}\sum_{\sigma\sigma'\sigma''}\sum_{\mathbf{kk'rst}}\tilde{u}(\mathbf{k'})\tilde{u}(\mathbf{k})\mathbf{k'}\cdot\mathbf{k}a^\dagger_{\mathbf{r-k},\sigma}a^\dagger_{\mathbf{s+k'},\sigma'}a^\dagger_{\mathbf{t+k-k'},\sigma''}a_{\mathbf{t},\sigma''}a_{\mathbf{s},\sigma'}a_{\mathbf{r},\sigma}, \tag{12.7}$$

where the conservation of momentum is used. In the following subsections, we will show the specific mathematical expressions for all contractions. The expressions are derived by using the Goldstone diagrams (not shown).

Single Contractions

There are 4 types of different single contractions, which are

$$\begin{aligned}
\hat{W}_3^{S1} &= -\frac{N_e}{2\Omega^2}\sum_{\sigma\sigma'}\sum_{\mathbf{krs}}(\tilde{u}(\mathbf{k}))^2k^2\{a^\dagger_{\mathbf{r-k},\sigma}a^\dagger_{\mathbf{s+k},\sigma'}a_{\mathbf{s},\sigma'}a_{\mathbf{r},\sigma}\},\\
\hat{W}_3^{S2} &= +\frac{1}{\Omega}\sum_{\sigma\sigma'}\sum_{\mathbf{krs}}\{a^\dagger_{\mathbf{r-k},\sigma}a^\dagger_{\mathbf{s+k},\sigma'}a_{\mathbf{s},\sigma'}a_{\mathbf{r},\sigma}\}\left(\frac{1}{\Omega}\sum_{\mathbf{i}}(\mathbf{i}-\mathbf{r}+\mathbf{k})\cdot\mathbf{k}\tilde{u}(\mathbf{k})\tilde{u}(\mathbf{i}-\mathbf{r}+\mathbf{k})\right),\\
\hat{W}_3^{S3} &= +\frac{1}{\Omega}\sum_{\sigma\sigma'}\sum_{\mathbf{krs}}\{a^\dagger_{\mathbf{r-k},\sigma}a^\dagger_{\mathbf{s+k},\sigma'}a_{\mathbf{s},\sigma'}a_{\mathbf{r},\sigma}\}\left(\frac{1}{\Omega}\sum_{\mathbf{i}}(\mathbf{r}-\mathbf{i})\cdot\mathbf{k}\tilde{u}(\mathbf{k})\tilde{u}(\mathbf{r}-\mathbf{i})\right),\\
\hat{W}_3^{S4} &= +\frac{1}{\Omega}\sum_{\sigma\sigma'}\sum_{\mathbf{krs}}\{a^\dagger_{\mathbf{r-k},\sigma}a^\dagger_{\mathbf{s+k},\sigma'}a_{\mathbf{s},\sigma'}a_{\mathbf{r},\sigma}\}\left(\frac{1}{\Omega}\sum_{\mathbf{i}}(\mathbf{r}-\mathbf{i}-\mathbf{k})\cdot(\mathbf{r}-\mathbf{i})\tilde{u}(\mathbf{r}-\mathbf{i})\tilde{u}(\mathbf{r}-\mathbf{i}-\mathbf{k})\right),
\end{aligned} \tag{12.8}$$

where the curly brackets refer to normal-ordering with respect to the reference determinant. Now we can define the $\tilde{\omega}^{rs}_{pq}$ by the following relation

$$\frac{1}{2}\sum_{\sigma\sigma''}\sum_{pqrs}\tilde{\omega}^{rs}_{pq}\{a^\dagger_{\mathbf{p},\sigma}a^\dagger_{\mathbf{q},\sigma'}a_{\mathbf{s},\sigma'}a_{\mathbf{r},\sigma}\} = \hat{W}_3^{S1}+\hat{W}_3^{S2}+\hat{W}_3^{S3}+\hat{W}_3^{S4}, \tag{12.9}$$

However, we notice that this effective 2-body integral is not symmetric with respect to the exchange of two electrons, due to the fact we used an asymmetric form of the 3-body integral. So we need to symmetrised it as follows

$$\tilde{\omega}^{rs}_{pq} \leftarrow \frac{1}{2}(\tilde{\omega}^{rs}_{pq}+\tilde{\omega}^{sr}_{qp}). \tag{12.10}$$

Double Contractions

The double contractions in the 3-body integrals result in the $\tilde{\omega}_p$ in the main text. It is a sum of 5 types of double contractions, which reads

$$\begin{aligned}\tilde{\omega}_p = &\frac{N_e}{\Omega^2}\left(\sum_{\mathbf{i}} \tilde{u}^2(\mathbf{p}-\mathbf{i})(\mathbf{p}-\mathbf{i})^2\right) \\ &- \frac{1}{\Omega^2}\left(\sum_{\mathbf{ij}} (\mathbf{p}-\mathbf{i})\cdot(\mathbf{p}-\mathbf{j})\tilde{u}(\mathbf{p}-\mathbf{i})\tilde{u}(\mathbf{p}-\mathbf{j})\right) \\ &- \frac{1}{\Omega^2}\left(\sum_{\mathbf{ij}} (\mathbf{i}-\mathbf{j})\cdot(\mathbf{i}-\mathbf{p})\tilde{u}(\mathbf{i}-\mathbf{j})\tilde{u}(\mathbf{i}-\mathbf{p})\right) \\ &- \frac{1}{\Omega^2}\left(\sum_{\mathbf{ij}} (\mathbf{j}-\mathbf{i})\cdot(\mathbf{p}-\mathbf{i})\tilde{u}(\mathbf{j}-\mathbf{i})\tilde{u}(\mathbf{p}-\mathbf{i})\right) \\ &+ \frac{1}{\Omega^2}\left(\sum_{\mathbf{ij}} (\mathbf{i}-\mathbf{j})^2\tilde{u}^2(\mathbf{i}-\mathbf{j})\right).\end{aligned} \tag{12.11}$$

Triple Contractions

There are 2 types of triple contractions which contribute to E_{T}

$$E_{\mathrm{T}} = \frac{N_e}{2\Omega^2}\sum_{\sigma}\sum_{\mathbf{ij}} \tilde{u}^2(\mathbf{i}-\mathbf{j})(\mathbf{i}-\mathbf{j})^2 - \frac{1}{\Omega}\sum_{\sigma}\sum_{\mathbf{ij}}\left(\frac{1}{\Omega}\sum_{\mathbf{k}} (\mathbf{i}-\mathbf{k})\cdot(\mathbf{i}-\mathbf{j})\tilde{u}(\mathbf{i}-\mathbf{j})\tilde{u}(\mathbf{i}-\mathbf{k})\right) \tag{12.12}$$

Part V

Summary and Outlook

In this thesis, the Theory part is dedicated to the review of the essential theories on which the new works in this thesis are based. Starting from the very basic concepts in quantum mechanics, we introduce the quantum many-body problem, along with the well-known BO approximation to decouple the electronic and nuclear problems and the Bloch's theorem relevant to periodic solids in the first chapter. As an example of periodic systems, we introduce the model system of 3D UEG at the end of the first chapter. Eventually, we review a host of important *ab initio* electronic structure theories, including the mean field theories such as HF and DFT in chapter 2, perturbation theories like MP2 and G_0W_0, wavefunction-based CC theories in chapter 4 and two popular QMC methods in chapter 5. The problem of finite size errors in periodic solids is explained and the two approaches to fix them are introduced in chapter 6. In the last chapter of part II, we go through the main ideas and theoretical formulations of the HAC theory, which provides corrections to the quasiparticle energies due to the electron-phonon interactions at 0 K and finite temperatures.

In part III of this thesis, the theories and algorithms which are developed during my PhD study are introduced. There are two main developments, each is motivated at the beginning with a section of "Motivations". The first half of this part is about the implementation of MP2 forces using plane wave basis functions and the framework we use to optimise the atomic structures of periodic solids. The second part is focused on improving the efficiency and accuracy of CC methods by combining them with the transcorrelation scheme, forming the so-called TC-CC framework. The important step in this framework is on the approximations made to the 3-body operators in the transcorrelated Hamiltonian, without which the TC-CC method is computationally too expensive to be applicable to any realistic periodic systems.

Part IV presents results obtained using existing and newly developed methods on systems such as solid hydrogen phases and 3D UEG. In chapter 10, we compare the strengths and weaknesses of various methods, including DFT, CC and QMC, applied to the solid hydrogen phases at high pressures. Especially, we show that CCSD, with recent developments that improve its efficiency, can match the state-of-the-art DMC theory in predictions of the relative stabilities of different phases. Considering the model structures of solid hydrogen in the previous chapter were optimised by DFT-PBE, which contains uncontrolled errors in the XC functional, we use the newly developed algorithm that computes the MP2 forces using a plane wave basis; the MP2 forces are then used to further optimise the DFT-PBE model structures. The resulting MP2 structures have more stable total CCSD energies and show almost perfect agreement in

the H_2 vibron frequencies as a function of pressure with experiments. The EPI corrected G_0W_0 band gaps are also in reasonable good agreement with recent experiments. In the last chapter of Part IV, we apply our TC-CC methods, e.g. TC-CCD and TC-DCD, on 3D UEG. We show that, after optimising the parameters in the TC correlator, a great deal of improvement in both accuracies and efficiencies can be gained. Most noticeably, the resulting TC-CCD/DCD method has significantly reduced errors in the energies compared to their canonical counterparts, using the QMC results as benchmarks.

In the future, extension of the TC methods to real solids will be investigated, where the computation of the TC integrals and the choice of correlators will be the main concerns. In real solids, the oscillatory behavior of the wavefunction close to the nuclei needs to be treated by the PAW method, in order to produce accurate integrals for the TC Hamiltonian. More flexible choices of the correlator will also be explored, such as artificial neural networks. We believe that the improved accuracies and efficiencies of the TC-CC methods in the 3D UEG can be transferred to real solids, which will largely extend the scope of what we currently can achieve in the studies of solid phase diagrams using CC and methods alike.

Glossary

$S(\mathbf{G})$ transition structure factor. 57

3D UEG three dimensional uniform electron gas. 5, 6, 41, 121, 122

BO Born-Oppenheimer. 3–5, 11, 59, 61, 121

CBS complete basis set. 26, 37, 53

CC coupled cluster. 4, 5, 38, 39, 121, 122

CCD coupled cluster doubles. 5, 6, 31, 34, 39, 41, 42, 44, 121

CCSD coupled cluster singles and doubles. 4, 5, 24, 31, 37, 39, 41, 42, 44, 45, 56, 67–82, 84, 85, 93, 96–102, 121

CCSD(T) coupled cluster singles and doubles plus perturbative triples. 4, 31, 44, 45, 72–74

CI configuration interaction. 39

CISD configuration interaction singles and doubles. 39

DCD distinguishable cluster doubles. 5, 31, 39, 42, 44, 121

DCSD distinguishable cluster singles and doubles. 31, 42, 44, 72–75

DFT density functional theory. 4, 5, 17, 23, 24, 33, 34, 66, 84, 100, 121

DMC diffusion Monte Carlo. 4, 5, 24, 47–49, 53, 54, 57, 66, 67, 72, 77, 78, 80–82, 100, 121

DMRG density matrix renormalisation group. 18

EPI electron-phonon interaction. 5, 6, 12, 59, 121

FCI full configuration interaction. 27, 38, 39, 50, 51

FCIQMC full configuration interaction quantum Monte Carlo. 5, 47, 48, 50–54, 56, 67, 72–75, 80, 81

FN-DMC fixed-node diffusion Monte Carlo. 49, 50

HF Hartree-Fock. 4, 5, 18, 21–27, 32, 35, 40, 42, 50, 76, 79, 86, 88–92, 121

HFOs Hartree-Fock orbitals. 67–69, 71–74

KS Kohn-Sham. 23, 34, 59, 60

MP2 second order Møller-Plesset perturbation. 5, 6, 12, 31, 37, 45, 56, 84–102, 121

MP2NOs MP2 natural orbitals. 67–69, 71–74

PAW projector augmented wave. 19

PES potential energy surface. 12

QMC quantum Monte Carlo. 4, 10, 24, 47–49, 121

r.h.s. right hand side. 10

RPA random phase approximation. 34, 41

SD Slater determinant. 27, 30, 56

SJ Slater-Jastrow. 4

ST similarity transformation. 5

TA twist-averaging. 55

TC transcorrelation. 5, 6, 121, 122

TDL thermodynamic limit. 12, 45, 55

UEG uniform electron gas. 39

VMC variational Monte Carlo. 18, 50

XC exchange-correlation. 4, 23, 24, 34, 121

Bibliography

[1] Matthias Troyer and UJ Wiese. "Computational Complexity and Fundamental Limitations to Fermionic Quantum Monte Carlo Simulations". In: *Phys. Rev. Lett.* 1.2 (2005), pp. 1–5. arXiv: cond-mat/0408370v1.

[2] Samuel Francis Boys, Nicholas Charles Handy, and John Wilfrid Linnett. "A Condition to Remove the Indeterminacy in Interelectronic Correlation Functions". In: *Proc. R. Soc. Math. Phys. Eng. Sci.* 309.1497 (Mar. 1969), pp. 209–220. DOI: 10.1098/rspa.1969.0038.

[3] Samuel Francis Boys, Nicholas Charles Handy, and John Wilfrid Linnett. "The Determination of Energies and Wavefunctions with Full Electronic Correlation". In: *Proc. R. Soc. Math. Phys. Eng. Sci.* 310.1500 (Apr. 1969), pp. 43–61. DOI: 10.1098/rspa.1969.0061.

[4] Max Planck. "Ueber Das Gesetz Der Energieverteilung Im Normalspectrum". In: *Ann. Phys.* 309.3 (1901), pp. 553–563. ISSN: 1521-3889. DOI: 10.1002/andp.19013090310.

[5] A. Einstein. "Über Einen Die Erzeugung Und Verwandlung Des Lichtes Betreffenden Heuristischen Gesichtspunkt". In: *Ann. Phys.* 322.6 (1905), pp. 132–148. ISSN: 1521-3889. DOI: 10.1002/andp.19053220607.

[6] Kirill Shtengel. "A Home for Anyon?" In: *Nat. Phys.* 3.11 (Nov. 2007), pp. 763–763. ISSN: 1745-2481. DOI: 10.1038/nphys767.

[7] N. W. Ashcroft and N. David. Mermin. *Solid State Physics*. Harcourt College Publishers, 1976.

[8] D. R. Hartree. "The Wave Mechanics of an Atom with a Non-Coulomb Central Field. Part II. Some Results and Discussion". In: *Math. Proc. Camb. Philos. Soc.* 24.1 (Jan. 1928), pp. 111–132. ISSN: 1469-8064, 0305-0041. DOI: 10.1017/S0305004100011920.

[9] J. C. Slater. "Note on Hartree's Method". In: *Phys. Rev.* 35.2 (Jan. 1930), pp. 210–211. DOI: 10.1103/PhysRev.35.210.2.

[10] V. Fock. "Näherungsmethode zur Lösung des quantenmechanischen Mehrkörperproblems". In: *Z. Physik* 61.1 (Jan. 1930), pp. 126–148. ISSN: 0044-3328. DOI: 10.1007/BF01340294.

[11] Douglas Rayner Hartree and W. Hartree. "Self-Consistent Field, with Exchange, for Beryllium". In: *Proceedings of the Royal Society of London. Series A - Mathematical and Physical Sciences* 150.869 (May 1935), pp. 9–33. DOI: 10.1098/rspa.1935.0085.

[12] L. H. Thomas. "The Calculation of Atomic Fields". In: *Math. Proc. Camb. Philos. Soc.* 23.5 (Jan. 1927), pp. 542–548. ISSN: 1469-8064, 0305-0041. DOI: 10.1017/S0305004100011683.

[13] Enrico Fermi. "Un Metodo Statistico per La Determinazione Di Alcune Prioprietà Dell'Atomo". In: *Rend Accad Naz Lincei* 6 (1927), pp. 602–607.

[14] Steven R. White. "Density Matrix Formulation for Quantum Renormalization Groups". In: *Phys. Rev. Lett.* 69.19 (Nov. 1992), pp. 2863–2866. DOI: 10.1103/PhysRevLett.69.2863.

[15] D. Ceperley, G. V. Chester, and M. H. Kalos. "Monte Carlo Simulation of a Many-Fermion Study". In: *Phys. Rev. B* 16.7 (Oct. 1977), pp. 3081–3099. DOI: 10.1103/PhysRevB.16.3081.

[16] Attila Szabo and Neil S. Ostlund. *Modern Quantum Chemistry: Introduction to Advanced Electronic Structure Theory.*

[17] Per-Olov Löwdin. "The historical development of the electron correlation problem". In: *Int. J. Quantum Chem.* 55.2 (1995), pp. 77–102. ISSN: 1097-461X. DOI: 10.1002/qua.560550203.

[18] Tosio Kato. "On the Eigenfunctions of Many-Particle Systems in Quantum Mechanics". In: *Commun. Pure Appl. Math.* 10.2 (1957), pp. 151–177. ISSN: 1097-0312. DOI: 10.1002/cpa.3160100201.

[19] Andreas Grüneis et al. "Explicitly Correlated Plane Waves: Accelerating Convergence in Periodic Wavefunction Expansions". In: *J. Chem. Phys.* 139.8 (Aug. 2013), p. 084112. ISSN: 0021-9606, 1089-7690. DOI: 10.1063/1.4818753.

[20] N. F. Mott. "The Basis of the Electron Theory of Metals, with Special Reference to the Transition Metals". In: *Proc. Phys. Soc. A* 62.7 (July 1949), p. 416. ISSN: 0370-1298. DOI: 10.1088/0370-1298/62/7/303.

[21] Lars Hedin. "New Method for Calculating the One-Particle Green's Function with Application to the Electron-Gas Problem". In: *Phys. Rev.* 139.3A (Aug. 1965), A796–A823. DOI: 10.1103/PhysRev.139.A796.

[22] Richard D. Mattuck. *A Guide to Feynman Diagrams in the Many-Body Problem.* Courier Corporation, Jan. 1992. ISBN: 978-0-486-67047-8.

[23] Xin-zheng Li and Enge Wang. *Computer Simulations Of Molecules And Condensed Matter: From Electronic Structures To Molecular Dynamics*. World Scientific, Jan. 2018. ISBN: 978-981-323-046-0.

[24] David Bohm and David Pines. "A Collective Description of Electron Interactions: III. Coulomb Interactions in a Degenerate Electron Gas". In: *Phys. Rev.* 92.3 (Nov. 1953), pp. 609–625. DOI: 10.1103/PhysRev.92.609.

[25] Murray Gell-Mann and Keith A. Brueckner. "Correlation Energy of an Electron Gas at High Density". In: *Phys. Rev.* 106.2 (1957), pp. 364–368. ISSN: 0031899X. DOI: 10.1103/PhysRev.106.364.

[26] Mark S. Hybertsen and Steven G. Louie. "First-Principles Theory of Quasiparticles: Calculation of Band Gaps in Semiconductors and Insulators". In: *Phys. Rev. Lett.* 55.13 (Sept. 1985), pp. 1418–1421. DOI: 10.1103/PhysRevLett.55.1418.

[27] Mark S. Hybertsen and Steven G. Louie. "Electron Correlation in Semiconductors and Insulators: Band Gaps and Quasiparticle Energies". In: *Phys. Rev. B* 34.8 (Oct. 1986), pp. 5390–5413. DOI: 10.1103/PhysRevB.34.5390.

[28] Falco Hüser, Thomas Olsen, and Kristian S. Thygesen. "Quasiparticle GW Calculations for Solids, Molecules, and Two-Dimensional Materials". In: *Phys. Rev. B* 87.23 (June 2013), p. 235132. DOI: 10.1103/PhysRevB.87.235132.

[29] Trygve Helgaker, Poul Jørgensen, and Jeppe Olsen. "Hartree-Fock Theory". In: *Molecular Electronic-Structure Theory*. John Wiley & Sons, Ltd, 2014, pp. 433–522. ISBN: 978-1-119-01957-2. DOI: 10.1002/9781119019572.ch10.

[30] Andreas Grüneis et al. "Natural Orbitals for Wave Function Based Correlated Calculations Using a Plane Wave Basis Set". In: *J. Chem. Theory Comput.* 7.9 (2011), pp. 2780–2785. ISSN: 15499618. DOI: 10.1021/ct200263g.

[31] Francesco Aquilante et al. "Systematic Truncation of the Virtual Space in Multiconfigurational Perturbation Theory". In: *J. Chem. Phys.* 131.3 (July 2009), p. 034113. ISSN: 0021-9606. DOI: 10.1063/1.3157463.

[32] Jiří Čížek and J Paldus. "Coupled Cluster Approach". In: *Phys Scr* 21.3-4 (1980), p. 251. ISSN: 0031-8949. DOI: 10.1088/0031-8949/21/3-4/006.

[33] Rodney J. Bartlett and Monika Musiał. "Coupled-Cluster Theory in Quantum Chemistry". In: *Rev. Mod. Phys.* 79.1 (Feb. 2007), pp. 291–352. ISSN: 0034-6861, 1539-0756. DOI: 10.1103/RevModPhys.79.291.

[34] Daniel Kats and Frederick R. Manby. "Sparse Tensor Framework for Implementation of General Local Correlation Methods". In: *J. Chem. Phys.* 138.14 (Apr. 2013), p. 144101. ISSN: 0021-9606. DOI: 10.1063/1.4798940.

[35] Daniel Kats and Frederick R. Manby. "Communication: The Distinguishable Cluster Approximation". In: *J. Chem. Phys.* 139.2 (July 2013), p. 021102. ISSN: 0021-9606. DOI: 10.1063/1.4813481.

[36] Daniel Kats. "The Distinguishable Cluster Approach from a Screened Coulomb Formalism". In: *J. Chem. Phys.* 144.4 (Jan. 2016), p. 044102. ISSN: 0021-9606. DOI: 10.1063/1.4940398.

[37] Péter Pulay. "Convergence Acceleration of Iterative Sequences. the Case of Scf Iteration". In: *Chem. Phys. Lett.* 73.2 (July 1980), pp. 393–398. ISSN: 0009-2614. DOI: 10.1016/0009-2614(80)80396-4.

[38] P. Pulay. "Improved SCF Convergence Acceleration". In: *J. Comput. Chem.* 3.4 (1982), pp. 556–560. ISSN: 1096-987X. DOI: 10.1002/jcc.540030413.

[39] Gustavo E. Scuseria, Thomas M. Henderson, and Danny C. Sorensen. "The Ground State Correlation Energy of the Random Phase Approximation from a Ring Coupled Cluster Doubles Approach". In: *J. Chem. Phys.* 129.23 (Dec. 2008), p. 231101. ISSN: 0021-9606. DOI: 10.1063/1.3043729.

[40] D. J. Thouless. "Stability Conditions and Nuclear Rotations in the Hartree-Fock Theory". In: *Nucl. Phys.* 21.C (Nov. 1960), pp. 225–232. ISSN: 00295582. DOI: 10.1016/0029-5582(60)90048-1.

[41] Krishnan Raghavachari et al. "A Fifth-Order Perturbation Comparison of Electron Correlation Theories". In: *Chem. Phys. Lett.* 157.6 (May 1989), pp. 479–483. ISSN: 0009-2614. DOI: 10.1016/S0009-2614(89)87395-6.

[42] Trygve Helgaker, Poul Jørgensen, and Jeppe Olsen. "Perturbation Theory". In: *Molecular Electronic-Structure Theory*. John Wiley & Sons, Ltd, 2014, pp. 724–816. ISBN: 978-1-119-01957-2. DOI: 10.1002/9781119019572.ch14.

[43] James J. Shepherd and Andreas Grüneis. "Many-Body Quantum Chemistry for the Electron Gas: Convergent Perturbative Theories". In: *Phys. Rev. Lett.* 110.22 (2013). ISSN: 00319007. DOI: 10.1103/PhysRevLett.110.226401. arXiv: 1310.6059.

[44] Peter J. Reynolds, Jan Tobochnik, and Harvey Gould. "Diffusion Quantum Monte Carlo". In: *Computers in Physics* 4.6 (Nov. 1990), pp. 662–668. ISSN: 0894-1866. DOI: 10.1063/1.4822960.

[45] Nicholas Metropolis and S. Ulam. "The Monte Carlo Method". In: *J. Am. Stat. Assoc.* 44.247 (Sept. 1949), pp. 335–341. ISSN: 0162-1459. DOI: 10.1080/01621459.1949.10483310.

[46] W. M. C. Foulkes et al. "Quantum Monte Carlo Simulations of Solids". In: *Rev. Mod. Phys.* 73.1 (Jan. 2001), pp. 33–83. DOI: 10.1103/RevModPhys.73.33.

[47] PJ Reynolds and DM Ceperley. "Fixed Node Quantum Monte Carlo for Molecules a) b)". In: *J. ...* 77.11 (1982), p. 5593. ISSN: 00219606. DOI: 10.1063/1.443766.

[48] Nicholas Metropolis et al. "Equation of State Calculations by Fast Computing Machines". In: *J. Chem. Phys.* 21.6 (June 1953), pp. 1087–1092. ISSN: 0021-9606. DOI: 10.1063/1.1699114.

[49] James B. Anderson. "A Random-walk Simulation of the Schrödinger Equation: H+3". In: *J. Chem. Phys.* 63.4 (Aug. 1975), pp. 1499–1503. ISSN: 0021-9606. DOI: 10.1063/1.431514.

[50] James B. Anderson. "Quantum Chemistry by Random Walk. H 2P, H+3 D3h 1A′1, H2 3Σ+u, H4 1Σ+g, Be 1S". In: *J. Chem. Phys.* 65.10 (Nov. 1976), pp. 4121–4127. ISSN: 0021-9606. DOI: 10.1063/1.432868.

[51] C. J. Umrigar. "Observations on Variational and Projector Monte Carlo Methods". In: *J. Chem. Phys.* 143.16 (Oct. 2015), p. 164105. ISSN: 0021-9606. DOI: 10.1063/1.4933112.

[52] C. J. Umrigar et al. "Alleviation of the Fermion-Sign Problem by Optimization of Many-Body Wave Functions". In: *Phys. Rev. Lett.* 98.11 (Mar. 2007), p. 110201. DOI: 10.1103/PhysRevLett.98.110201.

[53] Miguel A. Morales et al. "Multideterminant Wave Functions in Quantum Monte Carlo". In: *J. Chem. Theory Comput.* 8.7 (July 2012), pp. 2181–2188. ISSN: 1549-9618. DOI: 10.1021/ct3003404.

[54] David Pfau et al. “Ab Initio Solution of the Many-Electron Schr\"odinger Equation with Deep Neural Networks”. In: *Phys. Rev. Research* 2.3 (Sept. 2020), p. 033429. DOI: 10.1103/PhysRevResearch.2.033429.

[55] Jan Hermann, Zeno Schätzle, and Frank Noé. “Deep-Neural-Network Solution of the Electronic Schrödinger Equation”. In: *Nat. Chem.* 12.10 (Oct. 2020), pp. 891–897. ISSN: 1755-4349. DOI: 10.1038/s41557-020-0544-y.

[56] Max Wilson et al. “Simulations of State-of-the-Art Fermionic Neural Network Wave Functions with Diffusion Monte Carlo”. In: *arXiv:2103.12570* (Mar. 2021). arXiv: 2103.12570.

[57] C. J. Umrigar, M. P. Nightingale, and K. J. Runge. “A Diffusion Monte Carlo Algorithm with Very Small Time-step Errors”. In: *J. Chem. Phys.* 99.4 (Aug. 1993), pp. 2865–2890. ISSN: 0021-9606. DOI: 10.1063/1.465195.

[58] George H. Booth, Alex J.W. Thom, and Ali Alavi. “Fermion Monte Carlo without Fixed Nodes: A Game of Life, Death, and Annihilation in Slater Determinant Space”. In: *J. Chem. Phys.* 131.5 (Aug. 2009), p. 054106. ISSN: 00219606. DOI: 10.1063/1.3193710.

[59] Deidre Cleland, George H. Booth, and Ali Alavi. “Communications: Survival of the Fittest: Accelerating Convergence in Full Configuration-Interaction Quantum Monte Carlo”. In: *J. Chem. Phys.* 132.4 (2010). ISSN: 00219606. DOI: 10.1063/1.3302277.

[60] Nandini Trivedi and D. M. Ceperley. “Ground-State Correlations of Quantum Antiferromagnets: A Green-Function Monte Carlo Study”. In: *Phys. Rev. B* 41.7 (Mar. 1990), pp. 4552–4569. DOI: 10.1103/PhysRevB.41.4552.

[61] J. C. Slater. “The Theory of Complex Spectra”. In: *Phys. Rev.* 34.10 (Nov. 1929), pp. 1293–1322. DOI: 10.1103/PhysRev.34.1293.

[62] E. U. Condon. “The Theory of Complex Spectra”. In: *Phys. Rev.* 36.7 (Oct. 1930), pp. 1121–1133. DOI: 10.1103/PhysRev.36.1121.

[63] J. S. Spencer, N. S. Blunt, and W. M.c. Foulkes. “The Sign Problem and Population Dynamics in the Full Configuration Interaction Quantum Monte Carlo Method”. In: *J. Chem. Phys.* 136.5 (Feb. 2012), p. 054110. ISSN: 0021-9606. DOI: 10.1063/1.3681396.

[64] C Lin, F H Zong, and D M Ceperley. "Twist-Averaged Boundary Conditions in Continuum Quantum Monte Carlo Algorithms." In: *Phys. Rev. E Stat. Nonlin. Soft Matter Phys.* 64.1 (2001), p. 016702. ISSN: 1539-3755. DOI: 10.1103/PhysRevE.64.016702. arXiv: cond-mat/0101339.

[65] Simone Chiesa et al. "Finite-Size Error in Many-Body Simulations with Long-Range Interactions". In: *Phys. Rev. Lett.* 97.7 (2006), p. 076404. ISSN: 0031-9007. DOI: 10.1103/PhysRevLett.97.076404.

[66] R Gaudoin and J M Pitarke. "Quantum Monte Carlo Modeling of the Spherically Averaged Structure Factor of a Many-Electron System". In: *Phys Rev B - Condens Matter Mater Phys* 75.15 (2007), pp. 1–4. ISSN: 10980121. DOI: 10.1103/PhysRevB.75.155105. arXiv: cond-mat/0607406.

[67] N. D. Drummond et al. "Finite-Size Errors in Continuum Quantum Monte Carlo Calculations". In: *Phys. Rev. B - Condens. Matter Mater. Phys.* 78.12 (2008), pp. 1–19. ISSN: 10980121. DOI: 10.1103/PhysRevB.78.125106. arXiv: 0806.0957.

[68] Markus Holzmann et al. "Theory of Finite Size Effects for Electronic Quantum Monte Carlo Calculations of Liquids and Solids". In: (2016), pp. 1–23. arXiv: 1603.03957.

[69] Ke Liao and Andreas Grüneis. "Communication: Finite Size Correction in Periodic Coupled Cluster Theory Calculations of Solids". In: *J. Chem. Phys.* 145.14 (2016), pp. 0–4. ISSN: 00219606. DOI: 10.1063/1.4964307.

[70] Thomas Gruber et al. "Applying the Coupled-Cluster Ansatz to Solids and Surfaces in the Thermodynamic Limit". In: *Phys. Rev. X* 8.2 (May 2018), p. 021043. DOI: 10.1103/PhysRevX.8.021043.

[71] P. B. Allen and V. Heine. "Theory of the Temperature Dependence of Electronic Band Structures". In: *J. Phys. C: Solid State Phys.* 9.12 (June 1976), pp. 2305–2312. ISSN: 0022-3719. DOI: 10.1088/0022-3719/9/12/013.

[72] P. B. Allen and M. Cardona. "Temperature Dependence of the Direct Gap of Si and Ge". In: *Phys. Rev. B* 27.8 (Apr. 1983), pp. 4760–4769. DOI: 10.1103/PhysRevB.27.4760.

[73] S. Poncé et al. "Temperature Dependence of Electronic Eigenenergies in the Adiabatic Harmonic Approximation". In: *Phys. Rev. B* 90.21 (Dec. 2014), p. 214304. DOI: 10.1103/PhysRevB.90.214304.

[74] S. Poncé et al. "Verification of First-Principles Codes: Comparison of Total Energies, Phonon Frequencies, Electron–Phonon Coupling and Zero-Point Motion Correction to the Gap between ABINIT and QE/Yambo". In: *Computational Materials Science* 83 (Feb. 2014), pp. 341–348. ISSN: 0927-0256. DOI: 10.1016/j.commatsci.2013.11.031.

[75] Feliciano Giustino. "Electron-Phonon Interactions from First Principles". In: *Rev. Mod. Phys.* 89.1 (Feb. 2017), p. 015003. DOI: 10.1103/RevModPhys.89.015003.

[76] Tong Shen et al. "Influence of High-Energy Local Orbitals and Electron-Phonon Interactions on the Band Gaps and Optical Absorption Spectra of Hexagonal Boron Nitride". In: *Phys. Rev. B* 102.4 (July 2020), p. 045117. DOI: 10.1103/PhysRevB.102.045117.

[77] Mauro Del Ben, Jürg Hutter, and Joost VandeVondele. "Forces and Stress in Second Order Møller-Plesset Perturbation Theory for Condensed Phase Systems within the Resolution-of-Identity Gaussian and Plane Waves Approach". In: *J Chem Phys* 143.10 (Sept. 2015), p. 102803. ISSN: 1089-7690. DOI: 10.1063/1.4919238.

[78] Florian Weigend and Marco Häser. "RI-MP2: First Derivatives and Global Consistency". In: *Theor Chem Acta* 97.1 (Oct. 1997), pp. 331–340. ISSN: 1432-2234. DOI: 10.1007/s002140050269.

[79] Vladimir V. Rybkin and Joost VandeVondele. "Spin-Unrestricted Second-Order Møller–Plesset (MP2) Forces for the Condensed Phase: From Molecular Radicals to F-Centers in Solids". In: *J. Chem. Theory Comput.* 12.5 (May 2016), pp. 2214–2223. ISSN: 1549-9618. DOI: 10.1021/acs.jctc.6b00015.

[80] G. Kresse and D. Joubert. "From Ultrasoft Pseudopotentials to the Projector Augmented-Wave Method". In: *Phys. Rev. B* 59.3 (Jan. 1999), pp. 1758–1775. DOI: 10.1103/PhysRevB.59.1758.

[81] P. E. Blöchl. "Projector Augmented-Wave Method". In: *Phys. Rev. B* 50.24 (Dec. 1994), pp. 17953–17979. ISSN: 01631829. DOI: 10.1103/PhysRevB.50.17953. arXiv: 1408.4701v2.

[82] G Kresse and J Furthmüller. "Efficient Iterative Schemes for Ab Initio Total-Energy Calculations Using a Plane-Wave Basis Set". In: *Phys Rev B* 54.16 (1996), pp. 11169–11186. ISSN: 0163-1829. DOI: 10.1103/PhysRevB.54.11169.

[83] Edgar Solomonik et al. "A Massively Parallel Tensor Contraction Framework for Coupled-Cluster Computations". In: *Journal of Parallel and Distributed Computing*. Domain-Specific Languages and High-Level Frameworks for High-Performance Computing 74.12 (Dec. 2014), pp. 3176–3190. ISSN: 0743-7315. DOI: 10.1016/j.jpdc.2014.06.002.

[84] Atsushi Togo and Isao Tanaka. "$\texttt{Spglib}$: A Software Library for Crystal Symmetry Search". In: *ArXiv180801590 Cond-Mat* (Aug. 2018). arXiv: 1808.01590 [cond-mat].

[85] Jiří Čížek. "On the Correlation Problem in Atomic and Molecular Systems. Calculation of Wavefunction Components in Ursell-Type Expansion Using Quantum-Field Theoretical Methods". In: *J. Chem. Phys.* 45.11 (Dec. 1966), pp. 4256–4266. ISSN: 0021-9606. DOI: 10.1063/1.1727484.

[86] J. Čižek and J. Paldus. "Correlation Problems in Atomic and Molecular Systems III. Rederivation of the Coupled-Pair Many-Electron Theory Using the Traditional Quantum Chemical Methodst". In: *Int. J. Quantum Chem.* 5.4 (1971), pp. 359–379. ISSN: 1097-461X. DOI: 10.1002/qua.560050402.

[87] Christoph Riplinger et al. "Sparse Maps—A Systematic Infrastructure for Reduced-Scaling Electronic Structure Methods. II. Linear Scaling Domain Based Pair Natural Orbital Coupled Cluster Theory". In: *J. Chem. Phys.* 144.2 (Jan. 2016), p. 024109. ISSN: 0021-9606. DOI: 10.1063/1.4939030.

[88] Gunnar Schmitz and Christof Hättig. "Perturbative Triples Correction for Local Pair Natural Orbital Based Explicitly Correlated CCSD(F12*) Using Laplace Transformation Techniques". In: *J. Chem. Phys.* 145.23 (Dec. 2016), p. 234107. ISSN: 0021-9606. DOI: 10.1063/1.4972001.

[89] Max Schwilk et al. "Scalable Electron Correlation Methods. 3. Efficient and Accurate Parallel Local Coupled Cluster with Pair Natural Orbitals (PNO-LCCSD)". In: *J. Chem. Theory Comput.* 13.8 (Aug. 2017), pp. 3650–3675. ISSN: 1549-9618. DOI: 10.1021/acs.jctc.7b00554.

[90] Péter R. Nagy, Gyula Samu, and Mihály Kállay. "Optimization of the Linear-Scaling Local Natural Orbital CCSD(T) Method: Improved Algorithm and Benchmark Applications". In: *J. Chem. Theory Comput.* 14.8 (Aug. 2018), pp. 4193–4215. ISSN: 1549-9618. DOI: 10.1021/acs.jctc.8b00442.

[91] George H Booth et al. "Towards an Exact Description of Electronic Wavefunctions in Real Solids." In: *Nature* 493.7432 (2013), pp. 365–70. ISSN: 1476-4687. DOI: 10.1038/nature11770.

[92] James McClain et al. "Gaussian-Based Coupled-Cluster Theory for the Ground-State and Band Structure of Solids". In: *J. Chem. Theory Comput.* 13.3 (Mar. 2017), pp. 1209–1218. ISSN: 1549-9618. DOI: 10.1021/acs.jctc.7b00049.

[93] Ke Liao et al. "A Comparative Study Using State-of-the-Art Electronic Structure Theories on Solid Hydrogen Phases under High Pressures". In: *npj Comput. Mater.* 5.1 (Dec. 2019), p. 110. ISSN: 2057-3960. DOI: 10.1038/s41524-019-0243-7.

[94] Yang Gao et al. "Electronic Structure of Bulk Manganese Oxide and Nickel Oxide from Coupled Cluster Theory". In: *Phys. Rev. B* 101.16 (Apr. 2020), p. 165138. DOI: 10.1103/PhysRevB.101.165138.

[95] Wilfried Meyer. "Ionization Energies of Water from PNO-CI Calculations". In: *Int J Quantum Chem* 5.S5 (1971), pp. 341–348. ISSN: 1097-461X. DOI: 10.1002/qua.560050839.

[96] Marcel Nooijen and Robert J. Le Roy. "Orbital Invariant Single-Reference Coupled Electron Pair Approximation with Extensive Renormalized Triples Correction". In: *Journal of Molecular Structure: THEOCHEM*. Coupled-Cluster Methods: Theory and Applications. A Collection of Invited Papers in Honor of Debashis Mukherjee on the Occasion of His 60th Birthday 768.1 (Aug. 2006), pp. 25–43. ISSN: 0166-1280. DOI: 10.1016/j.theochem.2006.05.017.

[97] Frank Neese, Frank Wennmohs, and Andreas Hansen. "Efficient and Accurate Local Approximations to Coupled-Electron Pair Approaches: An Attempt to Revive the Pair Natural Orbital Method". In: *J. Chem. Phys.* 130.11 (Mar. 2009), p. 114108. ISSN: 0021-9606. DOI: 10.1063/1.3086717.

[98] Lee M. J. Huntington and Marcel Nooijen. "pCCSD: Parameterized Coupled-Cluster Theory with Single and Double Excitations". In: *J. Chem. Phys.* 133.18 (Nov. 2010), p. 184109. ISSN: 0021-9606. DOI: 10.1063/1.3494113.

[99] J. Paldus, J. Čížek, and M. Takahashi. "Approximate Account of the Connected Quadruply Excited Clusters in the Coupled-Pair Many-Electron

Theory". In: *Phys. Rev. A* 30.5 (Nov. 1984), pp. 2193–2209. DOI: 10.1103/PhysRevA.30.2193.

[100] Piotr Piecuch and Josef Paldus. "On the Solution of Coupled-Cluster Equations in the Fully Correlated Limit of Cyclic Polyene Model". In: *Int. J. Quantum Chem.* 40.S25 (1991), pp. 9–34. ISSN: 1097-461X. DOI: 10.1002/qua.560400807.

[101] Rodney J. Bartlett and Monika Musiał. "Addition by Subtraction in Coupled-Cluster Theory: A Reconsideration of the CC and CI Interface and the nCC Hierarchy". In: *J. Chem. Phys.* 125.20 (Nov. 2006), p. 204105. ISSN: 0021-9606. DOI: 10.1063/1.2387952.

[102] James B. Robinson and Peter J. Knowles. "Approximate Variational Coupled Cluster Theory". In: *J. Chem. Phys.* 135.4 (July 2011), p. 044113. ISSN: 0021-9606. DOI: 10.1063/1.3615060.

[103] David W. Small, Keith V. Lawler, and Martin Head-Gordon. "Coupled Cluster Valence Bond Method: Efficient Computer Implementation and Application to Multiple Bond Dissociations and Strong Correlations in the Acenes". In: *J. Chem. Theory Comput.* 10.5 (May 2014), pp. 2027–2040. ISSN: 1549-9618. DOI: 10.1021/ct500112y.

[104] Daniel Kats. "Communication: The Distinguishable Cluster Approximation. II. The Role of Orbital Relaxation". In: *J. Chem. Phys.* 141.6 (Aug. 2014), p. 061101. ISSN: 0021-9606, 1089-7690. DOI: 10.1063/1.4892792.

[105] Daniel Kats et al. "Accurate Thermochemistry from Explicitly Correlated Distinguishable Cluster Approximation". In: *J. Chem. Phys.* 142.6 (2015). ISSN: 00219606. DOI: 10.1063/1.4907591.

[106] Varun Rishi et al. "Excited States from Modified Coupled Cluster Methods: Are They Any Better than EOM CCSD?" In: *J. Chem. Phys.* 146.14 (Apr. 2017), p. 144104. ISSN: 0021-9606. DOI: 10.1063/1.4979078.

[107] Theodoros Tsatsoulis et al. "A Comparison between Quantum Chemistry and Quantum Monte Carlo Techniques for the Adsorption of Water on the (001) LiH Surface". In: *J. Chem. Phys.* 146.20 (May 2017), p. 204108. ISSN: 0021-9606. DOI: 10.1063/1.4984048.

[108] Samuel Francis Boys and John Wilfrid Linnett. "Some Bilinear Convergence Characteristics of the Solutions of Dissymmetric Secular Equations". In: *Proc. R. Soc. Math. Phys. Eng. Sci.* 309.1497 (Mar. 1969), pp. 195–208. DOI: 10.1098/rspa.1969.0037.

[109] Osamu Hino, Yoshitaka Tanimura, and Seiichiro Ten-no. "Biorthogonal Approach for Explicitly Correlated Calculations Using the Transcorrelated Hamiltonian". In: *J. Chem. Phys.* 115.17 (Oct. 2001), pp. 7865–7871. ISSN: 0021-9606. DOI: 10.1063/1.1408299.

[110] Osamu Hino, Yoshitaka Tanimura, and Seiichiro Ten-no. "Application of the Transcorrelated Hamiltonian to the Linearized Coupled Cluster Singles and Doubles Model". In: *Chem. Phys. Lett.* 353.3 (Feb. 2002), pp. 317–323. ISSN: 0009-2614. DOI: 10.1016/S0009-2614(02)00042-8.

[111] Naoto Umezawa and Shinji Tsuneyuki. "Ground-State Correlation Energy for the Homogeneous Electron Gas Calculated by the Transcorrelated Method". In: *Phys. Rev. B* 69.16 (Apr. 2004), p. 165102. DOI: 10.1103/PhysRevB.69.165102.

[112] Rei Sakuma and Shinji Tsuneyuki. "Electronic Structure Calculations of Solids with a Similarity-Transformed Hamiltonian". In: *J. Phys. Soc. Jpn.* 75.10 (Oct. 2006), p. 103705. ISSN: 0031-9015. DOI: 10.1143/JPSJ.75.103705.

[113] Masayuki Ochi and Shinji Tsuneyuki. "Second-Order Møller–Plesset Perturbation Theory for the Transcorrelated Hamiltonian Applied to Solid-State Calculations". In: *Chem. Phys. Lett.* 621 (Feb. 2015), pp. 177–183. ISSN: 0009-2614. DOI: 10.1016/j.cplett.2015.01.009.

[114] Masayuki Ochi et al. "Iterative Diagonalization of the Non-Hermitian Transcorrelated Hamiltonian Using a Plane-Wave Basis Set: Application to Sp-Electron Systems with Deep Core States". In: *J. Chem. Phys.* 144.10 (Mar. 2016), p. 104109. ISSN: 0021-9606. DOI: 10.1063/1.4943117.

[115] Masayuki Ochi, Ryotaro Arita, and Shinji Tsuneyuki. "Correlated Band Structure of a Transition Metal Oxide ZnO Obtained from a Many-Body Wave Function Theory". In: *Phys. Rev. Lett.* 118.2 (Jan. 2017), p. 026402. DOI: 10.1103/PhysRevLett.118.026402.

[116] Hongjun Luo and Ali Alavi. "Combining the Transcorrelated Method with Full Configuration Interaction Quantum Monte Carlo: Application to the Homogeneous Electron Gas". In: *J. Chem. Theory Comput.* 14.3 (Mar. 2018), pp. 1403–1411. ISSN: 1549-9618. DOI: 10.1021/acs.jctc.7b01257.

[117] Péter Jeszenszki et al. "Accelerating the Convergence of Exact Diagonalization with the Transcorrelated Method: Quantum Gas in One Dimension with Contact Interactions". In: *Phys. Rev. A* 98.5 (Nov. 2018), p. 053627. DOI: 10.1103/PhysRevA.98.053627.

[118] Werner Dobrautz, Hongjun Luo, and Ali Alavi. "Compact Numerical Solutions to the Two-Dimensional Repulsive Hubbard Model Obtained via Nonunitary Similarity Transformations". In: *Phys. Rev. B* 99.7 (Feb. 2019). ISSN: 2469-9950, 2469-9969. DOI: 10.1103/PhysRevB.99.075119.

[119] Aron J. Cohen et al. "Similarity Transformation of the Electronic Schrödinger Equation via Jastrow Factorization". In: *J. Chem. Phys.* 151.6 (Aug. 2019), p. 061101. ISSN: 0021-9606. DOI: 10.1063/1.5116024.

[120] Péter Jeszenszki et al. "Eliminating the Wave-Function Singularity for Ultracold Atoms by a Similarity Transformation". In: *Phys. Rev. Research* 2.4 (Nov. 2020), p. 043270. DOI: 10.1103/PhysRevResearch.2.043270.

[121] Xin-Zheng Li et al. "Classical and Quantum Ordering of Protons in Cold Solid Hydrogen under Megabar Pressures." In: *J. Phys. Condens. Matter* 25.8 (2013), p. 085402. ISSN: 1361-648X. DOI: 10.1088/0953-8984/25/8/085402. arXiv: 1302.0062v1.

[122] N. D. Drummond et al. "Quantum Monte Carlo Study of the Phase Diagram of Solid Molecular Hydrogen at Extreme Pressures". In: *Nat. Commun.* 6 (2015), p. 7794. ISSN: 2041-1723. DOI: 10.1038/ncomms8794.

[123] Sam Azadi, W. M. C. Foulkes, and Thomas D. Kühne. "Quantum Monte Carlo Study of High Pressure Solid Molecular Hydrogen". In: *New J. Phys.* 15.11 (2013), p. 113005. ISSN: 1367-2630. DOI: 10.1088/1367-2630/15/11/113005. arXiv: 1307.1463.

[124] Jeremy McMinis et al. "Molecular to Atomic Phase Transition in Hydrogen under High Pressure". In: *Phys. Rev. Lett.* 114.10 (2015). ISSN: 10797114. DOI: 10.1103/PhysRevLett.114.105305.

[125] Miguel A. Morales et al. "Nuclear Quantum Effects and Nonlocal Exchange-Correlation Functionals Applied to Liquid Hydrogen at High Pressure". In: *Phys. Rev. Lett.* 110.6 (Feb. 2013), p. 065702. DOI: 10.1103/PhysRevLett.110.065702.

[126] Miguel A. Morales et al. "Towards a Predictive First-Principles Description of Solid Molecular Hydrogen with Density Functional Theory". In: *Phys. Rev. B* 87.18 (May 2013), p. 184107. DOI: 10.1103/PhysRevB.87.184107.

[127] Russel J. Hemley and Ho-kwang Mao. *Phase Transition in Solid Molecular Hydrogen at Ultrahigh Pressures*. Tech. rep. 1988.

[128] Hector E. Lorenzana, Isaac F. Silvera, and Kenneth A. Goettel. "Evidence for a Structural Phase Transition in Solid Hydrogen at Megabar Pressures". In: *Phys. Rev. Lett.* 63.19 (Nov. 1989), pp. 2080–2083. DOI: 10.1103/PhysRevLett.63.2080.

[129] Ho Kwang Mao and Russell J Hemley. "Ultrahigh-Pressure Transitions in Solid Hydrogen". In: *Rev. Mod. Phys.* 66.2 (1994), pp. 671–692. ISSN: 00346861. DOI: 10.1103/RevModPhys.66.671.

[130] Vincent Natoli, Richard M. Martin, and David Ceperley. "Crystal Structure of Molecular Hydrogen at High Pressure". In: *Phys. Rev. Lett.* 74.9 (Feb. 1995), pp. 1601–1604. DOI: 10.1103/PhysRevLett.74.1601.

[131] Igor Goncharenko and Paul Loubeyre. "Neutron and X-Ray Diffraction Study of the Broken Symmetry Phase Transition in Solid Deuterium". In: *Nature* 435.7046 (June 2005), p. 1206. ISSN: 1476-4687. DOI: 10.1038/nature03699.

[132] Chris J. Pickard and Richard J. Needs. "Structure of Phase III of Solid Hydrogen". In: *Nat. Phys.* 3.7 (July 2007), pp. 473–476. ISSN: 1745-2473. DOI: 10.1038/nphys625. arXiv: 1609.07486.

[133] Ross T. Howie et al. "Mixed Molecular and Atomic Phase of Dense Hydrogen". In: *Phys. Rev. Lett.* 108.12 (Mar. 2012), p. 125501. DOI: 10.1103/PhysRevLett.108.125501.

[134] Eugene Wigner and Hillard B. Huntington. "On the Possibility of a Metallic Modification of Hydrogen". In: *J. Chem. Phys.* 3.12 (Dec. 1935), pp. 764–770. ISSN: 00219606. DOI: 10.1063/1.1749590.

[135] Russel J. Hemley and Ho-kwang Mao. "Optical Studies of Hydrogen Above 200 Gigapascals: Evidence for Metallization by Band Overlap". In: *Science* 244.4911 (June 1989), pp. 1462–1465. ISSN: 0036-8075, 1095-9203. DOI: 10.1126/science.244.4911.1462.

[136] S. T. Weir, A. C. Mitchell, and W. J. Nellis. "Metallization of Fluid Molecular Hydrogen at 140 GPa (1.4 Mbar)". In: *Phys. Rev. Lett.* 76.11 (Mar. 1996), pp. 1860–1863. ISSN: 0031-9007. DOI: 10.1103/PhysRevLett.76.1860.

[137] Kurt A. Johnson and N. W. Ashcroft. "Structure and Bandgap Closure in Dense Hydrogen". In: *Nature* 403.6770 (2000), pp. 632–635. ISSN: 00280836. DOI: 10.1038/35001024.

[138] M. I. Eremets and I. A. Troyan. "Conductive Dense Hydrogen". In: *Nat. Mater.* 10.12 (Dec. 2011), pp. 927–931. ISSN: 14764660. DOI: 10.1038/nmat3175.

[139] Ji Chen et al. "Quantum Simulation of Low-Temperature Metallic Liquid Hydrogen". In: *Nat. Commun.* 4 (June 2013), p. 2064. ISSN: 2041-1723. DOI: 10.1038/ncomms3064.

[140] M. D. Knudson et al. "Direct Observation of an Abrupt Insulator-to-Metal Transition in Dense Liquid Deuterium". In: *Science* 348.6242 (June 2015), pp. 1455–1460. ISSN: 0036-8075, 1095-9203. DOI: 10.1126/science.aaa7471.

[141] Mohamed Zaghoo, Ashkan Salamat, and Isaac F. Silvera. "Evidence of a First-Order Phase Transition to Metallic Hydrogen". In: *Phys. Rev. B* 93.15 (Apr. 2016), p. 155128. DOI: 10.1103/PhysRevB.93.155128.

[142] Ranga P Dias and Isaac F Silvera. "Observation of the Wigner-Huntington Transition to Metallic Hydrogen". In: *Science* 355.6326 (Jan. 2017), pp. 715–718. ISSN: 10959203. DOI: 10.1126/science.aal1579. arXiv: 1703.03064.

[143] N. W. Ashcroft. "Metallic Hydrogen: A High-Temperature Superconductor?" In: *Phys. Rev. Lett.* 21.26 (1968), pp. 1748–1749. ISSN: 00319007. DOI: 10.1103/PhysRevLett.21.1748.

[144] Egor Babaev, Asle Sudbø, and N. W. Ashcroft. "A Superconductor to Superfluid Phase Transition in Liquid Metallic Hydrogen". In: *Nature* 431.7009 (Oct. 2004), p. 666. ISSN: 1476-4687. DOI: 10.1038/nature02910.

[145] Ranga P Dias and Isaac F Silvera. "Erratum for the Research Article Observation of the Wigner-Huntington Transition to Metallic Hydrogen by R. P. Dias and I. F. Silvera (Science (2017) 355 (715) DOI: 10.1126/Science.Aal1579)". In: *Science* 357.6352 (Aug. 2017), eaao5843. ISSN: 10959203. DOI: 10.1126/science.aao5843.

[146] Hua Y. Geng. "Public Debate on Metallic Hydrogen to Boost High Pressure Research". In: *Matter and Radiation at Extremes* 2.6 (Nov. 2017), pp. 275–277. ISSN: 2468-2047. DOI: 10.1016/j.mre.2017.10.001.

[147] Chandrabhas Narayana et al. "Solid Hydrogen at 342 GPa: No Evidence for an Alkali Metal". In: *Nature* 393.6680 (May 1998), pp. 46–49. ISSN: 00280836. DOI: 10.1038/29949. arXiv: physics/9810036.

[148] Paul Loubeyre, Florent Occelli, and René LeToullec. "Optical Studies of Solid Hydrogen to 320 GPa and Evidence for Black Hydrogen". In: *Nature* 416.6881 (Apr. 2002), pp. 613–617. ISSN: 00280836. DOI: 10.1038/416613a.

[149] Hélio Chacham and Steven G. Louie. "Metallization of Solid Hydrogen at Megabar Pressures: A First-Principles Quasiparticle Study". In: *Phys. Rev. Lett.* 66.1 (Jan. 1991), pp. 64–67. ISSN: 00319007. DOI: 10.1103/PhysRevLett.66.64.

[150] John S. Tse and Dennis D. Klug. "Evidence from Molecular Dynamics Simulations for Non-Metallic Behaviour of Solid Hydrogen above 160 GPa". In: *Nature* 378.6557 (Dec. 1995), pp. 595–597. ISSN: 00280836. DOI: 10.1038/378595a0.

[151] Sam Azadi et al. "Dissociation of High-Pressure Solid Molecular Hydrogen: A Quantum Monte Carlo and Anharmonic Vibrational Study". In: *Phys. Rev. Lett.* 112.16 (2014). ISSN: 10797114. DOI: 10.1103/PhysRevLett.112.165501. arXiv: 1403.3681.

[152] Sam Azadi, N. D. Drummond, and W. M. C. Foulkes. "Nature of the Metallization Transition in Solid Hydrogen". In: *Phys. Rev. B* 95.3 (2017), p. 35142. ISSN: 24699969. DOI: 10.1103/PhysRevB.95.035142. arXiv: 1608.00754.

[153] Jorge Kohanoff et al. "Solid Molecular Hydrogen: The Broken Symmetry Phase". In: *Phys. Rev. Lett.* 78.14 (Apr. 1997), pp. 2783–2786. DOI: 10.1103/PhysRevLett.78.2783.

[154] D M Ceperley and B J Alder. *Ground State of Solid Hydrogen*. 1987.

[155] Raymond C Clay et al. "Benchmarking Exchange-Correlation Functionals for Hydrogen at High Pressures Using Quantum Monte Carlo". In: *Phys. Rev. B - Condens. Matter Mater. Phys.* 89.18 (2014), p. 184106. ISSN: 1550235X. DOI: 10.1103/PhysRevB.89.184106. arXiv: 1401.7365.

[156] Michael Hanfland, Russell J. Hemley, and Ho-kwang Mao. "Novel Infrared Vibron Absorption in Solid Hydrogen at Megabar Pressures". In: *Phys. Rev. Lett.* 70.24 (June 1993), pp. 3760–3763. DOI: 10.1103/PhysRevLett.70.3760.

[157] Chang-Sheng Zha, Zhenxian Liu, and Russell J. Hemley. "Synchrotron Infrared Measurements of Dense Hydrogen to 360 GPa". In: *Phys. Rev. Lett.* 108.14 (Apr. 2012), p. 146402. DOI: 10.1103/PhysRevLett.108.146402.

[158] Bartomeu Monserrat et al. "Hexagonal Structure of Phase III of Solid Hydrogen". In: *Phys. Rev. B* 94.13 (Oct. 2016), p. 134101. DOI: 10.1103/PhysRevB.94.134101.

[159] Xiao-Wei Zhang, En-Ge Wang, and Xin-Zheng Li. "Ab Initio Investigation on the Experimental Observation of Metallic Hydrogen". In: *Phys. Rev. B* 98.13 (Oct. 2018), p. 134110. DOI: 10.1103/PhysRevB.98.134110.

[160] Sam Azadi and Graeme J. Ackland. "The Role of van Der Waals and Exchange Interactions in High-Pressure Solid Hydrogen". In: *Phys. Chem. Chem. Phys.* 19.32 (Aug. 2017), pp. 21829–21839. ISSN: 1463-9084. DOI: 10.1039/C7CP03729E.

[161] Theodoros Tsatsoulis et al. "Reaction Energetics of Hydrogen on Si(100) Surface: A Periodic Many-Electron Theory Study". In: *J. Chem. Phys.* 149.24 (Dec. 2018), p. 244105. ISSN: 0021-9606. DOI: 10.1063/1.5055706.

[162] Jan Gerit Brandenburg et al. "Physisorption of Water on Graphene: Subchemical Accuracy from Many-Body Electronic Structure Methods". In: *J. Phys. Chem. Lett.* 10.3 (Feb. 2019), pp. 358–368. ISSN: 1948-7185. DOI: 10.1021/acs.jpclett.8b03679.

[163] Thomas Gruber and Andreas Grüneis. "*Ab Initio* Calculations of Carbon and Boron Nitride Allotropes and Their Structural Phase Transitions Using Periodic Coupled Cluster Theory". In: *Phys. Rev. B* 98.13 (Oct. 2018). ISSN: 2469-9950, 2469-9969. DOI: 10.1103/PhysRevB.98.134108.

[164] Simons Collaboration on the Many-Electron Problem et al. "Towards the Solution of the Many-Electron Problem in Real Materials: Equation of State of the Hydrogen Chain with State-of-the-Art Many-Body Methods". In: *Phys. Rev. X* 7.3 (Sept. 2017), p. 031059. DOI: 10.1103/PhysRevX.7.031059.

[165] John P. Perdew, Kieron Burke, and Matthias Ernzerhof. "Generalized Gradient Approximation Made Simple". In: *Phys. Rev. Lett.* 77.18 (Oct. 1996), pp. 3865–3868. DOI: 10.1103/PhysRevLett.77.3865.

[166] Biswajit Santra et al. "Hydrogen Bonds and van Der Waals Forces in Ice at Ambient and High Pressures". In: *Phys. Rev. Lett.* 107.18 (Oct. 2011), p. 185701. DOI: 10.1103/PhysRevLett.107.185701.

[167] James J. Shepherd et al. "Full Configuration Interaction Perspective on the Homogeneous Electron Gas". In: *Phys. Rev. B - Condens. Matter Mater. Phys.* 85.8 (2012), pp. 1–4. ISSN: 10980121. DOI: 10.1103/PhysRevB.85.081103. arXiv: 1109.2635.

[168] Michele Ruggeri, Pablo López Ríos, and Ali Alavi. "Correlation Energies of the High-Density Spin-Polarized Electron Gas to meV Accuracy". In: *Phys. Rev. B* 98.16 (Oct. 2018), p. 161105. DOI: 10.1103/PhysRevB.98.161105.

[169] Andreas Irmler and Andreas Grüneis. "Particle-Particle Ladder Based Basis-Set Corrections Applied to Atoms and Molecules Using Coupled-Cluster Theory". In: *J. Chem. Phys.* 151.10 (Sept. 2019), p. 104107. ISSN: 0021-9606. DOI: 10.1063/1.5110885.

[170] Peter E. Blöchl, Clemens J. Först, and Johannes Schimpl. "Projector Augmented Wave Method: Ab Initio Molecular Dynamics with Full Wave Functions". In: *Bull. Mater. Sci.* 26.1 (2003), pp. 33–41. ISSN: 02504707. DOI: 10.1007/BF02712785. arXiv: cond-mat/0201015.

[171] G Kresse and J Hafner. "Norm-Conserving and Ultrasoft Pseudopotentials for First-Row and Transition Elements". In: *J. Phys. Condens. Matter* 6.40 (1994), pp. 8245–8257. ISSN: 0953-8984. DOI: 10.1088/0953-8984/6/40/015.

[172] Andreas Grüneis et al. "Perspective: Explicitly Correlated Electronic Structure Theory for Complex Systems". In: *J. Chem. Phys.* 146.8 (Feb. 2017), p. 080901. ISSN: 0021-9606. DOI: 10.1063/1.4976974.

[173] K. Ghanem, A. Y. Lozovoi, and A. Alavi. "Unbiasing the Initiator Approximation in I-FCIQMC". In: *To be published.* (2019).

[174] Paul Loubeyre, Florent Occelli, and Paul Dumas. "Synchrotron Infrared Spectroscopic Evidence of the Probable Transition to Metal Hydrogen". In: *Nature* 577.7792 (Jan. 2020), pp. 631–635. ISSN: 0028-0836, 1476-4687. DOI: 10.1038/s41586-019-1927-3.

[175] Isaac F. Silvera and Ranga Dias. "Comment on: Observation of a First Order Phase Transition to Metal Hydrogen near 425 GPa". In: *ArXiv190703198 Cond-Mat* (July 2019). arXiv: 1907.03198 [cond-mat].

[176] Vitaly Gorelov et al. "Energy Gap Closure of Crystalline Molecular Hydrogen with Pressure". In: *Phys. Rev. Lett.* 124.11 (Mar. 2020), p. 116401. DOI: 10.1103/PhysRevLett.124.116401.

[177] Kyuho Lee et al. "Higher-Accuracy van Der Waals Density Functional". In: *Phys. Rev. B* 82.8 (Aug. 2010), p. 081101. DOI: 10.1103/PhysRevB.82.081101.

[178] Andreas Grüneis, Martijn Marsman, and Georg Kresse. "Second-Order Møller–Plesset Perturbation Theory Applied to Extended Systems. II. Structural and Energetic Properties". In: *J Chem Phys* 133.7 (2010), p. 74107. ISSN: 00219606. DOI: 10.1063/1.3466765.

[179] D. Sangalli et al. "Many-Body Perturbation Theory Calculations Using the Yambo Code". In: *J. Phys.: Condens. Matter* 31.32 (May 2019), p. 325902. ISSN: 0953-8984. DOI: 10.1088/1361-648X/ab15d0.

[180] Lorenzo Monacelli et al. "Black Metal Hydrogen above 360 GPa Driven by Proton Quantum Fluctuations". In: *Nat. Phys.* (Sept. 2020), pp. 1–5. ISSN: 1745-2481. DOI: 10.1038/s41567-020-1009-3.

[181] Mehmet Dogan, Sehoon Oh, and Marvin L. Cohen. "Observed Metallization of Hydrogen Interpreted as a Band Structure Effect". In: *J. Phys.: Condens. Matter* 33.3 (Oct. 2020), 03LT01. ISSN: 0953-8984. DOI: 10.1088/1361-648X/abba8a.

[182] Isaac F. Silvera and Ranga Dias. "Metallic Hydrogen". In: *J. Phys.: Condens. Matter* 30.25 (May 2018), p. 254003. ISSN: 0953-8984. DOI: 10.1088/1361-648X/aac401.

[183] Paul Loubeyre, Florent Occelli, and Paul Dumas. "Comment on: Observation of the Wigner-Huntington Transition to Metallic Hydrogen". In: *ArXiv170207192 Cond-Mat* (Feb. 2017). arXiv: 1702.07192 [cond-mat].

[184] Felix Hummel, Theodoros Tsatsoulis, and Andreas Grüneis. "Low Rank Factorization of the Coulomb Integrals for Periodic Coupled Cluster Theory". In: *J. Chem. Phys.* 146.12 (Mar. 2017), p. 124105. ISSN: 0021-9606. DOI: 10.1063/1.4977994.

[185] P. B. Allen and V. Heine. "Theory of the Temperature Dependence of Electronic Band Structures". In: *J. Phys. C: Solid State Phys.* 9.12 (June 1976), pp. 2305–2312. ISSN: 0022-3719. DOI: 10.1088/0022-3719/9/12/013.

[186] Paolo Giannozzi et al. "QUANTUM ESPRESSO: A Modular and Open-Source Software Project for Quantum Simulations of Materials". In: *J. Phys.: Condens. Matter* 21.39 (Sept. 2009), p. 395502. ISSN: 0953-8984. DOI: 10.1088/0953-8984/21/39/395502.

[187] Andrea Marini et al. "Yambo: An Ab Initio Tool for Excited State Calculations". In: *Computer Physics Communications* 180.8 (Aug. 2009), pp. 1392–1403. ISSN: 0010-4655. DOI: 10.1016/j.cpc.2009.02.003.

[188] D. R. Hamann. "Optimized Norm-Conserving Vanderbilt Pseudopotentials". In: *Phys. Rev. B* 88.8 (Aug. 2013), p. 085117. DOI: 10.1103/PhysRevB.88.085117.

[189] E. Wigner. "On the Interaction of Electrons in Metals". In: *Phys. Rev.* 46.11 (Dec. 1934), pp. 1002–1011. DOI: 10.1103/PhysRev.46.1002.

[190] D. M. Ceperley and B. J. Alder. "Ground State of the Electron Gas by a Stochastic Method". In: *Phys. Rev. Lett.* 45.7 (Aug. 1980), pp. 566–569. DOI: 10.1103/PhysRevLett.45.566.

[191] W. Kohn and L. J. Sham. "Self-Consistent Equations Including Exchange and Correlation Effects". In: *Phys. Rev.* 140.4A (Nov. 1965), A1133–A1138. DOI: 10.1103/PhysRev.140.A1133.

[192] J. P. Perdew and Alex Zunger. "Self-Interaction Correction to Density-Functional Approximations for Many-Electron Systems". In: *Phys. Rev. B* 23.10 (May 1981), pp. 5048–5079. DOI: 10.1103/PhysRevB.23.5048.

[193] James J. Shepherd, George H. Booth, and Ali Alavi. "Investigation of the Full Configuration Interaction Quantum Monte Carlo Method Using Homogeneous Electron Gas Models". In: *J. Chem. Phys.* 136.24 (June 2012), p. 244101. ISSN: 0021-9606. DOI: 10.1063/1.4720076.

[194] James J. Shepherd, Thomas M. Henderson, and Gustavo E. Scuseria. "Range-Separated Brueckner Coupled Cluster Doubles Theory". In: *Phys. Rev. Lett.* 112.13 (Apr. 2014), p. 133002. DOI: 10.1103/PhysRevLett.112.133002.

[195] James J. Shepherd, Thomas M. Henderson, and Gustavo E. Scuseria. "Coupled Cluster Channels in the Homogeneous Electron Gas". In: *J. Chem. Phys.* 140.12 (Mar. 2014), p. 124102. ISSN: 0021-9606. DOI: 10.1063/1.4867783.

[196] Verena A. Neufeld and Alex J. W. Thom. "A Study of the Dense Uniform Electron Gas with High Orders of Coupled Cluster". In: *J. Chem. Phys.* 147.19 (Nov. 2017), p. 194105. ISSN: 0021-9606. DOI: 10.1063/1.5003794.

[197] Andreas Irmler et al. "Duality of Ring and Ladder Diagrams and Its Importance for Many-Electron Perturbation Theories". In: *Phys. Rev. Lett.* 123.15 (Oct. 2019), p. 156401. ISSN: 0031-9007, 1079-7114. DOI: 10.1103/PhysRevLett.123.156401.

[198] Paola Gori-Giorgi, Francesco Sacchetti, and Giovanni B. Bachelet. "Analytic Structure Factors and Pair-Correlation Functions for the Unpolarized Homogeneous Electron Gas". In: *Phys. Rev. B* 61.11 (Mar. 2000), pp. 7353–7363. ISSN: 0163-1829, 1095-3795. DOI: 10.1103/PhysRevB.61.7353. arXiv: cond-mat/9909448.

[199] T. Gaskell. "The Collective Treatment of a Fermi Gas: II". In: *Proc. Phys. Soc.* 77.6 (June 1961), pp. 1182–1192. ISSN: 0370-1328. DOI: 10.1088/0370-1328/77/6/312.

[200] Kai Guther et al. "NECI: N-Electron Configuration Interaction with an Emphasis on State-of-the-Art Stochastic Methods". In: *J. Chem. Phys.* 153.3 (July 2020), p. 034107. ISSN: 0021-9606. DOI: 10.1063/5.0005754.

[201] Charles R. Harris et al. "Array Programming with NumPy". In: *Nature* 585.7825 (Sept. 2020), pp. 357–362. ISSN: 1476-4687. DOI: 10.1038/s41586-020-2649-2.

[202] P. López Ríos et al. "Inhomogeneous Backflow Transformations in Quantum Monte Carlo Calculations". In: *Phys. Rev. E* 74.6 (Dec. 2006). ISSN: 1539-3755, 1550-2376. DOI: 10.1103/PhysRevE.74.066701.

Appendix A

Curriculum Vitae

Ke Liao

Email: ke.liao.whu@gmail.com

Google Scholar: Ke Liao

Education

- **Exchange Study** from 2014-2015, King's College London, London, UK
- **Bachelor Degree in Physics** in 2015, Wuhan University, Wuhan, China
- **Master Degree in Physics** in 2017, International Max Planck Research School for Condensed Matter Science, Stuttgart, Germany
- **Ph.D. in Chemsitry** in 2021, International Max Planck Research School for Condensed Matter Science, Stuttgart, Germany

Conferences and Presentations

- DPG Spring Meeting, Dresden, Germany (poster), 03.2017
- CECAM workshop: Theoretical Chemistry for Extended Systems, Toulouse, France (co-presenter of poster), 05.2017
- European Summerschool in Quantum Chemistry, Sicily, Italy (poster), 09.2017
- 16th International Congress on Quantum Chemistry, Menton, France (poster), 06.2018
- Workshop: Local correlation approaches for molecules and solids, Regensburg, Germany (poster), 06.2019

- Invited talk by Dr. Ji Chen, Peking University, Beijing, China, 10.2019
- Workshop: 2020 Total Energy and Force Methods, San Sebastian, Spain (poster), 01.2020
- Invited talk at AI Lab, ByteDance (remote video presentation), 12.2020

Publications

- **Ke Liao** and Andreas Grüneis, Communication: Finite size correction in periodic coupled cluster theory calculations of solids, *Journal of Chemical Physics*, 141102 (2016)
- Thomas Gruber, **Ke Liao**, Theodoros Tsatsoulis, Felix Hummel and Andreas Grüneis, Applying the coupled-cluster Ansatz to solids and surfaces in the thermodynamic limit, *Physical Review X*, 8, 021043 (2018)
- **Ke Liao**, Xin-Zheng Li, Ali Alavi, Andreas Grüneis, A comparative study using state-of-the-art electronic structure theories on solid hydrogen phases under high pressures, *npj Computational Materials*, 5, 110 (2019)
- **Ke Liao**, Tong Shen, Xin-Zheng Li, Ali Alavi, Andreas Grüneis, Structural and electronic properties of solid molecular hydrogen from many-electron theories, *Physical Review B* 103 (5), 054111 (2021)
- **Ke Liao**, Thomas Schraivogel, Hongjun Luo, Daniel Kats, Ali Alavi, Towards efficient and accurate ab initio solutions to periodic systems via transcorrelation and coupled cluster theory, *Physical Review Research* 3, 033072 (2021)

Skills

- Programming languages: Python, C++, Fortran
- Natural languages: Chinese, native; English, fluent; German, B1 level